

AD-A268 143



TION PAGE

Form Approved
OMB No. 0704-0188

Pub
gac
col
Da.

stage 1 hour per response, including the time for reviewing instructions, searching existing data sources, gathering and maintaining the data needed to complete the collection of information, Send comments regarding this burden estimate or any other aspect of this collection of information, including suggestions for reducing this burden, to Washington Headquarters Services, Directorate for Information Operations and Reports, 1215 Jefferson Management and Budget, Paperwork Reduction Project (0704-0188), Washington, DC 20503

1. AGENCY USE ONLY (Leave blank)	2. REPORT DATE July 27, 1993	3. REPORT TYPE AND DATES COVERED Final Report covering 09/08/89-05/31/93
----------------------------------	---------------------------------	---

4. TITLE AND SUBTITLE IMPACT ON MOVING STRUCTURES AND EFFECTS OF STRIKER YAW AND TUMBLING	5. FUNDING NUMBERS AFOSR F49620-89-C-0127
--	--

6. AUTHOR(S) Werner Goldsmith	AFOSR-TR- 89 0570
----------------------------------	-------------------

7. PERFORMING ORGANIZATION NAME(S) AND ADDRESS(ES) Department of Mechanical Engineering University of California, Berkeley, CA 94720	8. PERFORMING ORGANIZATION REPORT NUMBER FR-89-C-0127-AF
--	---

9. SPONSORING/MONITORING AGENCY NAME(S) AND ADDRESS(ES) Air Force Office of Scientific Research Directorate for Aerospace Sciences Bolling AFB, DC 20332-6448 (Monitor: Dr. Specer Wu)	10. SPONSORING/MONITORING AGENCY REPORT NUMBER SELECTED AUG 16 1993 S B D
---	--

11. SUPPLEMENTARY NOTES	DISTRIBUTION STATEMENT A Approved for public release Distribution Unlimited
-------------------------	--

12a. DISTRIBUTION/AVAILABILITY STATEMENT Unlimited	DISTRIBUTION CODE 93-18804
---	--

13. ABSTRACT (Maximum 200 words)
Three separate non-standard conditions of projectile impact and perforation were investigated experimentally and analytically. The first concerned impingement of blunt 0.25 in. dia. hard-steel cylinders on stationary thin plates of aluminum and steel at yaw angles up to 19° at velocities from 115-285 m/s. Damage was produced by bulging, lateral indentation and front and side petaling. Measurements of the ballistic limit and terminal velocity were compared with predictions of a model utilizing simplifying phenomenological assumptions. Predictions underestimated the ballistic limit by up to 14% with better correlation at higher yaw angles; they were found to be in good accord with observed final speeds. The second topic involved the effect of striker tumbling on the impact response of thin and moderately thick stationary targets of aluminum, steel and polycarbonate. The 1/2 in dia. blunt projectiles impinged the plates at longitudinal speeds from 250-700 m/s and rotational speeds up to 3600 rad/s. Perforation and post-perforation measurements, including final velocities, oblique angles and crater sizes compared well with predictions of both an analytical and a numerical model. The third subject concerns impact at speeds up to 900 m/s of blunt and conically-tipped strikers on rotat-

14. SUBJECT TERMS projectile impact, plate perforation, yawing impact, tumbling projectile impact, impact on moving targets, perforation damage, ballistic limits, post-perforation velocities	15. NUMBER OF PAGES 100 + 37 p. appendix	16. PRICE CODE
---	---	----------------

17. SECURITY CLASSIFICATION OF REPORT Unclassified	18. SECURITY CLASSIFICATION OF THIS PAGE Unclassified	19. SECURITY CLASSIFICATION OF ABSTRACT Unclassified	20. LIMITATION OF ABSTRACT UL
---	--	---	----------------------------------

13 cont'd
ing targets with tangential velocities up to 133 m/s. Experimental data were also compared with a phenomenological and a numerical model and found to be in excellent agreement. Both of these latter studies constitute substantial extensions of earlier investigations involving these types of impacts.

IMPACT ON MOVING STRUCTURES AND EFFECTS OF STRIKER YAW AND TUMBLING

Final Report on Contract AFOSR F49620-89-C-0127
for the Period 09/08/89 to 05/31/93
with the Air Force Office of Scientific Research
Bolling Air Force Base, Washington, D. C.

Technical Monitor: Dr. Spencer Wu

by

Werner Goldsmith, Principal Investigator

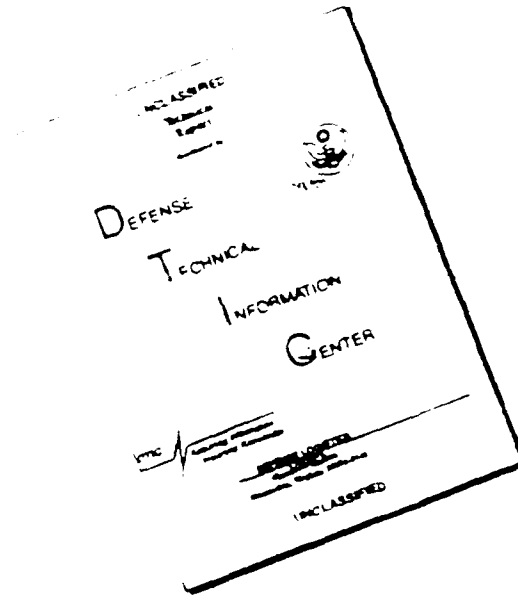
Professor Emeritus (recalled)
Department of Mechanical Engineering

UNIVERSITY OF CALIFORNIA
Berkeley, CA 94720

July 30, 1993

AFOSR-TR-93-057

DISCLAIMER NOTICE



THIS DOCUMENT IS BEST QUALITY AVAILABLE. THE COPY FURNISHED TO DTIC CONTAINED A SIGNIFICANT NUMBER OF PAGES WHICH DO NOT REPRODUCE LEGIBLY.

IMPACT ON MOVING STRUCTURES AND EFFECTS OF STRIKER YAW AND TUMBLING

Final Report on Contract AFOSR F49620-89-C-0127
for the Period 09/08/89 to 05/31/93
with the Air Force Office of Scientific Research
Bolling Air Force Base, Washington, D. C.

Technical Monitor: Dr. Spencer Wu

by

Werner Goldsmith, Principal Investigator

Professor Emeritus (recalled)
Department of Mechanical Engineering

UNIVERSITY OF CALIFORNIA
Berkeley, CA 94720

July 30, 1993

A) YAWING IMPACT ON THIN PLATES BY BLUNT PROJECTILES

The following text constitutes the abstract of the archive journal paper derived from this investigation; the full text may be found in the Appendix. This work was presented as part of the Miklowitz Memorial Symposium at the Joint Meeting of the Applied Mechanics Division of ASME, the Engineering Mechanics Division of ASCE, and the SES at the University of Virginia, Charlottesville, VA, on June 7, 1993. The M.S. thesis by Mr. Eric Tam was submitted on 4/4/91 to the Graduate Division of the University of California, Berkeley, and was entitled "Yaw Impact on Plates by Blunt-nosed Projectiles." A report by Mr. David Tomer, written in the Fall of 1986, entitled Yaw Impact was partly incorporated in the paper.

ABSTRACT

Two series of experimental investigations and an analytical study correlated with one of these were conducted to examine the phenomena attendant to the normal impact of blunt-nosed, hard-steel strikers at moderate angles of yaw (ranging from normal up to 19°) against stationary thin plates of aluminum and steel. The projectiles for the two sequences were 6.35 mm and 6.2 mm in diameter with corresponding lengths of 20 and 19 mm, respectively. The first set of runs involved 2024-0 aluminum and 4130 steel targets with a thickness of 3.175 mm, while the second utilized this thickness for the 2024-0 aluminum, but a thickness of 1.588 mm for the corresponding steel plate. The samples were circular with a 140 mm diameter and were clamped in a holder attached to a massive base. Initial velocities ranged from 115 to 285 m/s.

The experiments were designed to ascertain the ballistic limit at the various angles of yaw. The ballistic limit is the initial velocity of a particular striker required to just perforate a specified target, usually at normal incidence, in 50 percent of a large number of identical tests. At

higher initial speeds, where the projectile was ejected with a final velocity, this value and the final oblique angle were also determined. Post-mortem examination of the plates indicated that damage and failure occurred by bulging, lateral indentation, and side and front petaling.

A theoretical model was developed that analyzed the impact by dividing the process into five stages, utilizing simplifying phenomenological assumptions. These phases consisted of (1) initial striker penetration; (2) normal impact and plate failure; (3) initial rotation of the projectile; (4) shearing and ejection of a plug; and (5) target petaling. A major assumption was the use of a membrane representation for stage (2). Consecutive phases prevailed except for the simultaneity of domains (2) and (3). Two of these steps were identical to those employed in a model of impact on moving targets.

The present analytical model underpredicted the ballistic limit by up to 14.4%, but better correlation was found at higher yaw angles. Excellent agreement was observed between the experimental and analytical final velocities when the data points were corrected to reflect the difference between the experimental values of the ballistic limit and that predicted by the model. Fair agreement was found between the experimental and analytical values of the oblique angle in spite of the paucity of the data obtained, due to the limitations imposed by the equipment.

B) EFFECT OF TUMBLING PROJECTILE IMPACT ON THIN AND MODERATELY THICK TARGETS

a) Objective and Methodology

This portion of the Final Report is concerned with the experimental, analytical and numerical investigation of the effect of tumbling of cylindrical blunt-nosed strikers on thin and moderately thick stationary metallic plates. Deformation patterns, failure phenomena and crater sizes of the targets as well as the final velocities and trajectories of the projectiles and plugs are correlated with initial kinematic information and target thickness. Penetration capability of the striker and the energy absorption capability of the targets are examined in detail.

Various types of impact conditions are sketched in Fig. B-1; it may be noted that the tumbling impact incorporates both yaw and oblique impact as well as an angular motion about an axis through the center of mass orthogonal to the longitudinal axis of the projectile. In the experiments, this type of motion was induced by a generator placed between the gun and the target plate, consisting of a rectangular block whose upper frontal edge was struck by a portion of the frontal face of the initially purely translating striker. This approach was a modification of the technique developed by Ruiz and Goldsmith (1988a, 1988b); there, however, the emphasis was on reproducible tumbling generation and its corresponding phenomenological model rather than the effect of such tumbling on target response.

Blunt-faced hard-steel cylinders (R_C 54) with a diameter of 12.7 mm and a length of 38.2 mm were fired from either pneumatic or powder guns at initial velocities such that the forward speed of the striker after the initial impact (that effected tumbling) ranged from 250-700 m/s. Tumbling speeds ranged from 0-3600 rad/sec and concomitant yaw angles varied from 0 to 80 degrees. Target specimens consisted of aluminum 6061-T6 with thickness of 1/16 in, 1/8 in,

3/16 in, 1/4 in and 1/2 in; 4130 steel with thicknesses of 1/16 in and 1/8 in; and polycarbonate (Lexan) with thicknesses of 1/8 and 1/4 in. A total of 117 shots were fired. A substantial portion of the data was obtained from high-speed cinematography using a stationary film and a rotating mirror; velocity data were also obtained from interruption of laser beams or energized circuits on paper witness plates that were connected to electronic recording devices. Since the deformation and failure phenomena for thin and moderately thick targets are different, these responses are examined and discussed separately; this has also been done for the development of the corresponding phenomenological models. Based on observations, a model for thin targets was generated that consists of three stages: initial perforation, hole enlargement and petaling. The model for targets of intermediate thickness consists of four stages: erosion, wave propagation (which comprises five different transients), hole enlargement and crack propagation. Transition from one stage to another was proposed. Numerical simulations of the penetration processes were performed by employment of the program DYNA 3D*, an explicit nonlinear three-dimensional finite element code for solid and structural mechanics, that utilized a new slide surface "SAND", which greatly facilitated the simulation of impact problems involving material failure.

All analytical and numerical results were compared with the experimental data, and reasonable correspondence was obtained. It was found that, in general, sufficiently large impact angles (or, alternatively, large enough yaw angles when the oblique angle is zero) may reduce penetration capability of projectiles remarkably and change the trajectory of the projectile substantially, particularly for the thicker targets.

*Courtesy San Diego and Pittsburgh Supercomputer Centers

b) Experimental Arrangement

The general scheme of the experiments has been presented previously (Ruiz and Goldsmith, 1988a, b; Yuan et al, 1992, Goldsmith, Tam and Tomer, Present Final Report, App. A.). A sketch of the set-up is presented in Fig. B-2 that displays the major features of the equipment. This consists of a launching device, initial velocity measurement arrangement connected through a delay to the lighting system for a high speed camera, a tumbling generator that converts the initial translatory motion into a combination of translation and rotation about a transverse axis, the target and its holder; the projectile is arrested by a catcher box.

(i) The projection devices consist of either a 12.7 mm diameter powder gun or a pneumatic gun of similar caliber. The former was used when initial striker velocities were designed to exceed 150 m/s. The projectile was loaded into the gun and either desired amount of powder was emplaced in the cartridge, positioned immediately behind the striker, or, alternatively, the reservoir chamber was filled with nitrogen at the desired pressure. Firing was semi-automatic in that it activated all events (except for the high-speed camera, which was run continuously) and was initiated external to the closed firing chamber.

(ii) The initial velocity was independently measured by the record obtained (and recorded on a Nicolet oscilloscope) from two photosensors impinged upon by a set of two parallel .5 mW He-Ne laser beams (Spectra-Physics Model 155) that were interrupted by the passage of the projectile. For the powder gun, this occurred just outside the muzzle, while two slits in the barrel near the muzzle end accommodated the beam for the gas propulsion device.

(iii) Tumbling was achieved by the impingement of a portion of the front face of the projectile on massive blocks that converted the initial translational

energy into a combination of translation and rotation (tumbling, or pitching). To permit higher initial velocities, a massive 4 x 4 x 1 in block of 6061-T6 aluminum fixed between two angle plates and securely anchored to the base served as the motion converter. Two screws at the bottom of the block served to adjust its vertical position to provide for the desired overlap. The generator angle was also capable of adjustment by means of the screws. The yaw angle at impact with the target is extremely difficult to predict or control since very small changes in the overlap, initial striker velocity and position of the generator along the trajectory produce substantial variations in the angular orientation after tumbling is initiated. The arrangement deliberately permits small variations in the generator location so that the yaw angle can be varied.

Frequently, oblique angles are induced concurrently with tumbling motion. In order for the striker to intercept the target, its holder was designed to also be adjustable in the vertical direction; otherwise, there might not be a target impingement.

(iv) Two sizes of target holders were employed: one for thin targets (1.59-6.35 mm or 1/16-1/4 in) and another for the thicker targets (12.7-25.4 mm, or 1/2 - 1 in). Both had a diameter of 5.5 in. The distance between the tumbling generator and the target holder was reduced to the smallest dimension achievable physically in order to minimize large variations in the impact configuration for identical initial striker speeds and degrees of generator overlap .

(v) Two types of framing cameras were employed in the tests, depending on the impact speed. When the pneumatic gun was used, a Photec IV-A 164 16 mm moving sprocket camera using 100 ft of film at rates from 400-10,000 pps was employed, although the practical upper limit of the framing rate was 5,000 pps. For the powder gun, the Beckman-Whitley model WB-2 was utilized,

providing 35 mm images at rates from 20,000 to 1,000,000 per second, controlled by a rheostat, practical upper limit of 500,000 pps; in most tests, a speed near 45,000 pps was selected. This device uses stationary film and a rotating prism to provide 80 frames, each with an independent lighting path.

(vi) The light source for the illumination of the cameras consisted of a commercial 200 W stroboscopic flash unit, Singer Model Graflex Strobe 250 which had a duration of about 1.8 ms. The light was triggered from the interruption of the second laser beam, the signal being transmitted via a Tektronix Model AM 502 differential amplifier.

(vii) The photographic records were analyzed by means of a Scherr Tumico No. 3305 Optical Comparator), using a magnification of 10. Location were established by recording the position of the projectile at different frame numbers and subsequently dividing by the framing rate. The error in locating the striker in this way compared to that obtained from laser velocity measurement and from analysis of normal translational impacts was found to be about 5%.

(c) Experimental Results and Discussion

A summary of the experimental results is presented in Table 1, and properties of the three target materials employed in the tests are provided in Table 2. Figure B-3 depicts a typical sequence of high-speed photographs of the target response to a tumbling projectile.

In producing yaw and tumbling motion, oblique angles are also generated that range from 0 - 10 degrees. The presence of an oblique angle complicates the impact geometry considerably. To minimize confusion, the nomenclature adopted in defining the geometric and kinematic parameters present in impacts involving yaw and tumbling are shown in Fig. B-1(d) and will be elaborated upon below:

α Yaw angle, the angle between the axis and the velocity vector of the projectile

- β Impact (or Trajectory) angle, the angle between the projectile axis and the normal to the target
 β' Oblique angle, the angle between the trajectory and the target normal

Clearly, from Fig. B-1 (and Fig. 3, Appendix A): $\alpha = \beta + \beta'$.

Furthermore, $\alpha = \beta$ when $\beta' = 0$.

The analysis indicates that, for yaw and tumbling penetration, when an oblique angle is involved, it is the impact angle rather than the yaw angle that plays the dominant role in the penetration process. Rotational speeds of the striker in the present investigation ranged from 0 - 3600 rad/s. Their effects on the perforation process is small (since the duration is relatively short) and were hence neglected. However, the major role of tumbling is to change the impact (or else the yaw) angle, and this will significantly affect the perforation process. The following discussion will focus on the percentage velocity drop $(v/v_0) \times 100$ and the final oblique angle β'_f as a function of the initial translational velocity v_0 and impact angle β as the principal manifestation of the variation of the initial conditions.

(c1) Thin Targets of 6061-T6 Aluminum

Twenty-seven perforation tests were executed for 6061-T6 aluminum targets with a thickness of 3/16 in, with three of these occurring at normal incidence. Representative a posteriori target configurations are presented in Figs. B-4 and B-5. In general, nearly cylindrical plugs were generated when $\beta < 50^\circ$. When β was relatively small, $< 14^\circ$, as shown in Fig. B-4, plastic hole enlargement was found in addition to plugging, resulting in a thickening of the hole edge, as may be observed in this figure. For relatively large values of β , additional damage to the target ensued after perforation, as shown in Fig. B-5. Cracks initiated at the upper portion of the projectile/target interface at both impact and exit sides and propagated outward, constituting "front petaling" (Wu and Goldsmith, 1990a), a tearing process corresponding to

mode III fracture. When β is increased further, a second portion of a plug is ejected from the target. Global target deformation was noted in some tests when v_0 was relatively low.

Figure B-6 depicts a typical test result showing $(\Delta v/v_0)$ and B'_f as a function of impact angle β for given values v_0 and B' , using a multi-input least square curve fitting process. Similarly obtained predictions for the velocity drop and B'_f for a zero oblique angle as a function of β and v_0 are presented in Figs. B-7 and B-8. The first of these shows a linear increase in $(\Delta v/v_0)$ with increasing β . This parameter decreases with an increase of v_0 for a fixed value of β . Figure 8 depicts B'_f as a function of β and v_0 that show an increase of B'_f with increasing β for small values of β , but a decrease beyond a certain threshold when β increases further. In addition, B'_f decreases with increasing values of v_0 .

(c2) Targets of 6061-T6 Aluminum of Intermediate Thickness.

Twenty-four shots were executed on 12.7 mm (0.5 in) targets of this material, of which 19 perforated, two were ricochets, and 3 embedded; two tests occurred at normal incidence. Representative cross sections of these perforated plates are shown in Fig. B-9. In general, plugs were generated and forced out ahead of the projectile except at very high impact angles. The thickness of the plugs was not uniform due to the oblique position of the projectile during the penetration. For $\beta < 25^\circ$, the failure modes of the target plates were the same; an appreciable pile-up of the material near the entrance was observed, as shown in Fig. B-9, Run L5. This results from the oblique position of the projectile which leads to lateral indentation or internal ductile hole enlargement. Examination of the cross sections indicated that the exit cavity diameter was substantially larger than that of the projectile due to plate bulging which was noted in both normal and oblique

perforation. When $\beta > 25^\circ$, failure by fracture ensued as shown in Fig. B-9, Run L6. An additional portion of the plate was detached from the target in addition to the plug. At impact angles greater than 50° , failure consisted of tearing fracture and only a single piece of the target was detached. Global deflections in all instances were very small.

Figure B-10 shows an example of a velocity drop and final oblique angle as a function of impact angle for a specified initial velocity and oblique angle. Figure B-11 depicts the variation of $(\Delta v/v_0)$ as a function of β and v_0 at an oblique angle of zero. It is found that $(\Delta v/v_0)$ increase with β and decreases with v_0 . For $v_0 < 500$ m/s, $(\Delta v/v_0)$ increases very rapidly and attains the ballistic limit quickly. For $v_0 > 600$ m/s, the increase in the velocity drop is initially very large, but the increment decreases rapidly with further increases in β . The figure indicates that the ballistic limit is reached when $\beta = 27^\circ$ for $v_0 = 300$ m/s and $\beta = 42^\circ$ for $v_0 = 400$ ms/s. Four of five non-perforation shots agreed well with this limit. For $v_0 = 600$ m/s, the velocity drop tends to be stabilized at 35% when $\beta > 50^\circ$. An important conclusion drawn from the experiments is that the striker experienced a substantial change in the trajectory after perforation as the result of the impact angle. Figure B-12 shows the prediction of the effect of this parameter and of initial velocity on the final oblique angle of the striker. The change of direction with impact angle is very severe initially and attains a maximum (-53° when $v_0 = 300$ m/s) at an angle of about 18° and subsequently declines to zero quickly, as in a side-on impact ($\beta = 90^\circ$). The figure indicates that β'_f decreases with an increase in v_0 .

(d) Modeling of Yaw and Tumbling Penetration

(d1) Thin Target Deformation Model

Thin targets, which are defined here as those with thicknesses ranging from 1/16 - 1/4 in, are modeled as solids where stress, strain and deformation gradients throughout the thickness do not exist and where, hence, wave propagation in the plate can be neglected. Experimental observations indicate that the penetration process in thin targets can be characterized by three deformation stages. These stages are (i) Initial perforation, (ii) Hole enlargement and (iii) Front petaling. Normally, stages (i) and (ii) will happen contemporaneously except under conditions of normal perforation. It is assumed that stage (iii) occurs only after stage (i) has been completed and the condition of transition from hole enlargement to petaling is made. A finite difference method is used in time integration. The target material is considered to be rigid/perfectly plastic without strain hardening, while the projectile is considered to be totally undeformable.

(d1-i) Initial Perforation

Plugging is initiated upon first contact by the striker with the target. Unlike the case of normal impact, where the projectile touches the entire target contemporaneously, the striker here first contacts the target at a single point (or over a small arc) along the upper edge of the striker/target interface and subsequently extends gradually over a larger area as penetration progresses. This process is similar to the formation of a petal. The portion of the target material in contact with the face of the striker is assumed to instantly attain the same velocity of that portion of the projectile. When yaw and tumbling are present, the oblique position of the projectile leads to lateral indentation during the initial perforation stage. This phenomenon is defined as the contact between the periphery of the

projectile and the entry side of the target; it results in an elliptically-shaped crater. Once the center of the projectile face is intercepted by the target, the contact area becomes semi-elliptical and the indentation ends. Since this process lasts only a very short time, thickening of the target near the crater periphery is very small and is thus neglected in this stage.

The motion of the projectile and plug is based on the energy technique developed by Recht and Ipson (1963). The energy dissipation is divided into 3 parts: E_s , the energy expended at the periphery of the crater in the deformation processes that separate the plug from the target element; E_q is the energy dissipated in plastic deformation throughout the plug that accounts for the plug and the striker reaching a common velocity; and E_m is the kinetic energy of the plug. Care must be exercised in evaluating E_s . Due solely to the presence of the peripheral shear area, it might be expected to be relatively insensitive over a wide velocity range. It is reasonable to assume that the energy per unit area in this process is constant and that the energy can be considered to be proportional to the shear length of the plug. Due to the oblique position of the projectile, this length changes with time. This energy value was obtained from three normal shots on the target.

(d1-ii) Hole Enlargment

For small impact angles, hole enlargement occurs which begins with a non-zero initial radius. The process is not axisymmetric and the thickening of the edge of the hole is not evenly distributed. Thus the Taylor hole enlargement model (Taylor, 1948) is not applicable here. In the present model, a lower bound method, based on Bethe's assumption (1941) is developed and thickening along the edge of the hole is incorporated.

(dl-iii) Front Petaling

When the impact angle is relatively large (i.e., 14° for a 3/16 in thick plate), front petalling occurs. In such situations, Mai and Cotterell's model (1984) is adopted. The energy dissipated include that for shearing fracture of the petal, localized plastic shear in a zone continuous with the torn edges, and the momentum of the petal. The analysis indicated that the bending energy of the petal is small and is hence neglected.

The impact angle for transition from hole enlargement to petalling is given by

$$\alpha_{\text{crit}} = \sin^{-1} \frac{h \tau_s}{2r \sigma_y}$$

where τ_s is the dynamic shear stress and σ_y is the dynamic yield stress.

It is found that, for 6061-T6 aluminum, the critical impact angle for 1/4 in thick plates is 18.8° ; for 3/16 in it is 14° ; it is 9.3° for 1/8 in, and it is 4.5° for 1/16 in thick plates. For 1/8 in thick and 1/16 in thick 4130 steel, α_{crit} is 8.3° and 4.1° , respectively.

Simulations of a total of 50 runs (23 for 3/16, 5 for 1/8 in, 6 for 1/4 in 6061-T6 aluminum; 9 for 1/8 in and 7 for 1/16 in steel) were performed based on the analytical models described above. The results from these models were compared with experimental data and good agreement was found in the final velocity, final oblique angle and crater size except for a few isolated tests; the reasons for the discrepancies in these instances might be attributable to experimental errors. Table 5 presents the comparison of some of the analytical computations and the corresponding experimental results; the superscript e denotes test data and the superscript a represents analytical results. The comparison is also plotted in Fig. 6 for 3/16 in thick 6061-T6 aluminum plates.

(d2) Model for Plates of Intermediate Thickness

Based on experimental observation, the penetration or perforation of plates of intermediate thickness ($\frac{1}{2}$ in.) is divided into four stages:

(i) Erosion, (ii) Wave Propagation, (iii) Hole Enlargement, and (iv) Crack Propagation.

The target plate material is assumed to be rigid/perfectly-plastic and the projectile is again considered to be undeformable. Since the global deflection of the plate is very small for plates of intermediate thickness, it will be neglected in the analysis. From the test results, it is found that crack propagation will not materialize until the impact angle (during penetration) exceeds 25° . The details of the analytical approach will be presented in the final dissertation. Here, the case where the impact angle is less than 25° will be described, i.e., no crack propagation was involved.

(i) Erosion

Due to the impact angle, the projectile will initiate plate contact at a point. The first stage, erosion, commences once the projectile touches the plate. This stage continues until the entire face of the projectile has made contact with the target. As the result of the low impact angle, the penetration depth during this stage is small, and the time interval is very short. Thus, the presence and effect of the distal face of the target can be neglected and the penetration can be considered as a process where the striker enters an infinite medium. In such a case, the assumption of a constant indentation pressure acting normal to the contact area is appropriate--predictions using this maximum have compared well with corresponding experimental data (Hutchings, J. M., 1981). In the present investigation, the pressure is assumed to be equal to thrice the value of the yield stress of the target.

(ii) Wave Propagation

Once the entire face of the projectile is in contact with the target, the wave propagation phase will initiate. Since the striker velocity here is much lower than the plastic wave speed (5,300 m/s), this wave will always propagate away from the face of the projectile. As in perforation at normal incidence, this stage consists of indentation, plug formation, plug separation, plug slipping and post-perforation deformation. A detailed description of this process is found in Liss and Goldsmith, (1984). In the present model, the target is relatively thick; thus, bending effects will be small and are neglected here.

In yawing and tumbling penetration, the projectile moves both axially and laterally and, further, is subject to rotation. Forces act both on the face and on the lateral surface of the striker. The forces acting on the face could still be derived from the case of normal penetration; however, since the projectile rotates, the region of deformation ahead of the face of the striker is assumed to rotate as well. In consequence, the effective thickness of the target also changes. The plug is accelerated by the force from the face of the projectile. Once the plug attains the same velocity as the striker, the plug will separate from the projectile because the latter is decelerated by the resisting forces of the target. The plug velocity at this time is also its final velocity. The lateral surface of the projectile is still acted upon by a pressure which is equivalent to the indentation pressure in the erosion stage. This stage will end once the plug is completely ejected from the target.

(iii) Hole Enlargement

When the plug is completely separated from the target, the third stage, hole enlargement, is initiated. Since the ratio of the target thickness to

the diameter of the projectile is greater than 1 (using the "effective" target thickness here, as described above), a plane strain condition is assumed (Backman and Goldsmith, 1978). Strictly speaking, however, this is a problem between plane strain and plane stress, since the ratio is reduced due to the bulging effect. For such a problem, the pressure due to the symmetric hole enlargement consists of two parts, a static and a dynamic component. Since the normal velocity on the lateral surface of the projectile is small due to relatively small impact angles, the dynamic force, which depends on the normal velocity, is small and is hence neglected here. When using these parameters, it should be noted that the hole enlargement in the present case is different from that of the axisymmetric case. In axisymmetric hole enlargement, the direction of the velocities at each point is radial. Here, however, the velocities of each point have the same direction. The hole enlargement is no longer axisymmetric. The static pressure p can still be regarded as being evenly distributed along the edge of the hole and equal to that for an axisymmetric penetration situation, so that $p = 3.0\sigma_f$ with σ_f as the failure stress.

(iv) Crack Propagation

Cracks are assumed to be produced once the plug is ejected from the target. The contact pressure acting on the projectile will accelerate its rotation and thus increase the impact angle. When the impact angle and the velocities reach critical values, the tearing force will become so large as to initiate crack propagation. The energy dissipated during this process includes plastic deformation, extension of existing cracks and momentum change of the petals.

(d3) Consideration of Voids

In yawing and tumbling penetration, the projectile experiences both translational and rotational motion. This may produce voids in sections of

the target previously indented, but vacated by projectile rotation. In such cases, the actual pressure in this section is zero. Also, when the normal velocity of the projectile at some point is directed inward rather than outward, the pressure must set equal to zero at this point since negative pressures can not exist. Thus, at each instant, it is necessary to check each element of the projectile to see if it is in contact with the target or not. The normal velocity at each position is also checked. If the element of the projectile is in contact with the target, and normal velocity is directed outward, there is pressure; otherwise, the pressure is set to zero. The contour of the deformation is obtained at each instant and checked to ascertain whether contact with the striker exists; it is modified if necessary. The advantage of this method is that once the penetration process terminates, the contour (or the crater size) is determined.

Simulations of 14 runs for $\frac{1}{2}$ in 6061-T6 aluminum plates were performed based on the analytical model indicated above. The computed results were compared with the experimental data, and good correlation was found both in the final velocity and the final oblique angle. Table 4 indicates this information for some of the runs. The computed and measured final velocities of the plug are in good agreement, but the oblique angles are not. This correlation is also shown in Fig. B-10 for the $\frac{1}{2}$ in thick 6061-T6 aluminum plate. Fig. B-13 shows the comparison of calculated and measured cross-sectioned crater profile .

(e) Numerical Simulation

DYNA-3D, an explicit, non-linear three-dimensional finite element code for solid and structural mechanics, using the recently developed type of slide surface "SAND", which expanded the capability of the reproduction of impact

problems including material failure enormously, was used to simulate the event under investigation. Four runs have been performed on the CRAY machine at the Supercomputer Center in San Diego and others at the Supercomputer Center in Pittsburgh, Pa. The material model used here is elastic-plastic with a fracture capability. The failure criteria are the effective plastic strains. The calculations, compared with both the analytical and experimental results, showed substantial agreement. A simulation sequence for yaw and tumbling penetration using DYNA-3D is shown in Fig. B-14, representing Run Z20. Figure B-15 depicts the histories of the velocity and displacement of the center of the projectile. These histories show a very good correlation and are plotted in Fig. B-16. The final results for Run Z20 are presented below:

	Final Velocity m/s	Final Oblique Angle degrees	Crater Size mm
Experiment	400.4	-0.5	33.0
Analytical	394.6	1.6	31.6
Numerical	387.6	2.2	33.0

(f) Closure

The experimental, analytical and numerical modeling of the effect on a thin and moderately thick metallic target by a tumbling projectile has been executed for a variety of targets and initial geometric and kinematic conditions. The effect of tumbling on the perforation process has been clearly demonstrated. The good agreement between the phenomenological/numerical evaluations of the model and corresponding experimental data indicates that the present approach is highly successful in providing a predictive capability for this complicated impact process. Furthermore, the methodology described can serve as a substantial base for a more detailed modeling of the process which could include secondary features disregarded in the present representation.

B. REFERENCES

- Backman, M. E., and Goldsmith, W. "The Mechanics of Penetration of Projectiles into Targets," Int. J. Impact Engng., v. 16, pp. 1-99, 1978.
- Bethe, H. A., "An Attempt at a Theory of Armor Penetration," Frankford Arsenal, 1941. (See Woodward, R. L., Int. J. Mech. Sci., v. 20, pp. 349-359, 1978)
- Hutchings, J. M., "Further Studies of the Oblique Impact of a Hard Sphere against a Ductile Solid," Int. J. Mech. Sci., v. 24, pp. 639-646, 1981.
- Liss, J., and Goldsmith, W., "Plate Perforation Phenomena due to Normal Impact by Blunt Cylinders," Int. J. Impact Engng., v. 2, pp. 37-64, 1984.
- Mai, Y. W., and Cotterell, B., "The Essential Work of Fracture for Tearing of Ductile Metals," Int. J. Fracture, v. 24, pp. 229-236, 1984.
- Recht, R. F., and Ipson, T. W., "Ballistic Perforation Dynamics," J. appl. Mech., v. E30, 384-390, 1963.
- Ruiz, O., and Goldsmith, W., "Controlled Tumbling of Projectiles I: Theoretical Model," Int. J. Impact Engng., v. 7, 101-115, 1988a.
- Ruiz, O., and Goldsmith, W., "Controlled Tumbling of Projectiles II: Experimental Results," Int. J. Impact Engng., v. 7, 285-305, 1988b.
- Taylor, G. I., "The Formation and Enlargement of a Circular Hole in a Thin, Plastic Sheet," Quart. J. Mech. appl. Math., v. 1, p. 103, 1948.
- Wu, E. and Goldsmith, W., "Normal Impact on Moving Targets by Blunt Projectiles--Experimental Study," Int. J. Impact Engng., v. 9, 389-404, 1990a.
- Wu, E., and Goldsmith, W., "Normal Impact on Moving Targets by Blunt Projectiles--Analytical Considerations," Int. J. Impact Engng., v. 9, 405-432, 1990b.
- Yuan, W., et al., "Response of Simulated Propellant and Explosives to Projectile Impact--I. Material Behavior and Penetration Studies," Int. J. Impact Engng., v. 12, 475-497, 1992.

Material	Thickness in	Initial velocity m/s	Impact angle degree	Oblique angle degree	Tumbling speed rad/s
AL6061-T6	1/16 - 1/2	250 - 700	0 - 70	-5 - 15	0 - 3600
Steel 4130	1/16 - 1/8	350 - 700	0 - 60	-5 - 10	0 - 3000
Polycarbonate	1/8 - 1/4	250 - 700	0 - 50	0 - 15	0 - 1500

B) TABLE 1. Illustration of the Material Types, Ranges of Parameters Used in the Experiments

Material	Density kg/mm ³	Dynamic yield strength MPa	Dynamic shear strength MPa	Ultimate tensile strain %
Projectile	7977	~	~	~
AL6061-T6	2780	295	190	20
Steel 4130	7700	560	323	28

B) TABLE 2. Properties of Projectile and Target Materials

Run	Material	Thickness in	Initial Conditions			Final Results			REMARKS		
			v_i m/s	β_i deg	ω_i rad/s	v_f m/s	β_f deg	ω_f rad/s		$\Delta v/v_i$ %	
L5	AL	1/2	338.7	9.0	12.1	74.5	171.8	-40.5	-823.3	49.3	Perforated
L8	AL	1/2	243.2	42.3	46.0	1618.1	---	---	---	100	Ricochet
L2	AL	1/2	353.7	30.8	9.7	1600.3	---	---	---	100	Ricochet. Plug sheared out.
H15	AL	1/2	357.6	67.6	11.9	3627.3	---	---	---	100	Embedded
L6	AL	1/2	470.3	24.7	4.3	1088.8	251.5	-29.7	-969.5	46.5	Perforated
L15	AL	3/16	476.7	0.0	6.3	254.1	451.5	0.8	920.0	5.3	Perforated
Z13	AL	3/16	395.4	13.9	7.2	350.6	343.0	-2.2	529.0	13.3	Perforated
L24	AL	3/16	511.0	21.2	8.3	1604.0	403.7	1.5	1156.6	21.0	Normal perforation
J22	AL	1/4	423.5	45.8	10.3	2175.9	267.2	4.6	1420.1	36.9	Perforated
X1	AL	1/4	575.8	11.0	6.4	701.4	494.6	-6.3	1080.0	14.1	Perforated
J2	AL	1/8	684.6	3.8	4.5	259.2	652.9	1.2	2012.3	4.6	Perforated
J4	AL	1/8	395.0	32.2	10.3	1267.9	355.7	5.7	2196.8	9.9	Perforated
Y9	AL	1/16	403.0	1.7	-7.6	-347.8	397.3	-2.7	-1152.7	1.4	Perforated
I2	AL	1/16	81.0	46.8	0.0	914.2	---	---	---	100	No perforated. Ballistic limit
Z20	ST	1/8	458.7	22.0	7.3	1031.3	400.4	-0.5	1016.8	12.7	Perforated
J8	ST	1/8	418.1	51.4	10.5	2753.9	314.0	9.1	2557.7	28.4	Perforated
G1	ST	1/16	627.2	14.3	2.8	1872.5	581.0	1.6	1926.1	10.9	Perforated
J15	ST	1/16	299.7	63.4	17.3	3012.1	264.4	15.7	3103.6	14.0	Perforated
Y5	PL	1/4	334.0	46.7	6.9	1382.7	---	---	---	---	Perforated. Film not clear
A6	PL	1/4	563.2	0.0	0.0	0.0	542.9	0.0	0.0	3.6	Normal perforation
Y2	PL	1/8	271.1	37.4	12.4	1061.1	235.1	11.6	696.6	13.5	Perforated
Q9	PL	1/8	248.8	0.0	0.0	0.0	240.9	0.0	0.0	3.2	Normal perforation

B) TABLE 3. Experimental Results of Perforation of Plates by Yaw and Tumbling Cylindrical Projectiles

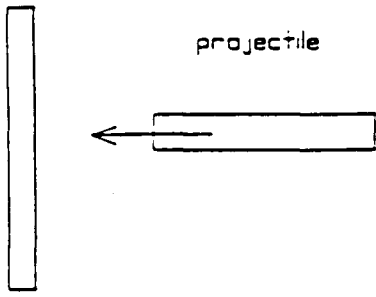
Run	Initial Conditions				Final Results									
	Projectile				Projectile					Plug				
	v_i m/s	β_i deg	β_i deg	ω_i rad/s	v_f^a m/s	β_f^e deg	β_f^a deg	ω_f^e rad/s	ω_f^a rad/s	v^e m/s	v^a m/s	β^e	β^a	
L4	404.2	17.8	-4.8	1075.4	253.2	-40.4	-41.7	-265.5	-90.3	345.6	299.3	1.5	-26.9	
L5	338.7	9.0	12.1	74.5	171.8	-40.5	-50.8	-823.3	250.4	216.6	215.4	-22.5	-19.7	
L9	523.1	10.9	6.8	433.7	580.8	-24.9	-28.2	-2033.4	-1745.0	426.2	406.0	-4.2	-16.2	
L11	476.3	12.3	-3.4	69	361.5	25.2	-24.1	43.3	-403.0	410.9	386.8	1.5	-16.6	
L13	505.1	6.6	4.6	1674.0	394.8	-19.4	-23.8	-882.9	-1174.1	409.9	404.1	-8.2	-12.9	
H14	635.2	2.3	2.9	516.6	550.7	-7.4	-6.2	-109.3	-832.6	553.8	543.5	-1.6	-3.8	
L33	564.7	0.0	0.0	0.0	478.4	0.0	0.0	0.0	0.0	514.3	478.5	0.0	0.0	
L34	401.7	0.0	0.0	0.0	323.0	0.0	0.0	0.0	0.0	348.7	320.4	0.0	0.0	

B) TABLE 4. Experimental and Analytical Results of Perforation of 1/2 in. AL6061-T6 Plates by Yaw and Tumbling Projectiles.

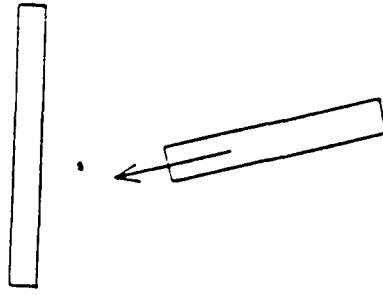
Run	Initial Conditions				Final Results									
	Projectile				Projectile					Crater				
	v_i m/s	β_i deg	β_i deg	ω_i rad/s	v_f^a m/s	β_f^e deg	β_f^a deg	ω_f^e rad/s	ω_f^a rad/s	v^e m/s	v^a m/s	δ^e m/s	δ^a m/s	
L15	476.7	0.0	6.3	254.1	451.5	446.5	0.8	0.0	920.0	-84.9	17.0	17.1	17.1	
L16	336.2	5.5	7.6	276.1	287.0	296.9	-9.3	-9.7	69.0	-1016.3	22.0	20.3	20.3	
L24	511.0	21.2	8.3	1604.0	403.7	447.6	1.5	1.2	1156.6	1798.8	33.0	31.6	31.6	
Z1	315.0	29.4	11.7	1023.2	238.2	224.1	0.0	-3.1	2349.6	1794.2	37.0	35.8	35.8	
Z13	395.4	13.9	7.2	350.6	343.0	339.7	-2.2	-6.2	529.0	689.4	28.0	26.1	26.1	
K3	525.2	0.0	0.0	0.0	498.5	499.3	0.0	0.0	0.0	0.0	14.0	12.7	12.7	

B) TABLE 5. Experimental and Analytical Results of Perforation of 3/16 in AL6061-T6 Plates by Yaw and Tumbling Projectiles.

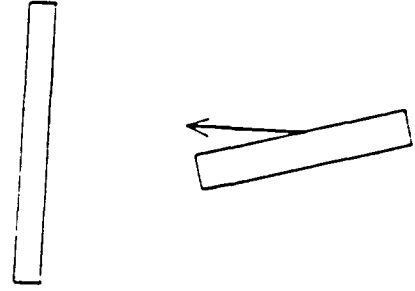
target



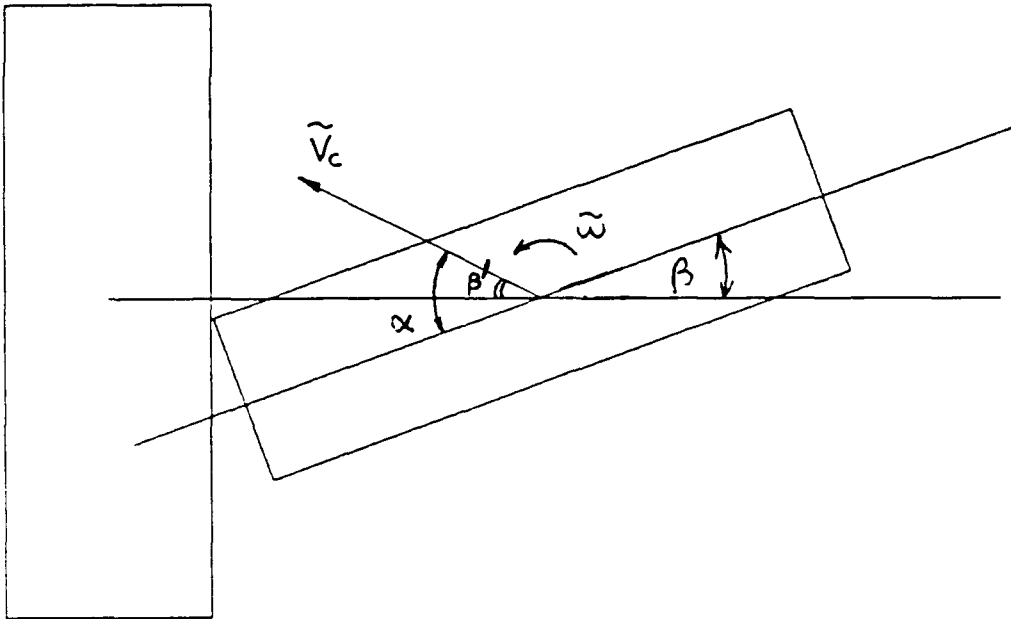
(a) normal impact



(b) oblique impact

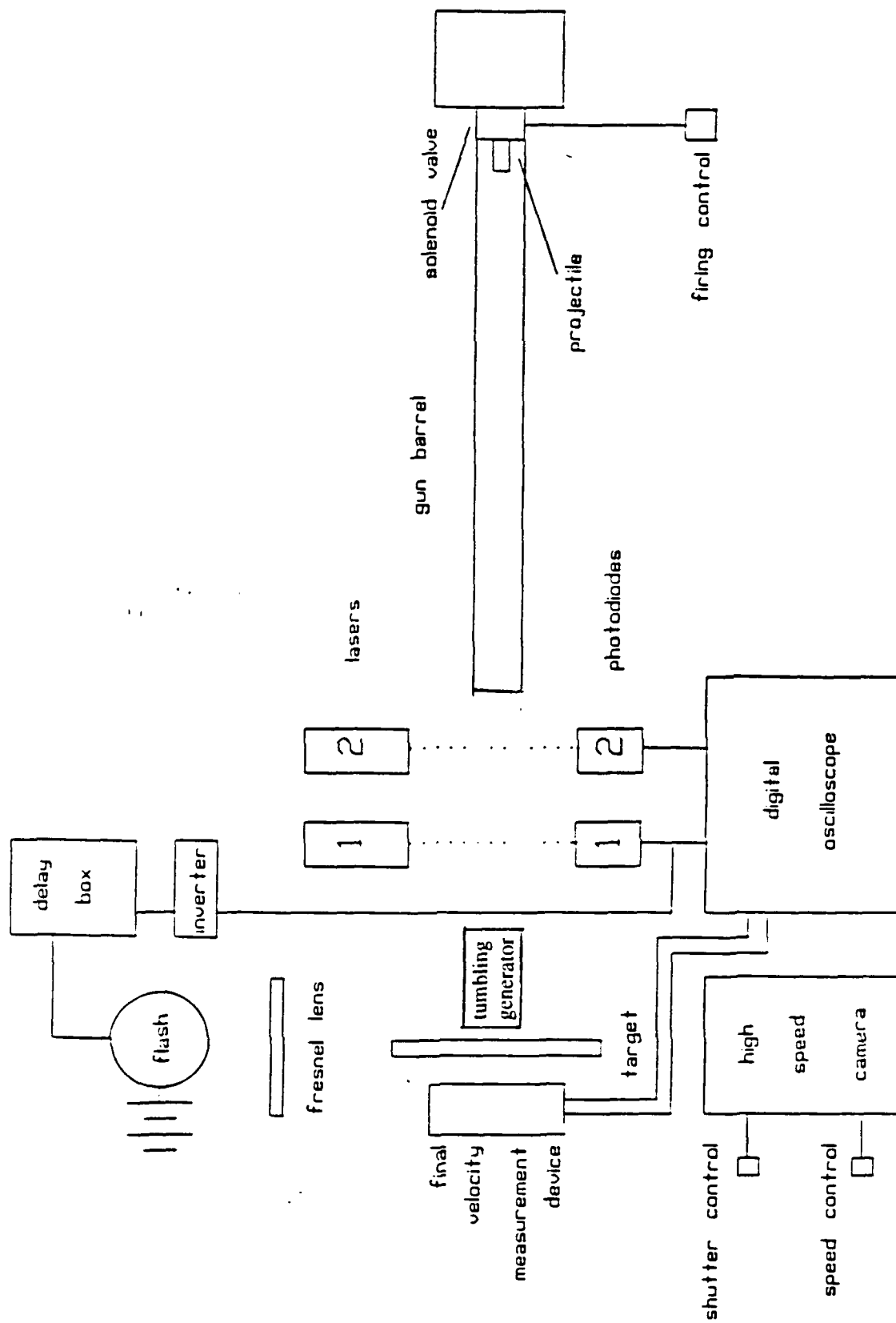


(c) yaw impact



(d) Yaw, oblique and tumbling impact

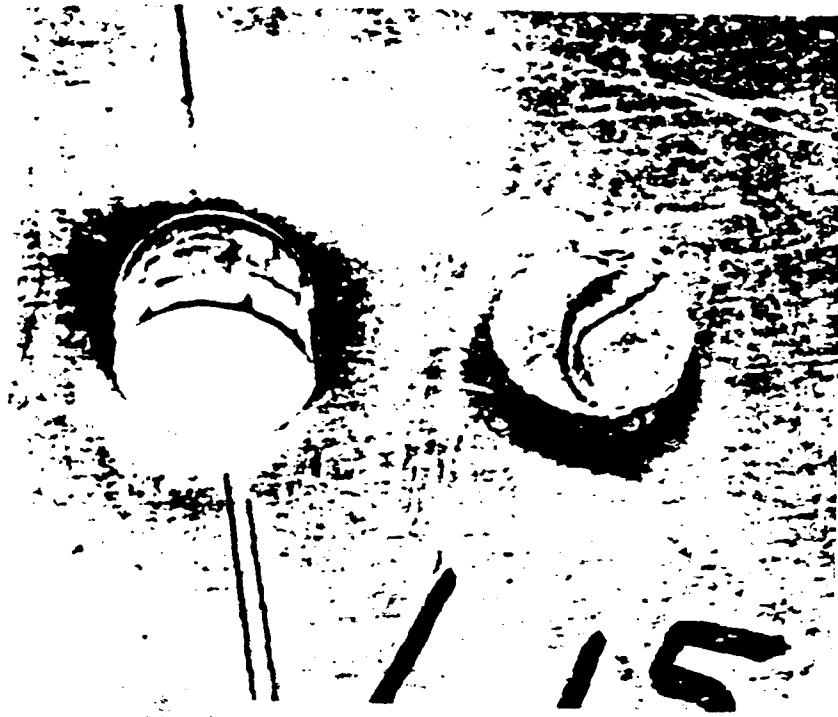
B) Fig. 1 Various Impacts



B) Figure 2. Experimental setup for yaw and tumbling impact



B) Figure 3. Typical Beckman-Whitney framing camera sequence showing the motion of the projectile before, during and after the impact. Run Z13. The framing rate is 22.3 $\mu\text{s}/\text{frame}$



(a) Impact Side



(b) Distal Side

B) Figure 4. Impact and distal sides of 3/16 in. thick AL6061-T6 target after yaw and tumbling impact by a cylindrical projectile, Run L15

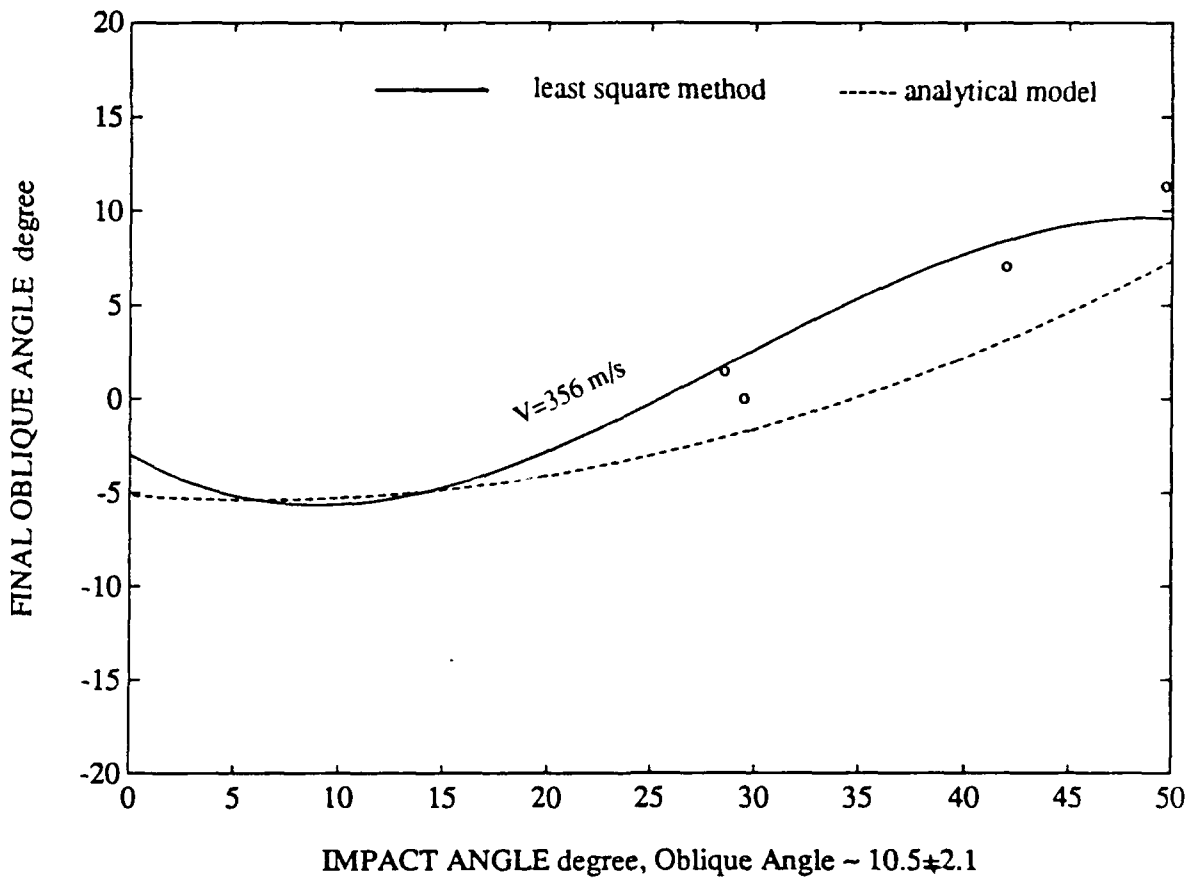
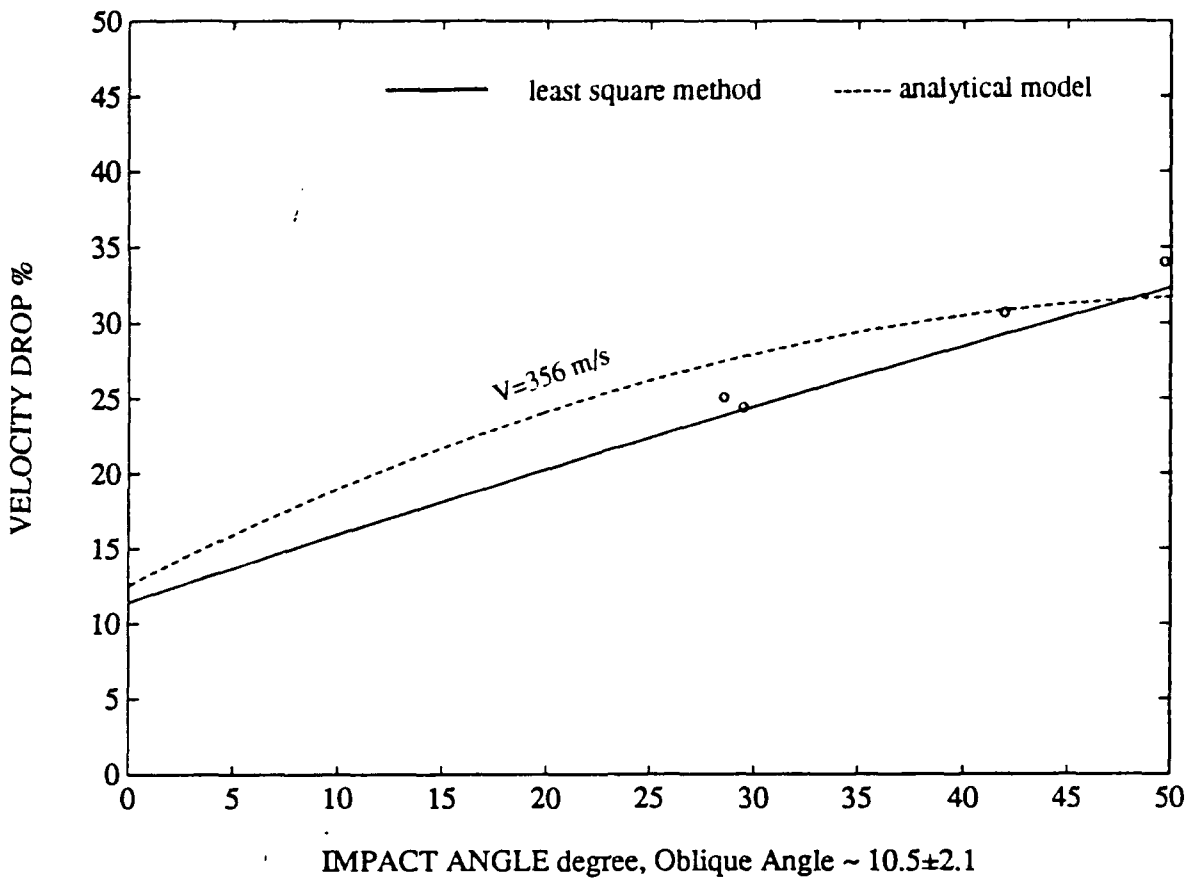


(a) Impact Side

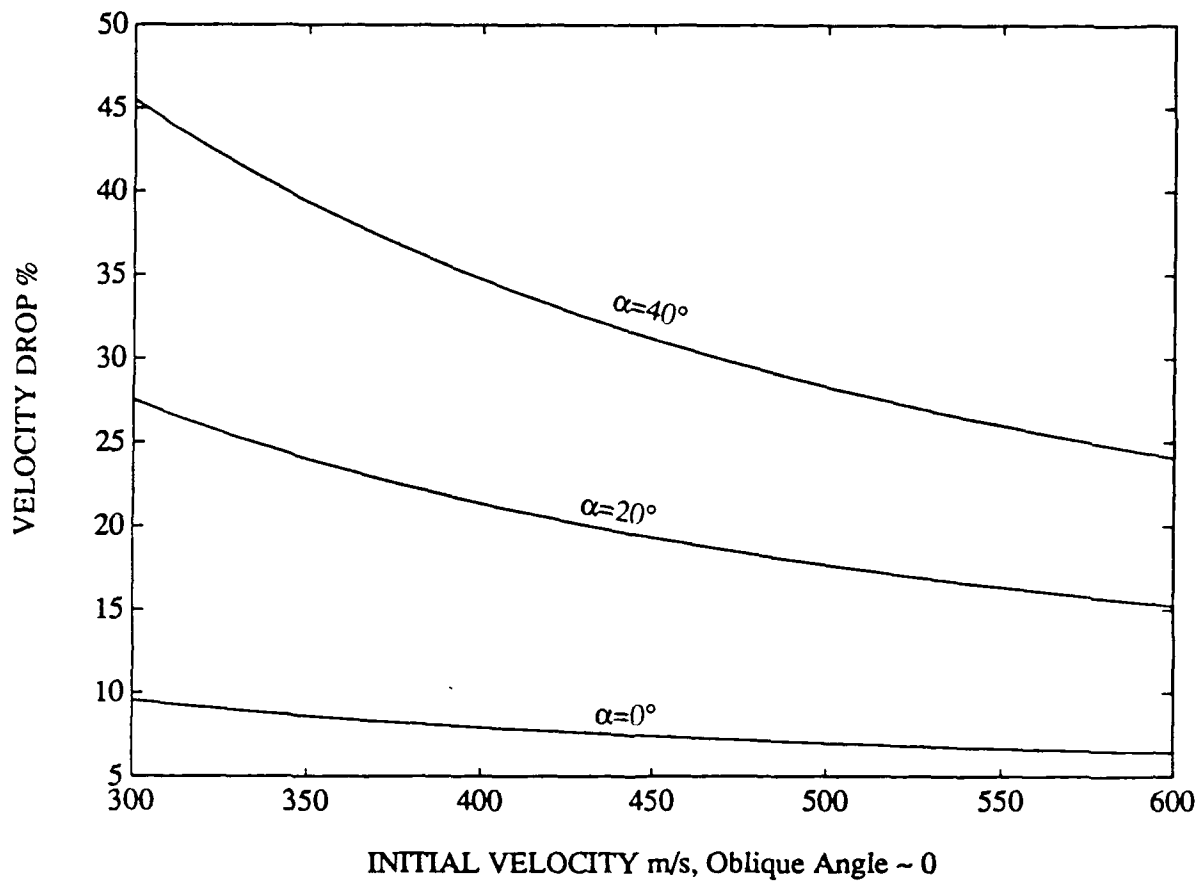
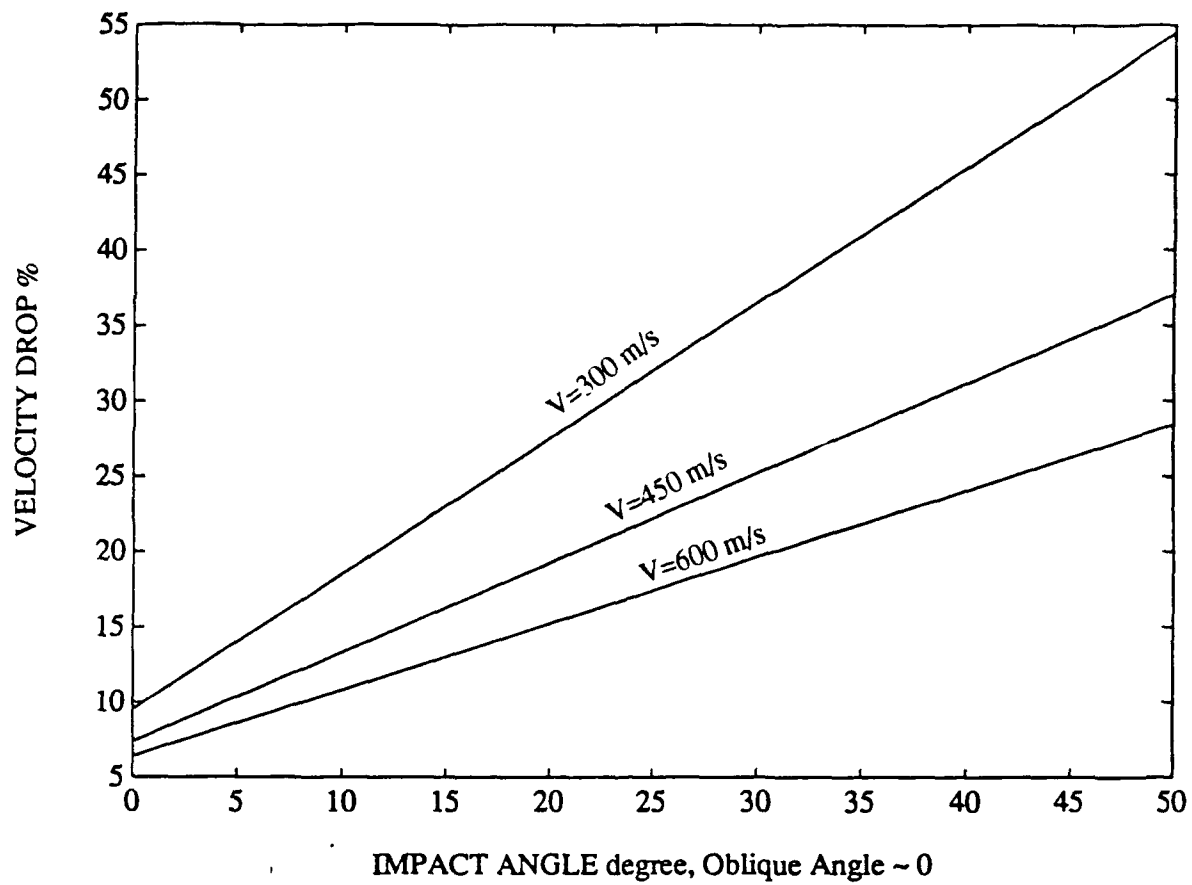


(b) Distal Side

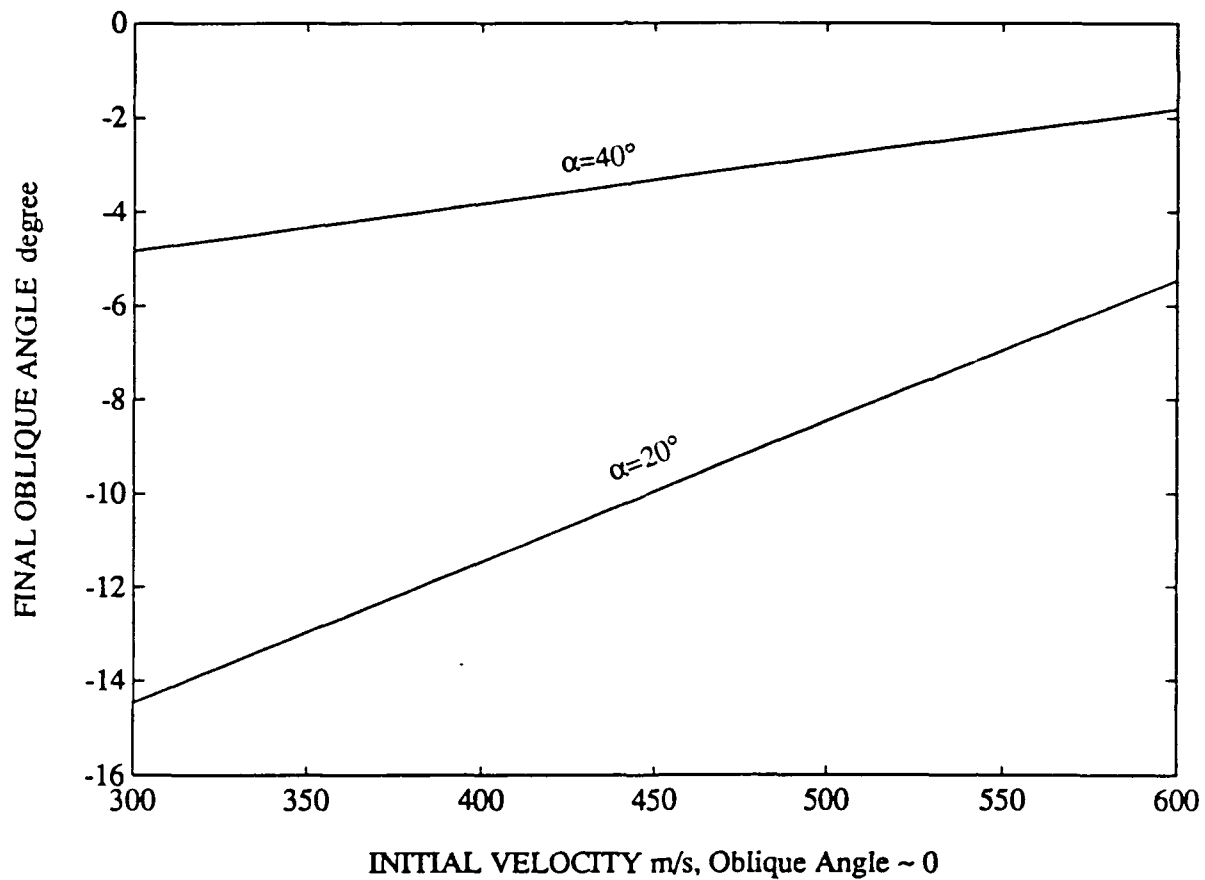
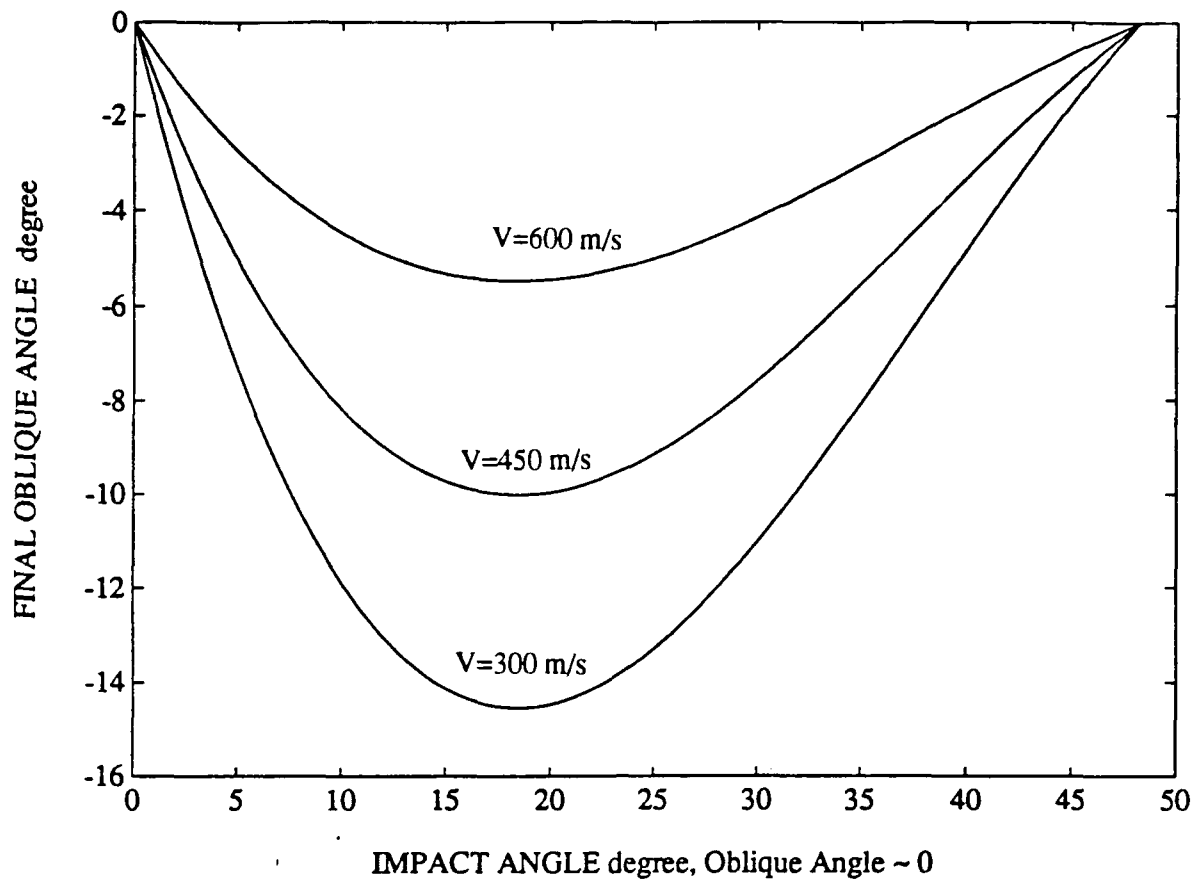
B) Figure 5. Impact and distal sides of 3/16 in. thick AL6061-T6 target after yaw and tumbling impact by a blunt-faced projectile. Run L24



B) Figure 6. Experimental and analytical results of velocity drop and final oblique angle for 3/16 in AL6061-T6 targets struck by hard-steel cylindrical projectiles as a function of initial impact angle



B) Figure 7. Prediction of velocity drop for 3/16 in AL6061-T6 targets struck by hard steel cylindrical projectiles as a function of initial impact angle and initial velocity based on experimental data and curve fitting technique



B) Figure 8. Prediction of final oblique angle for 3/16 in AL6061-T6 targets struck by hard-steel cylindrical projectiles as a function of initial impact angle and initial velocity based on experimental data and curve fitting technique

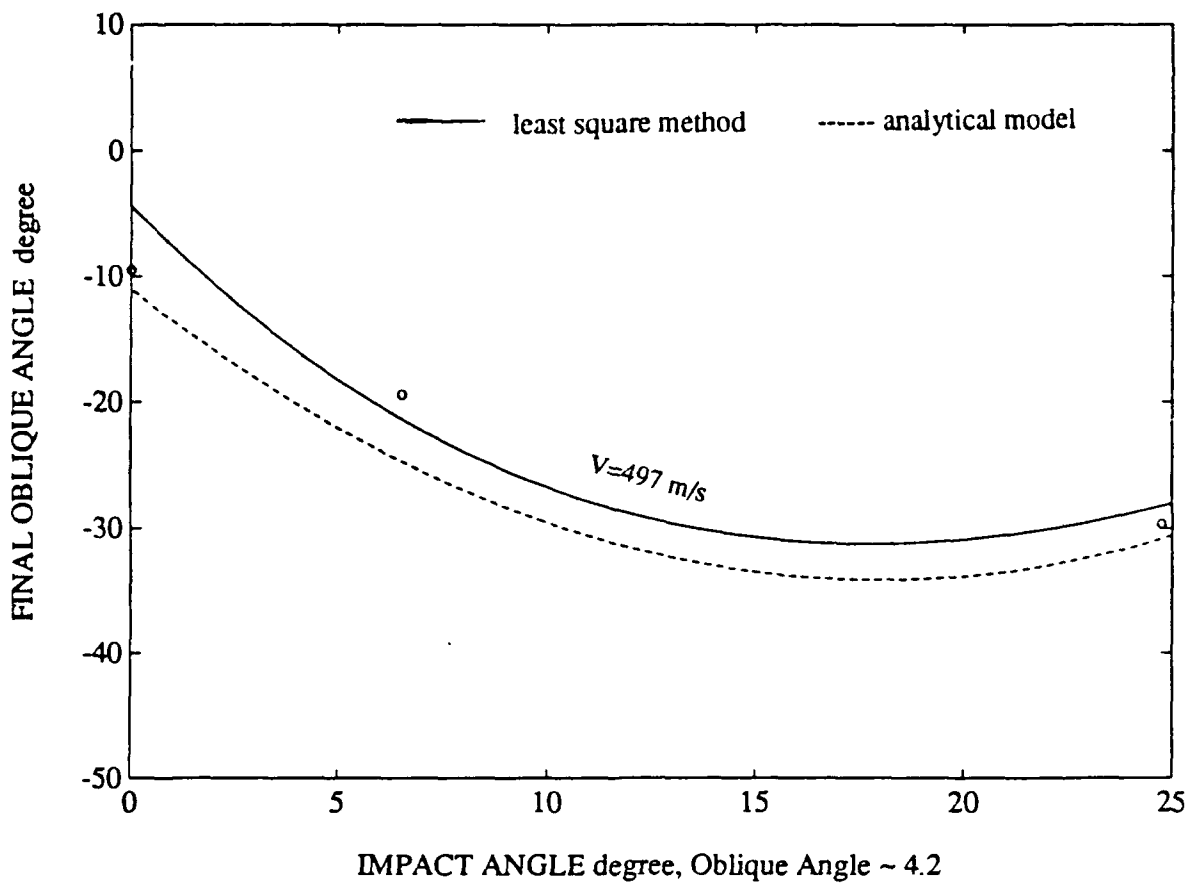
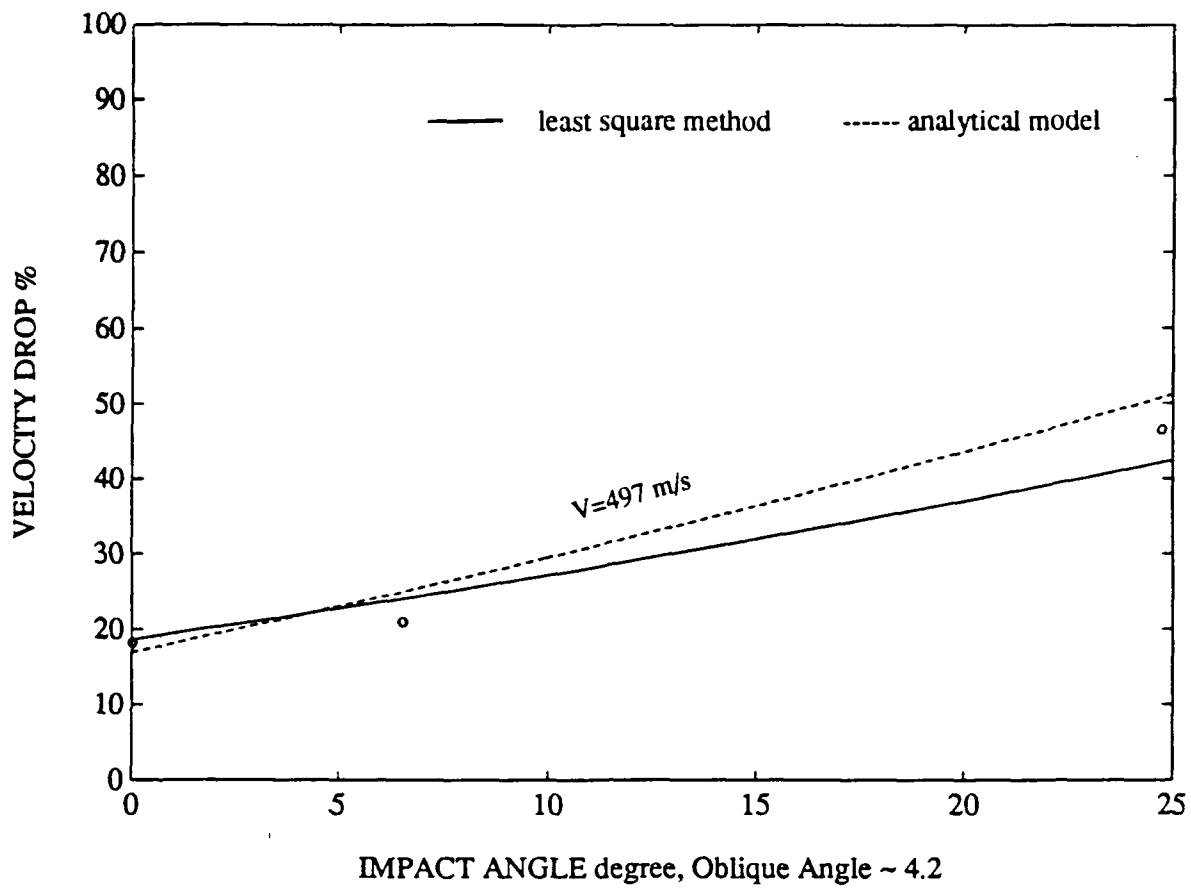


Run L5

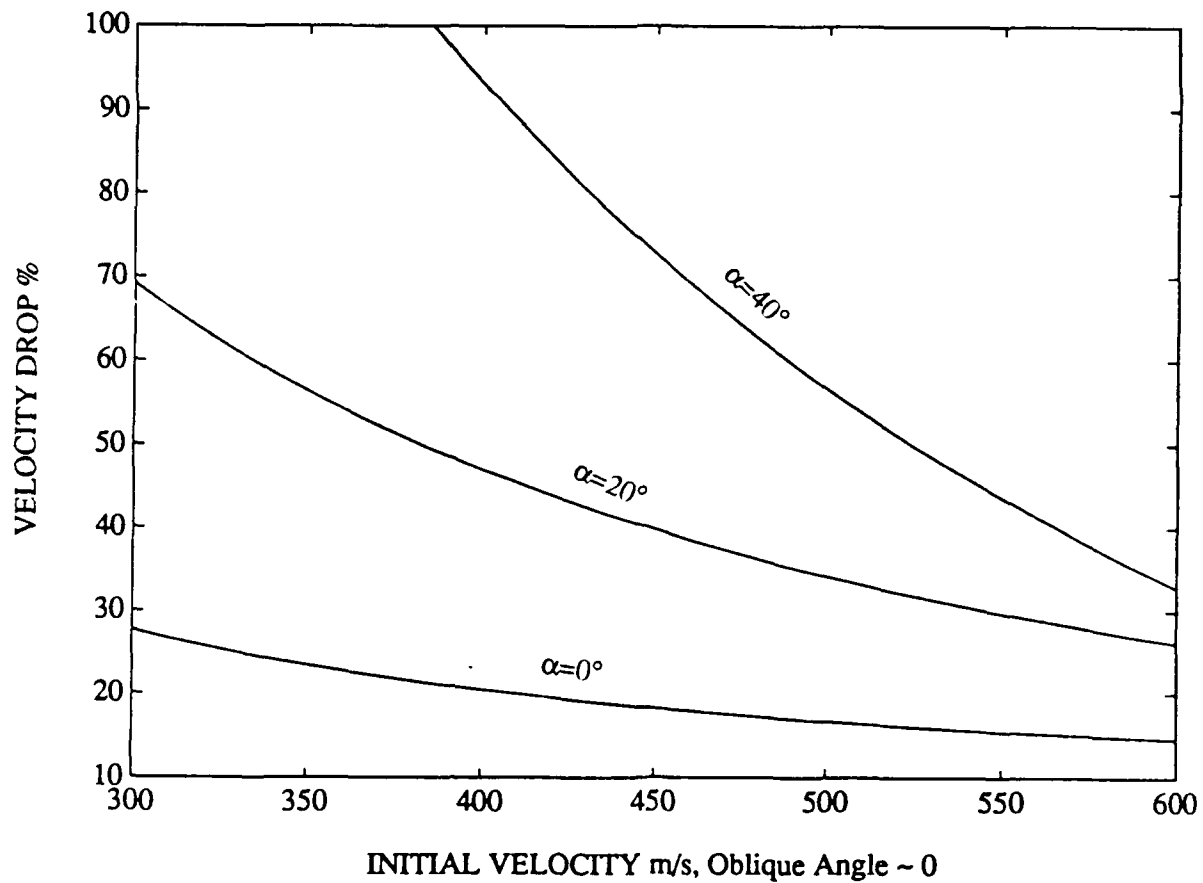
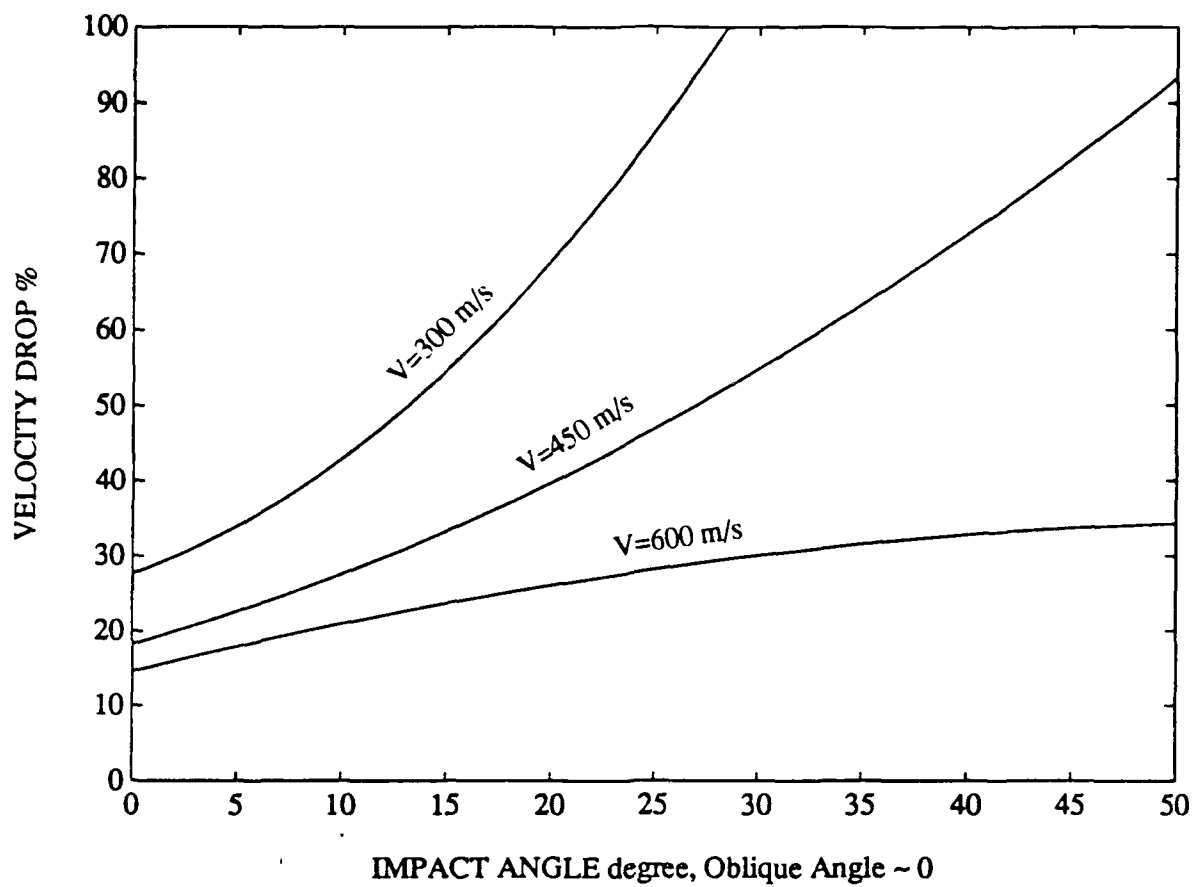


Run L6

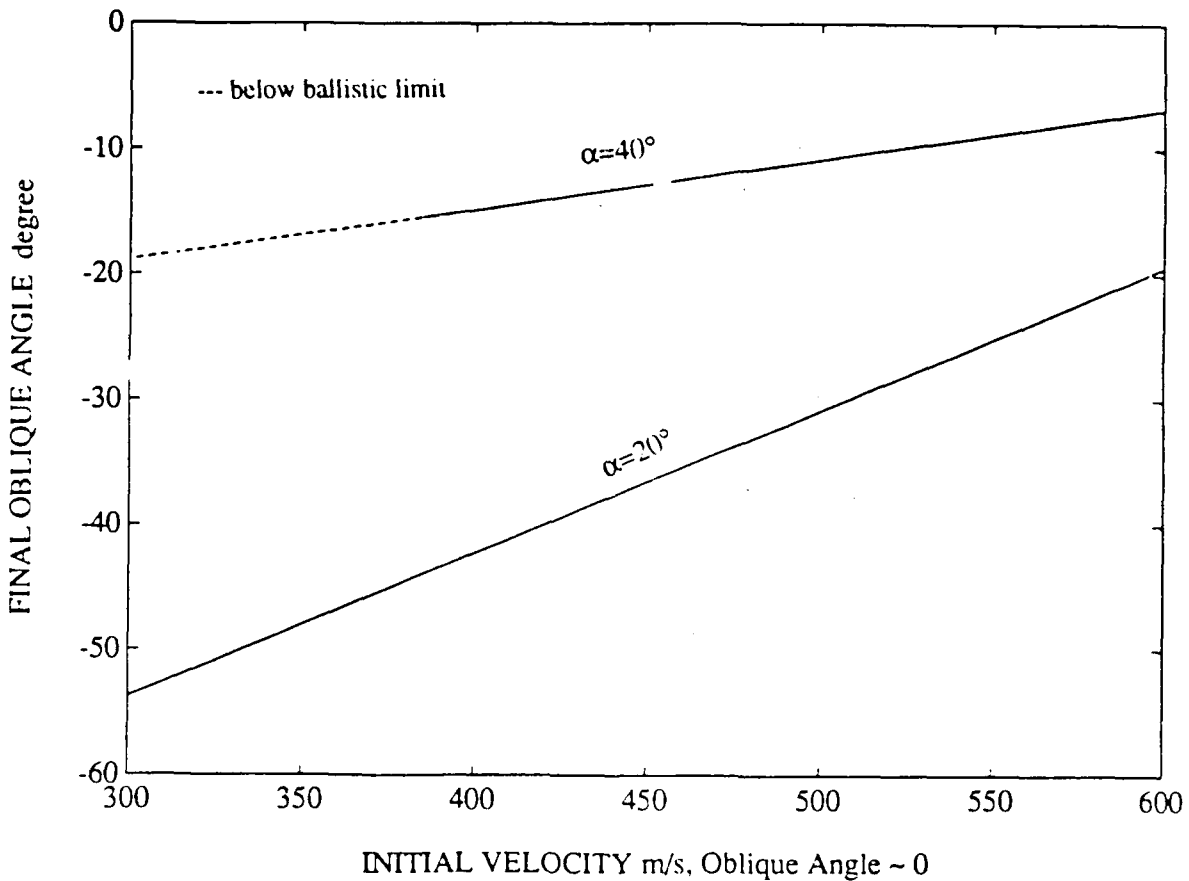
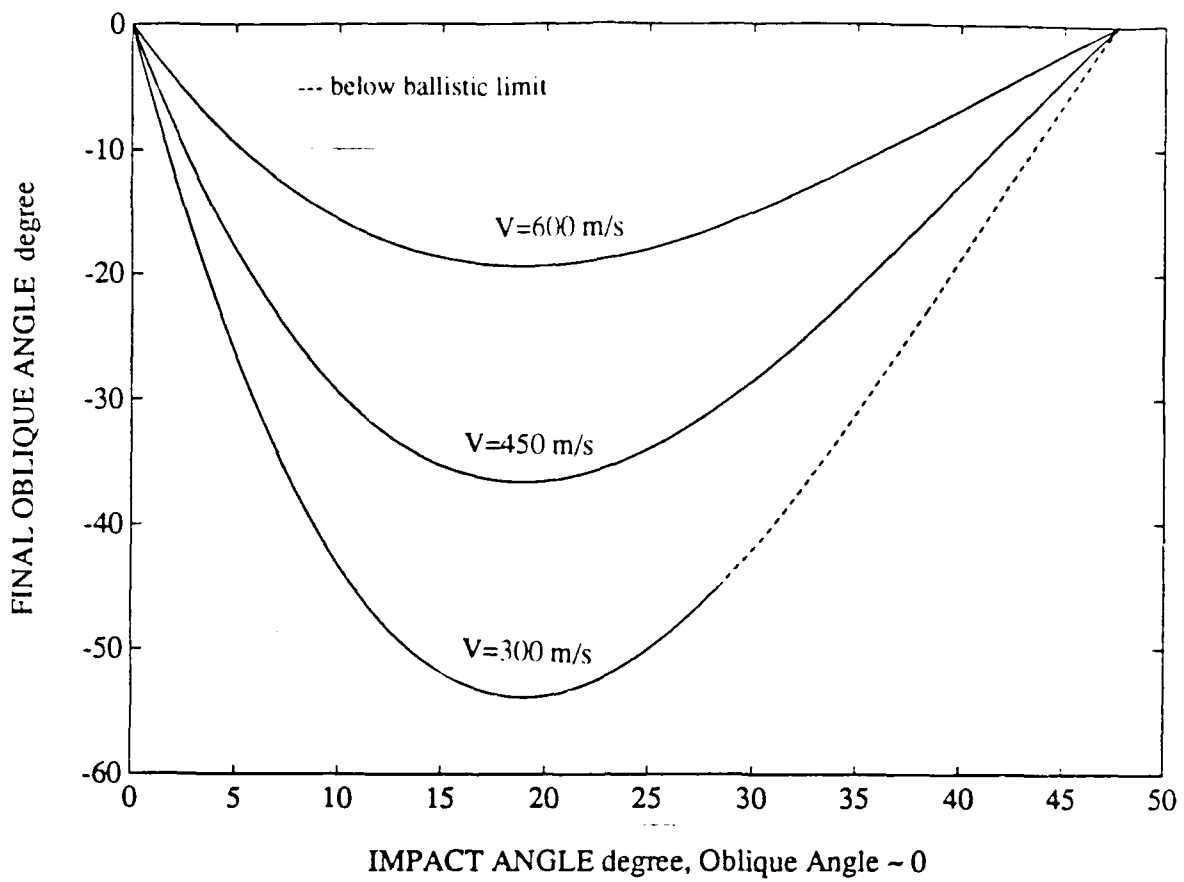
B) Figure 9. Cross section of 0.5 in thick AL6061-T6 target after yaw and tumbling impact by a cylindrical projectile



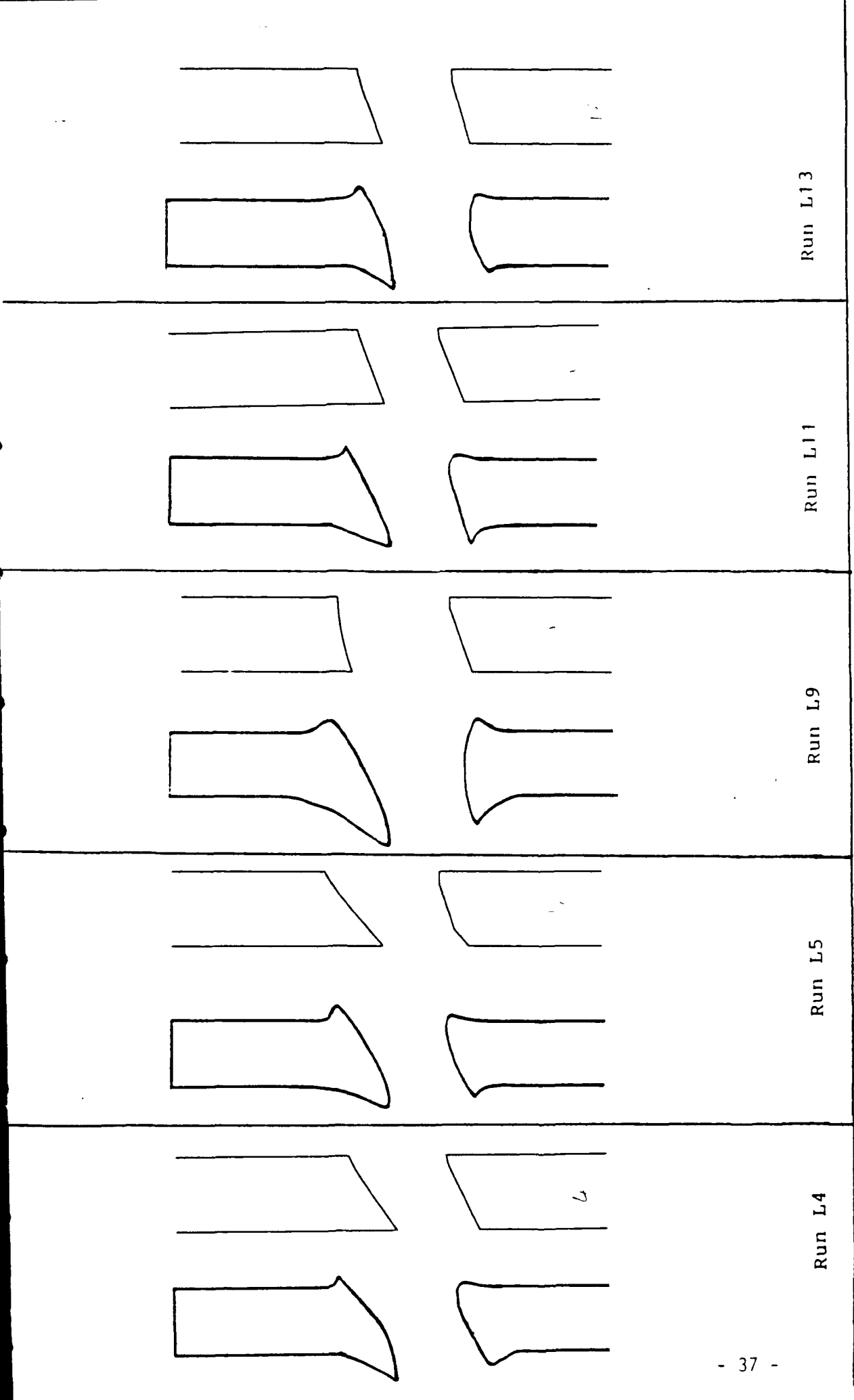
B) Figure 10. Experimental and analytical results of velocity drop and final oblique angle for 1/2 in AL6061-T6 targets struck by hard-steel cylindrical projectiles as a function of initial impact angle



B) Figure 11. Prediction of velocity drop for 1/2 in AL6061-T6 targets struck by hard steel cylindrical projectiles as a function of initial impact angle and initial velocity based on experimental data and curve fitting technique

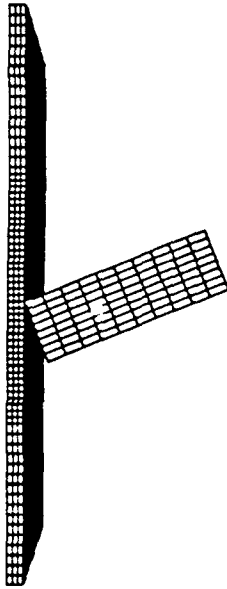


B) Figure 12. Prediction of final oblique angle for 1/2 in AL6061-T6 targets struck by hard-steel cylindrical projectiles as a function of initial impact angle and initial velocity based on experimental data and curve fitting technique



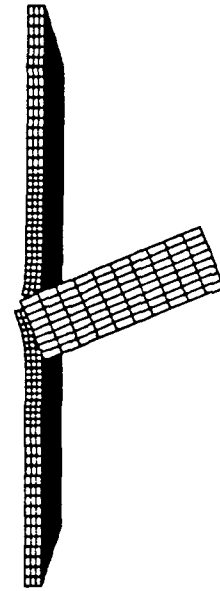
B) Figure 13. Cross-sectioned crater profile formed by a projectile
 Experimental results are shown on left
 Analytical results are shown on right

Z20 steel plate target(in,sec,lb sec²/in)
time = 0.00000E+00



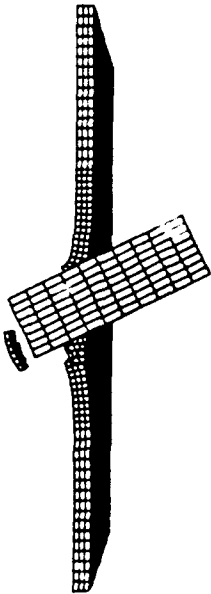
disp. scale factor = 0.100E+01 (default)

Z20 steel plate target(in,sec,lb sec²/in)
time = 0.10000E-04



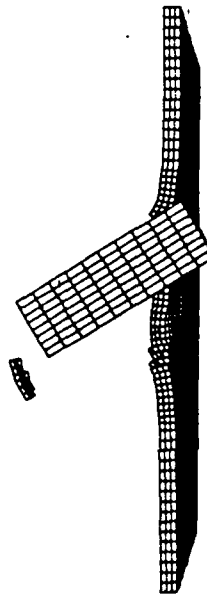
disp. scale factor = 0.100E+01 (default)

Z20 steel plate target(in,sec,lb sec²/in)
time = 0.40000E-04



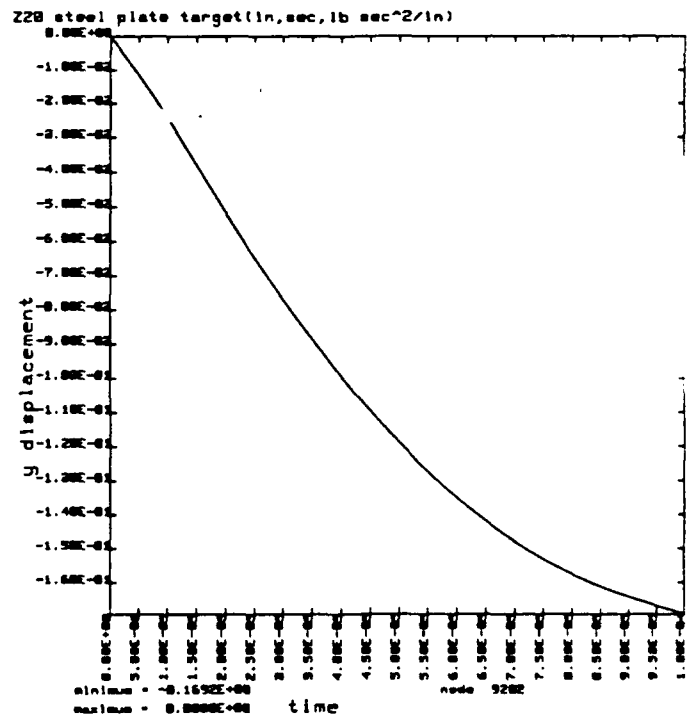
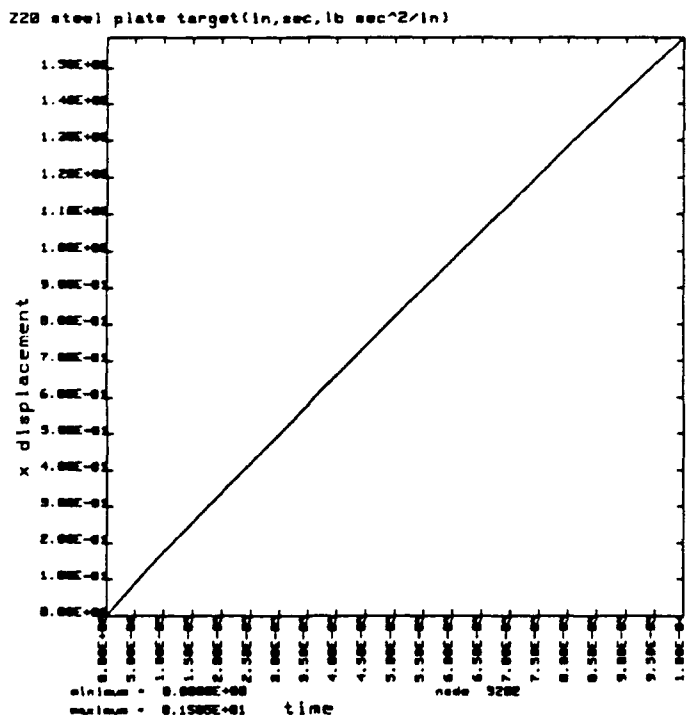
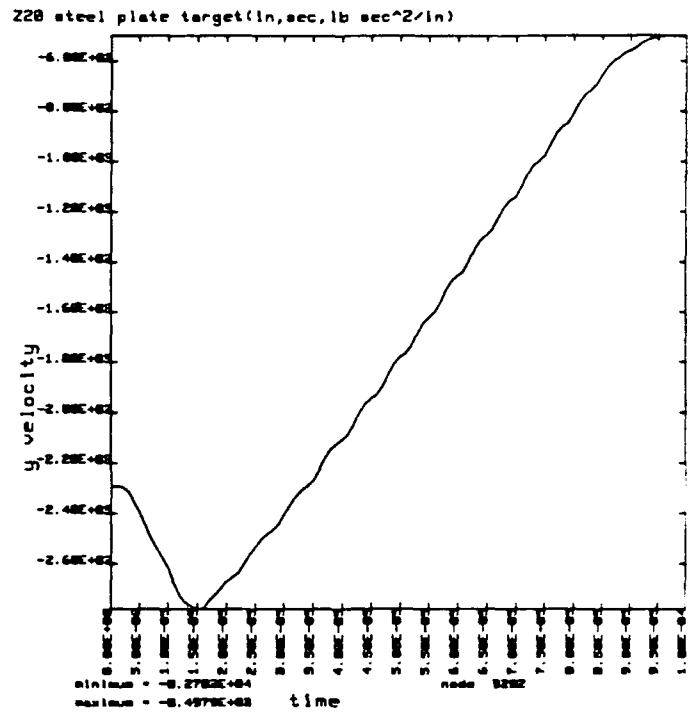
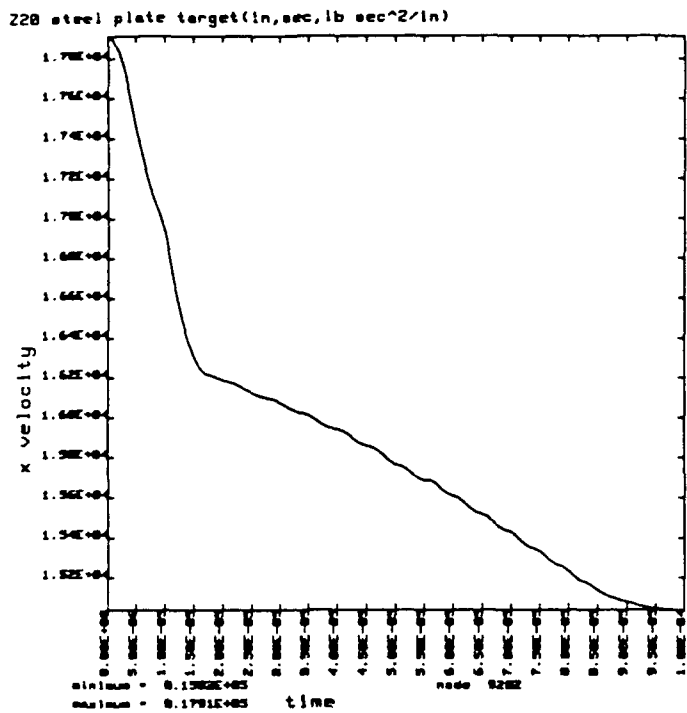
disp. scale factor = 0.100E+01 (default)

Z20 steel plate target(in,sec,lb sec²/in)
time = 0.80000E-04

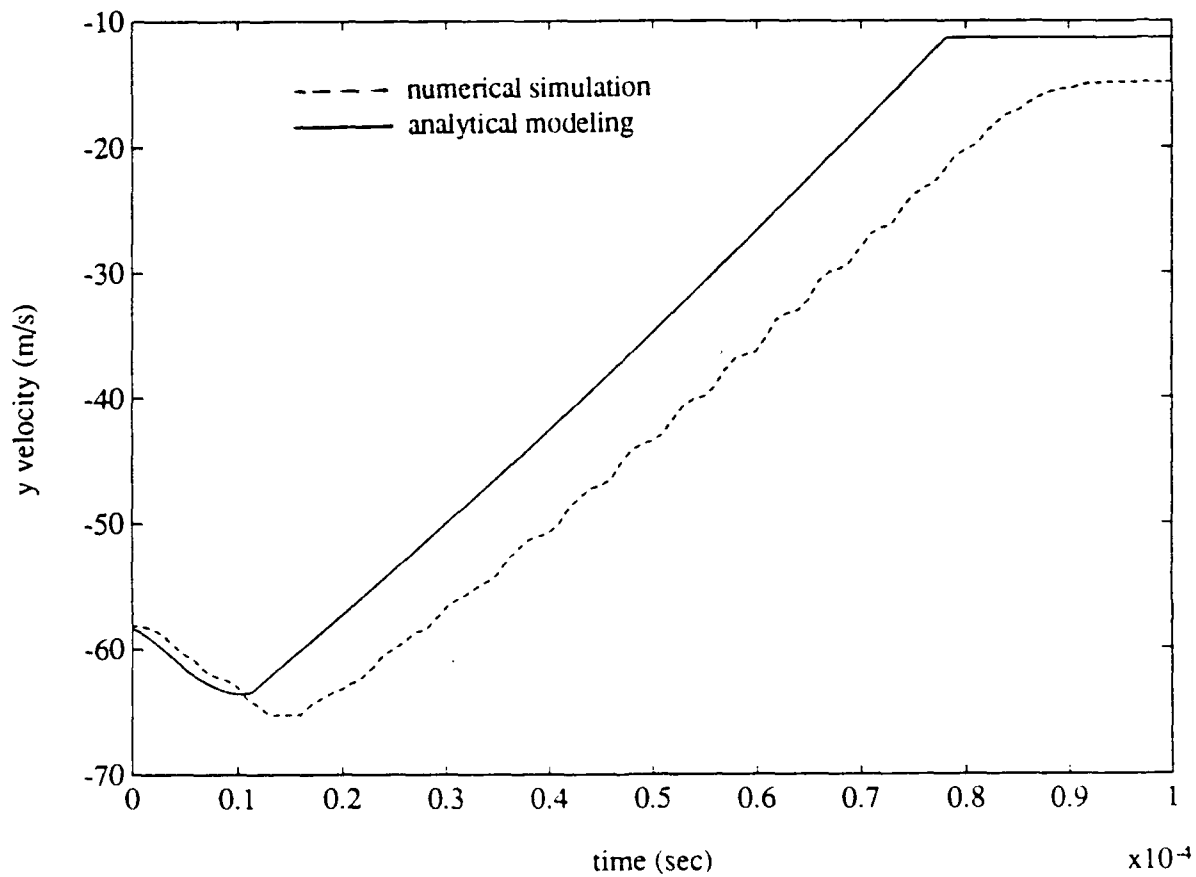
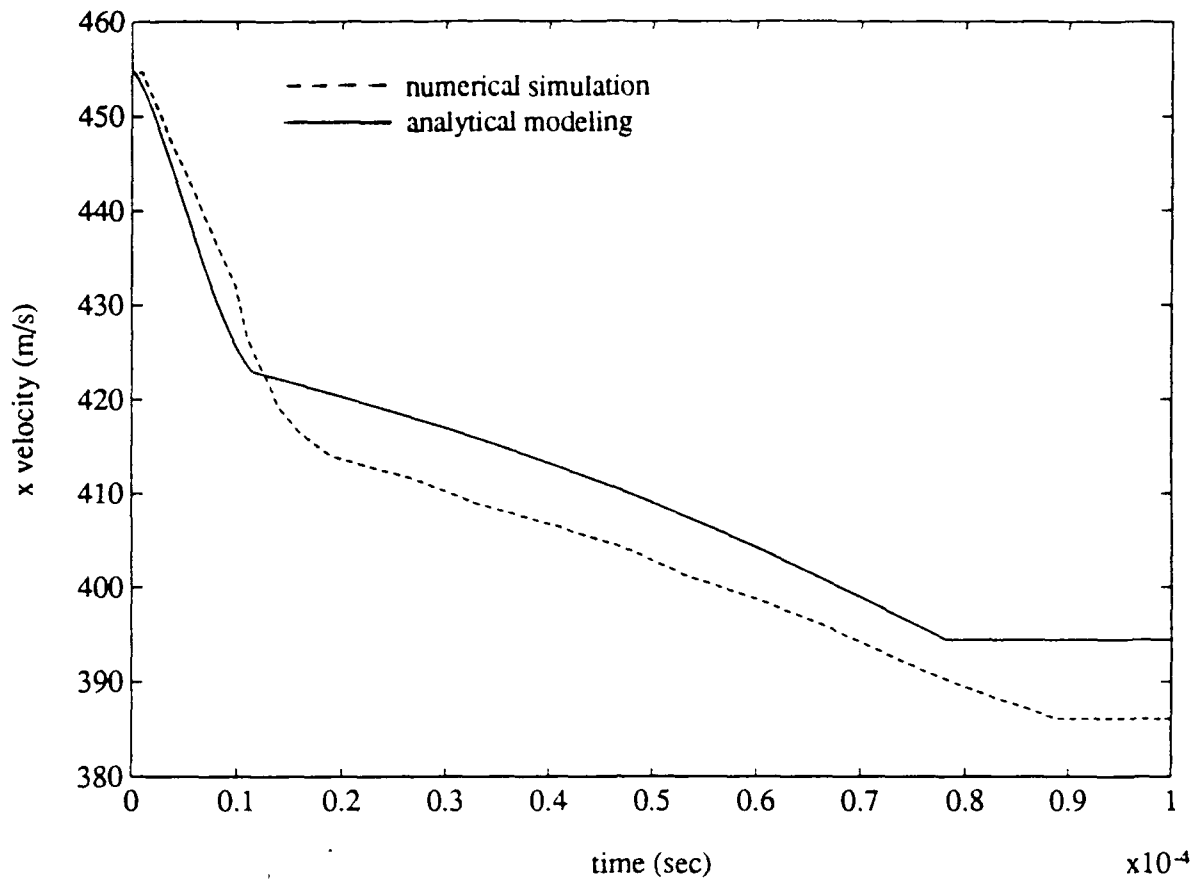


disp. scale factor = 0.100E+01 (default)

B) Figure 14. A simulation sequence of yaw and tumbling penetration of 1/8 in steel 4130 target by a hard-steel cylindrical projectile using DYNA3D. Run Z20



B) Figure 15. Histories of velocity and displacement of the center of the projectile, Run Z20



B) Figure 16. Comparison of histories of velocity of the center of the projectile in two directions between analytical modeling and numerical simulation, Run Z20

C. IMPACT ON MOVING TARGETS

a) Objective and Methodology

The purpose of this portion of the investigation was the development of an experimental technique that would produce impact of projectiles travelling at ballistic speeds on targets moving orthogonal to the striker trajectory at speeds up to 133 m/s. The target velocity thus is nearly 300 mph, that encompasses many flight vehicles. A previous investigation of this subject (Wu and Goldsmith, 1990a, 1990b) employed two circular plates at the opposite ends of a rotating arm as targets, but the synchronization used in this arrangement was not sufficiently accurate to be employed at higher speeds. Thus, continuous annular circular disks composed of aluminum, steel and polycarbonate, attached to a rotor whose motion provided the desired tangential velocity at the impact point, served as targets and, in most, instances, permitted repeated utilization since impact points were widely dispersed. Concern about the imbalance created by perforations producing deleterious effects on the motor and bearings prompted the incorporation of an extremely rapid electromagnetic brake that could arrest the system within 3 seconds. However, in practice, this apprehension proved to be unfounded, and the system was brought to rest solely by air resistance and bearing friction.

Concomitantly, the phenomena extant in this type of experimentation were studied phenomenologically, based on the earlier analysis, but using improved modeling based on experimental observation. In particular, the description of the failure mode during plugging and the deformation and fracture processes during petaling were updated. Additionally, a numerical study of the event was executed, using the finite element code DYNA-3D which has been upgraded to permit the description of failure processes. The program was run on a CRAY X-MP/48 Supercomputer. The results from the three types of approaches were

compared.

b) Experimental Arrangement

The principal components of the setup consisted of the propulsion device, the rotational target arrangement, the data acquisition system including optical and electronic instrumentation, including the stroboscopic light source, and auxiliary apparatus such as velocity measuring schemes, a catcher box and data reduction equipment.

(i) Continuous circular annular disks with an outer diameter of 24-26 in and an inner diameter of 14 in with thicknesses ranging from 1/16 to 3/8 in, consisting of 6061-T6 aluminum, CR1010 steel and polycarbonate, were attached to a motor-driven disk by means of set screws. Impact occurred 10 in from the shaft center. The desired tangential velocity was produced by a pulley transmission system; different pulley sizes produced different tangential speeds.

The motor size was selected based on an upper limit of angular acceleration time, selected to be 10 seconds, to attain the desired rotational speed (to avoid overheating) and needed to account for losses due to mechanical friction and air resistance. The acceleration depended principally upon the inertial moment of the target and attached rotational components; the maximum value of this moment of inertia was 19.3 lb-ft². The target diameter was checked against the allowable stresses produced by centrifugal action. For the maximum rotational speed of 5000 rpm, the effective stresses were found to be 1,800, 5,400 and 850 psi for aluminum, steel and polycarbonate disks with a 24 in outside and a 14 in inside diameter; this represents a factor of safety of at least 11 relative to the material yield stress. Other target speeds employed were 3500 and 2000 rpm.

Based on these considerations, the maximum torque load during acceleration was computed to be 25.7 ft-lb requiring a minimum 10.37 hp motor. The

driver selected for the operation was a 3500, 15 hp Dayton motor supplemented by a 308 shaft-mounted Dynacorp brake. The belted pulleys for the system permitted speed ratios ranging from 1.42 to 0.63. The pneumatic and powder gun arrangements, the Beckman-Whitley high-speed camera, and initial and final velocity measuring devices are detailed elsewhere (Wu and Goldsmith, 1990a; Yuan et al, B1992). A photograph and a schematic of the arrangement are shown in Figs. C-1 and C-2.

c) Procedure

When a low-strength plate is tested at the highest rotational motor speed of 5000 rpm, two mirrors were also used to deviate the light path from the flash unit to provide the proper distance from the camera from the required field of view. However, this was also done to minimize the danger of impact of debris from the target on the camera lens or other sensitive instrumentation.

Target emplacement is followed by insertion of striker and shell containing measured powder charge in gun. The high-speed camera is stabilized at the desired framing rate. All personnel are evacuated from the test chamber prior to firing. This occurs by depressing a button exterior to the site after the camera shutter has been manually opened. Once the button is pushed, the sequence of events is activated automatically. This includes the propulsion of the striker, the initial velocity measurement, the triggering, after a suitable delay, of the flash activated by passage of the projectile through the second laser beam. Immediately subsequent to firing, the shutter is closed, and the motor shuts off automatically 0.5 s after firing at which point the brake is activated.

d) Experimental Investigation and Failure Phenomena of Various Targets

Initial tests were conducted on cardboard targets to ascertain the appro-

priate synchronization and setting of the experimental controls. Subsequently, three materials were examined extensively: 6061-T6 aluminum, CR1010 steel and polycarbonate (Lexan), with thicknesses ranging from 1.588 mm (1/16 in) to 9.525 mm (3/8 in). The linear velocities of the plate at the impact radius of 254 mm (10 in) were chosen as 53.3, 93.1 and 133.3 m/s, corresponding to rotational speeds of the driven shaft of 2000, 3500 and 5000 rpm, respectively. The two types of cylindrical 12.7 mm ($\frac{1}{2}$ in) diameter, 38.1 mm (1.5 in) long hard-steel (R_C 60) projectiles consisted either of blunt-faced or 60° conicaly-tipped configurations. Initial striker velocities ranged from 200 to 1000 m/s. The measurements included the initial and final projectile velocities, the striker trajectories, crack (or crater) lengths in the target, and the penetration and failure modes of the plate as observed by the high-speed camera. Table C-1 lists the experimental conditions and some of the results.

(d-1) Deformation and Failure of 6061-T6 Aluminum Targets

(i) Results for Blunt-nosed Projectile Impact

For this test condition, a plug of nearly the same size as the cross section of the projectile is always initially ejected. A small rotation of the projectile occurs as the result of plate motion. Stress concentrations initiate at the side opposite to the direction of motion of the plate, and cracks first appear in this region, also resulting in a non-cylindrical lateral plug surface. In addition, some petals are formed that initiate at a point of material weakness or location of stress concentration. However, this is a secondary phenomenon when both target and projectile speeds are relatively large and target failure during plugging occurs primarily in shear. Subsequent to the plugging phase, the tip of the projectile is no longer in contact with the target. Additional plate failure ensues primarily due to contact with the side of the striker which results in a sizable bearing stress, acting opposite

to the direction of target motion, that is considerably greater than the material strength. For various impact conditions, three typical failure phenomena were observed in the petaling process:

(I) A regular continuous pile-up with some small cracks at its edge are formed around the crater, as shown in Fig. C-3. Here, a thin plate moving at high speed is penetrated by a high-velocity missile.

(II) A pile-up consisting of three major petals separated by two major cracks may be generated, as shown in Fig. C-4. The shape of the mound is not as regular as that observed in (I), and some small cracks are found in each petal. Two major cracks are propagated by combinations of Mode I and Mode III fracture. Due to the relative motion between striker and plate, target material is pushed not only to each side, but part of the petal is bent in a direction opposite to the motion of the target. This occurs when the target attains an intermediate thickness and the initial projectile velocity is not too high (i.e. a $\frac{1}{4}$ in thick 6061-T6 Al plate moving at 133 m/s struck by a blunt projectile at an initial speed of 450 m/s.).

(III) A major petal with a width approximately the same as the striker diameter is formed, as shown in Fig. C-5. The petal usually exhibits a large curvature due to bending. The propagation of the two cracks is primarily due to tearing (Mode II fracture) so that the material pile in the sides of the hole is not observed. This feature is observed when the plate is thin (1/16 in) and both target and projectile have relatively low speeds of 53.3 m/s and 143 m/s, respectively.

Due to the complexity of the process, failure phenomena intermediate to those described above are also observed in some of the tests. The petaling noted in (III) is similar to previously observed "front petaling" (Wu and Goldsmith, 1990a, 1990b) whereas the side petaling observed there has not been

found in the present investigation.

(ii) Results from Impact with Conical Projectiles

Due to the different contact geometry, the failure phenomenon here is different from that found in (i). One or more segments, most of triangular shape, are always generated, although the duration of this phase is not as well defined as in the case of blunt-nosed strikers. The size of the plug increases with plate thickness for the same projectile speed. In view of the conical tip, the contact area continuously increases that, in addition to the target motion, extends the petaling process. The length of the crater under comparable conditions is less than that for a blunt striker, and the petal appearance is more pronounced. Due to cracks initiated during the plugging stage, the piling up of the material around the crater is not as regular as that observed in the case of blunt strikers, and several cracks are found in this mound, as shown in Fig. C-6.

(d-2) Deformation and Failure of CR 1010 Steel Targets

The dynamic response of 3.175 mm (1/8 in) thick CR 1010 steel plates have been investigated both for blunt and conical-nosed strikers. When the initial velocities are higher than the ballistic limit, the response is similar to that of the 6061-T6 aluminum targets. However, due to differences in the material behavior, the deflection of the plate produced during plugging is larger than that generated in an aluminum plate of the same thickness.

(I) Blunt Projectiles

In the present tests, cracks are arrested in the petals and a mound of material around the contact area caused by bearing forces is present after perforation, as illustrated by Fig. C-7. For the same impact conditions, the plastic deflection region during plugging is even larger than that produced in a 1/16 in thick aluminum plate. Additional failure produced in the petaling

stage, such as indicated in (I) in the previous section for 1/16 in. plates was also found here. However, the dynamic response of the striker in the process is like that produced in a thicker aluminum plate. The decrease in the impact direction and rotation angle of the projectile is larger than what occurred in an aluminum plate of the same thickness. When the initial velocity is low, one or two cracks may extend to the end of the mound concomitant with a failure type intermediate to (i) and (ii) described in the last section.

(II) Conical Projectiles

Upon contact with a conical tip, the target material near the contact point is first stretched. Cracks initiate and petals are pushed out. Due to the high ductility of CR 1010 steel, plugging is not observed in the tests so that such a stage is hard to define. The failure of the plate in this phase is mainly due to tensile stress rather than shear. With the striker moving forward, cracks are generated in the plate and petals are bent due to the increase in the diameter of the contact circle. The plate deflection in this phase is greater than that produced by the impact of a blunt projectile, and also greater than on a corresponding aluminum plate struck by a conically-headed missile. Additional failure due to the contact between side surfaces of the striker and target is similar to that observed in impact on the aluminum plates. By virtue of the large deformation of the petals produced in the plugging phase and the high strength of the steel, the failure of the plate in the petaling stage is a combination of bending of the petals, Mode I fracture due to the large circumferential stress, and Mode III fracture due to compression and tearing, as portrayed in Fig. C-8.

(e) Failure Phenomena in Polycarbonate Plates

In the perforation of this material, plugging occurs first by brittle

fracture due to shear, in view of the material response in this fashion at room temperature. Additional failure mechanisms result from contact between the target and the side of the projectile. High local temperatures due to friction reduce the tensile strength of the target, and a fluid layer is produced at the interface. Consequently, some of the sections detached from the disk tend to adhere and move with the striker, while others are dissociated and assume an independent trajectory. The penetration time is short because the polycarbonate strength is low compared to the other materials used in the present tests, but, except for a clearly discernible front petaling process, the integral portion of the target tends to return to its initial position after penetration. The width of the crater is smaller than the diameter of the projectile due to elastic recovery and inward thermo-plastic flow; this phenomenon has also been observed with stationary plates of this material struck by cylindro-conical projectile (Radin and Goldsmith, 1988).

The photographs presented in Figs. C-9 and C-10 indicate that both blunt and conically-tipped projectile produce front petaling. The crater length caused by the impact of a blunt projectile is slightly greater than that from its cylindro-conical counterpart. The residual deformation indicates that the material experiences plastic flow during penetration.

(f) Interpretation of Failure Phenomena

A qualitative explanation of the failure process in the metal plates requires the specification of two parameters: Γ , which denotes the rate of propagation of petaling in the target, and Φ , which represents the rate of the contact area movement relative to the target. Parameter Γ varies inversely with the strength (and/or) thickness of the plate and is directly proportional to the striker momentum, mv , so that substantially smaller petals are generated at low values of this parameter. Furthermore, Γ depends on the tip

shape; it is greater for a conical- than for a blunt-nosed striker. The variation of contact area movement Φ increases with both projectile and target speed and decreases with material strength and/or target thickness.

(1) If $\Gamma \gg \Phi$, failure, consequently, occurs primarily by petal propagation. Tests involving low impact and small target speeds fall into this category; this case is exemplified by Fig. C-5.

(2) If $\Gamma > \Phi$, initial plugging is followed by petaling with substantial permanent deformation. This occurs for the cylindro-conical striker where front edge petal propagation exceeds the rate of contact area movement relative to the target. The stress near the petal edge does not immediately exceed the ultimate strength of the target, so that a plastic region near the crater edge is formed.

(3) When $\Gamma = \Phi$, both brittle and petaling failure occur around the edge of the crater. The impact produces little, if any plastic deformation in the disk.

(4) If $\Gamma < \Phi$, failure occurs primarily in a brittle fracture mode. Petaling has virtually no influence on the failure phenomenon.

(5) If $\Gamma \ll \Phi$, failure is dominated by bearing stress, exemplified by Figs. C-3 and C-7 where the target is embrittled by the high loading rate. Petaling can not propagate very far as the plug is rapidly separated from the plate by brittle fracture. The disk area near the contact zone will be compressed toward the end of the crater opposite to the direction of motion of the target. The final configuration of the petal usually involves a continuous piling up of the material around the crater.

(g) Motion of the Projectile during and after the Impact Process

Figure C-11 portrays a typical penetration process recorded by a high-

speed camera. Due to the motion of the target, there is a time-dependent moment acting on the projectile that changes both speed and orientation of the striker. Table C-1 contains the initial and final values of these parameters. The projectile kinematics are not significantly affected by the penetration process at high impact velocities for relatively moderate transverse target speeds and strengths, but the force exerted by the target will introduce some tumbling of the striker after completion of the perforation.

(g-1) Final Striker Velocity

The ratio of final to initial projectile velocity in the direction normal to the target surface is proportional to its initial value and inversely proportional to the target thickness, material strength and transverse speed. The influence of the first three parameters on the projectile speed is easily understood, since all of them relate to the ability of the target to resist perforation. When a target has a higher transverse speed, a greater rotation of the striker is produced due to the application of a higher moment. Consequently, the contact region between striker and target increases and a greater resistive force is produced. Thus, the projectile will manifest a lower final velocity compared to the case of slower target motion. It is observed that, when the initial striker velocity is about 900 m/s, the projectile experiences only a minor change in the velocity normal to the target subsequent to perforation, since the rotation of the striker generated by the petaling process is small; thus, there is a relatively low resistance of the target to the forward motion of the projectile.

(g-2) Trajectory of the Striker

The experimental results show that the trajectory angles θ for the same plate struck by different projectiles are of the same order of magnitude. The final trajectory angle is proportional to the plate thickness and inversely

proportional to the initial projectile speed. An increase in plate thickness increases the time of interaction between projectile and plate. The striker usually experiences a higher value of θ for impact on thicker plates. The increase of material strength has the same effect on the striker trajectory as an increase in plate thickness. Here, resistance of the plate to striker perforation increases, and hence the contact duration is enlarged as well.

The direction of motion of the target is normal to the initial striker trajectory. The failure of the target, and the influence on the motion of the projectile should be symmetric to the direction of target motion. However, since the target plate is usually somewhat anisotropic, caused by the sheet rolling process, and, further, an unstable rotation of the projectile may occur due to the asymmetric air pressure on its frontal face, a small deviation of the projectile in the plane of the target normal to its direction of motion occurs in some cases. The angle of deviation is also listed in Table C-1 and is so small that it can be neglected in most cases.

For polycarbonate plates, the resistance due to an increase in target thickness does not change as much as for metallic plates for the present impact conditions. Thus, the projectile trajectory exhibits virtually no change for the current test sequences.

(h) Analytical Modeling of Impact on Metallic Moving Structures

A analytical model which assumes that the perforation process consists of two successive stages -- plugging and petaling -- is formulated. Throughout the analysis, the striker is considered to be a rigid, flat-ended cylinder of radius a and the target material of density p is taken to be rigid-perfectly plastic. In the xyz coordinate system, z is normal to the plate and w is the displacement in that direction. Three consecutive phases are involved in the plugging process: plastic wave propagation, common motion of

the plate and striker, and failure of the plate by formation of a plug. In the petaling stage an energy approach was adopted. Energy is dissipated in numerous ways; account has been taken of that due to tearing the petal, a piling up of plastically-deformed material around the hole, bending and momentum of the petal. Projectile motion during and after perforation is calculated using rigid-body dynamics. Many of the details were presented in previous annual and semi-annual reports.

Some improvements have been made in the present analysis compared to previous models of plate impact in both the plugging and petaling stages (Beynet and Plunkett, 1971; Wu and Goldsmith, 1990a, 1990b).

(h-1) Plugging Stage

(h-1.1) Plastic Wave Propagation

This phase of the event is the same as detailed by Beynet and Plunkett and Wu and Goldsmith (1990a, 1990b); the velocity is given by $c_p = \sqrt{K/\rho}$ where K is bulk modulus of the material.

(h-1.2) Common Motion Stage of Plugging: Plate Theory

(i) Basic Assumptions and Equations of Motion

The model of Beynet and Plunkett assumes the presence of an outer stress-free region (not reached by any wave) and an immediately adjacent annular region subjected only to compressive elastic waves; no deflection occurs in either of these zones. Strictly speaking, the description of the target should be accomplished using shallow shell theory, since the target assumes such a configuration after the plastic wave has arrived at the distal side. However, since the duration of the plugging stage is very short, it is assumed that the disk still retains its planar shape and plate theory can be used. The motion in the interior regions beyond the contact zone, a plastic deformation region and a region of elastic in-plane and shear deformation.

respectively, can be found in Reismann (1988) and Whitney (1987).

The following assumptions are made in the present analytical model:

(I) The problem is considered to be axisymmetric since the duration of this phase is very short (less than 10 μ s).

(ii) Elastic deformation may be neglected in accordance with the previous cited investigations.

(III) Shear effects in the contact region are large and must be included.

(IV) The radial and circumferential bending moments M_r and M_θ and the radial displacement u_r are taken as zero. This has been shown to be a good model both theoretically and experimentally by Beynet and Plunkett (1971).

(h-1.3) Strain-Displacement Relations

It is assumed that the stress in the normal direction is finite, but the rotation ϕ is infinitesimal and $u_r = 0$. The strain and rotations are given by

$$\epsilon_{rr} = (1/2)(\delta w/\delta r)^2 \quad \epsilon_{rz} = (1/2)(\delta w/\delta r) \quad \phi_0 = \sin \phi_0 = (\delta w/\delta r)$$

(h-1.3) Constitutive Equations

For simplicity, a limited interaction criterion (Jones, 1967) is used so that there are no interactions between radial and circumferential membrane forces N_r and N_θ and the moments; only shear is considered together with the moments. It can be shown that only the positive horizontal portion of the yield hexagon is active, so that $N_r = h_t \sigma_r = h_t S_y$ and $0 \leq N_\theta \leq h_t S_y$ where S_y is the yield stress of the material.

(h-1.4) Governing Equations and Boundary Conditions

With the assumption that the derivatives $(\delta^4 w/\delta t^2 \delta r^2)$ and $(\delta^4 w/\delta r^2 \delta t^2)$ are continuous for all r and t , the field equation for the common motion is

$$\nabla^2 w + (h_t^2/12)(p/S_y) \nabla(\delta^2 w/\delta t^2) = (p/S_y)(\delta^2 w/\delta t^2)$$

where ∇^2 is the Laplacian operator in polar coordinates.

The motion of the striker is decelerated by both the resultant shear

force Q_r and the in-plane force N_r . When elastic deformation is neglected, the plate deflection outside the plastic deformation region is zero. Thus, the boundary conditions for the present problem are

$$(m_s + m_p)(\delta^2 w / \delta t^2) = 2\pi a [I_\theta (\delta^3 w / \delta t^2 \delta r) + N_r (\delta w / \delta r)] \quad \text{at } r = a \quad \text{and}$$

$$w = 0 \quad \text{at } r = R_a$$

The value of R_a can be found from the distance that the plastic wave propagates at time t . It is given by

$$R_a = a + c_p t = a + [\sqrt{(K/p)}]t / [1 + (h t^2 / 12)(2\pi / \lambda)^2]$$

where c is the wave speed, $c_p = \sqrt{(S_y/p)}$ is the plastic wave speed in the elementary theory and λ is the wave length.

The initial conditions are determined by the response of the plate at the time when the plastic wave reaches the distal surface of the target at time t_1 . They are given by

$$w|_{t=t_1} = 0 \quad \text{for } r > a; \quad \delta w / \delta t|_{t=t_1} = \begin{cases} (m_s / [m_s + m_p])v_0 & \text{for } r = a \\ 0 & \text{for } r > a \end{cases}$$

where m_p is the mass of the plug, m_s is the mass of the striker, and v_0 is the initial projectile velocity. The above equation of motion and corresponding initial and boundary conditions are solved up to the point of the failure of the material.

(h-2) Failure of the Target

Unlike other formulations where failure is considered to be the result of a single mechanism, such as shear or tension, failure for the present model is regarded to be governed by the effective strain in order to incorporate both types of loads. Thus, failure will occur when the effective strain $\epsilon_e > \epsilon_u$, where ϵ_u is the ultimate strain. The failure criterion for the present case can be expressed by: $\epsilon_e = (\sqrt{2/3})[2\epsilon_{rr}^2 + \frac{3}{2}(2\epsilon_{rz})^2] = \epsilon_u$.

During the plugging process, the force decelerating the projectile con-

sists of a shear force Q_r and an in-plane membrane force and is given by

$$F = 2\pi a(Q_r + N_r \frac{\delta w}{\delta r}) = 2\pi a(Q_r + N_r \sin \phi_0) \quad \mathbf{A}$$

Due to the lateral motion of the target, the projectile will also acquire an angular velocity $\dot{\alpha}$ and a rotation angle α at the end of plugging. However, as stated earlier, the rotation is so small that these angular parameters are considered to be zero, and the computed motion at the end of plugging constitutes the initial conditions for petaling.

(h-3) Energy Approach to Petaling

Damage subsequent to plugging results from the contact of the lateral surface of the striker with the target and results in petaling, an asymmetric process. An exact continuum analysis requiring determination of the stress field is extremely complex and well beyond the current state of the art. However, some results based on phenomenological observations can provide reasonable quantitative estimates of the damage to the target at this stage. An energy approach is used to estimate plate failure in this mode and rigid-body dynamics is used to describe the striker motion. The basic relation is

$$d(\Sigma W_i + K_e) = F \cdot dx \quad \text{or} \quad \Sigma \dot{W}_i + \dot{K}_e = F \cdot v_p$$

Here $\Sigma \dot{W}_i$ is the total energy rate of plate deformation due to projectile contact, \dot{K}_e is the kinetic energy rate of the petal, F is the contact force, and v_p is the velocity of the contact point. The coordinate system describing the motion and the geometry of the plate is shown in Fig. C-12. The motion of the target produces a moment acting on and resulting in a rotation of the projectile.» The energy rates corresponding to the piling up of the material around»the contact edge due to the acting compressive force, bending of a petal and fracture are estimated in the sequel, and are given as a function of

the rate of crater length increase, \dot{x} .

(h-3.1) Plastic Deformation Energy \dot{W}_1 due to the applied Plastic Force

During the petaling process, the motion of the projectile and failure (including both deformation and fracture) of the plate are symmetric about the x-axis. Assume that the projectile has an angle α relative to the x-direction at time t_i . The shape of the contact line between the projectile and the plate is a semi-ellipse. The minor axis of the ellipse is approximately equal to the radius of the projectile a , and the major axis is $b = (a/\cos \alpha)$. During the brief interval t_i to t_{i+1} , the change of the crater length is dx , and the plate material in this region is removed from the plate and eventually piled up around the edge of the hole. If it is assumed that this material has yielded completely and has the shape shown in Fig. C-13, and using G.I. Taylor's similarity law (1948) and results from symmetric hole enlargement (Thomson, 1955), the energy rate during this process can be shown to be

$$\dot{W}_1 = 2ah_t S_y \ln ([2A dx + B]/L_0) \dot{x}$$

where L_0 is the length of the curve in Fig. C-13 and A and B are constants for the short time duration Δt .

(h-3.2) Energy Rate due to Petal Bending

The further failure of the mound of material is due to the bending of the petal and the propagation of two parallel cracks separated by a distance approximately equal to the diameter of the projectile. Considering the petal to be a cantilever beam as shown in Fig. C-14, and neglecting the elastic strain energy, the energy rate for bending of a perfectly plastic petal is given by

$$\dot{W}_2 = ah_t S_y \epsilon_t \dot{x}$$

where ϵ_t is the ultimate tensile strain of the material.

(h-3.3) The Energy Rate \dot{W}_3 due to Crack Propagation

The major fractures in the plate producing the petal are two nearly par-

allel cracks. The propagation of these cracks in most cases is probably caused by a combination of bending and by the circumferential stress in the petal. The application of such a combined damage model may, however, lead to mathematical difficulties. It will be assumed here that the two mechanisms are not coupled and that the crack energy release rate can be estimated separately.

(I) Non-negligible Tearing Energy Rate

To quantify the crack propagation process, the work of fracture to be computed consists not only of the work required to produce Mode III shear fracture, but also that necessary to create the thin lip of width d on the edge of the petal, as shown in Fig. C-14c. For a perfectly plastic material, the energy rate of tearing is $W_3|_{\text{tear}} = (4dh_t S_y \tau_0 / \sqrt{3}) \dot{x} + (S_y / \sqrt{3})(h_t)^2 \dot{x}$ B where d is the shear zone width and τ_0 is the shear strength.

(II) The Energy Release Rate for a Mode I Crack

For the thin plates used in the present tests, the fracture is believed to be either in a plane stress or a plane stress/plane strain transition mode. Since both the velocities of the striker and the target are relatively high, an elastic-plastic or fully plastic behavior must be considered so that linear elastic fracture mechanics is not applicable to the present problem. A general method developed to define the fracture conditions in a component experiencing both elastic and plastic deformation is the Rice J integral which is a line integral with failure (crack initiation) occurring when J reaches some critical value. The analytic solution of J for the present problem can not be obtained. An empirical relation found for the crack opening displacement δ (Giavanola and Finnie, 1984) as $J = m S_f \delta$, where $S_f = (1/2)(S_y + S_u)$ is the flow stress, S_u being the ultimate strength of the material, and m is a numerical parameter given as 1.2 for plane stress and 1.6 for plane strain.

For a thin sheet, the crack opening displacement has to be accommodated by plastic deformation over a length approximately equal to the thickness (Finnie, personal communication). Hence $\epsilon = \delta/h_t$. If a critical value of the average strain ϵ_u is accepted as a fracture criterion, then the critical value of J in a Mode I crack is: $J_{IC} = mS_f\epsilon_u h_t$. By taking $G = J$ (Hertzberg, 1983), the energy release rate required for an incremental dx for two cracks is then $\dot{W}_3|_{\text{Mode I}} = m\epsilon_u(S_y + S_u)h_t^2x$ C

Equations B and C give the energy rates required to propagate the crack by virtue of two different mechanisms. Generally, the crack propagation is controlled by a complex combination of these processes. If it is assumed that there is no interaction, then the total fracture energy rate is

$$\dot{W}_3|_{\text{tearing}} + \dot{W}_3|_{\text{Mode I}}$$

(J) Major Improvements in Present Analytical Model

Several advancements were made in the analytical formulations presented by Wu and Goldsmith (1990a, 1990b) and Beynet and Plunkett (1971).

(J-1) Plugging State

(I) Transverse shear is included in the governing equations; this changes the wave pattern from a non-dispersive plastic longitudinal wave travelling with velocity $c_p = \sqrt{S_y/\rho}$ to a dispersive wave combining presence of in-plane extensive action and shearing effects. The phase velocity of this wave is $c/c_p = [1 + (\frac{2\pi h_t}{\lambda})^2]^{-1/2}$ where λ is the wave length. From the strain-deflection equations, it is evident that $\epsilon_{rr} = \phi_0\epsilon_{rz}$; thus, ϵ_{rz} is much greater than ϵ_{rr} . When thickness to wave length ratio is significant, it is evident that the propagation speed is substantially lower than c_p , representing the effect of shear; when h_t is small, compression dominates and

the outward propagation is essentially non-dispersive. If the shear effect is neglected, the equation of motion is the same as that of previous investigation. However, such a neglect leads to an underestimation of the deflection of the plate, especially that near the contact zone.

(II) Transverse Shear included in the Total Force Resisting Perforation

The total resistant force is given by A for the present model with h_t and S_y specified for a given target. Hence, if the resultant shear force Q_r is neglected, the resistive force will depend only on the gradient of the angular deflection $\delta w/\delta r$, assumed to be small. Thus, E is underestimated noticeably by the neglect of shearing effects.

(III) The effective strain is used as the failure criterion for the target.

Both experimental and analytical results show that, at high projectile velocities or for targets of intermediate thickness, the failure of the material in the plugging stage is primarily due to transverse shear (Zukas, 1990). The failure criterion for the present model, given above, is an equivalent strain. By substituting the strain-deflection relation into this criterion, it is seen that the failure of the material is mainly determined by shear rather than extension. Thus, the use of a criterion incorporating the shear effect is validated.

(J-2) Differences of Present Model from Previous One

As before (Wu and Goldsmith, 1990a, 1990b), an energy approach is used to describe the crater hole enlargement in the petaling stage. However, some of the techniques employed differ from those employed in the earlier model.

(J-2.1) Effect of Speed of Target on Petaling

It may be observed from the results presented by Wu and Goldsmith (1990a, 1990b) that the petaling process does not depend on the speed of target motion; all the differences due to this effect are generated during plugging.

With the assumption that the contact point is always in the mid-plane of the target, the effects of target motion are incorporated in the present model.

(J-2.2) Estimate of Plastic Deformation Energy Rate due to Compression

In the previous model, the plastic strain in the circumferential direction in the mound around the crater was given by $\epsilon = \int_{R_0}^R (dR/R)$ where R is defined as the radius of the elliptic tip. This expression is valid only for the case of homogeneous and axisymmetric deformation. When the major and minor axes of the ellipse are close in value, the approximation provides a simple expression of the circumferential strain, given by

present formulation is determined by $\epsilon = \int_{L_0}^L (dL/L)$ which is the general definition of strain. Also, as was found in the earlier investigation, that approach is applied to side petaling only. It was extended to front petaling by simply doubling its value, without further investigation or explanation. It was observed that most of the petals formed are of the frontal variety in the present investigation. Consequently, the earlier result does not appear to be applicable to the present case.

(J-2.3) Fracture Energy Rate

When a plate is struck by a projectile, there is a relatively large area of plastic deformation around the crack. The fracture condition for the target thicknesses in the present work, as stated, is believed to be either plane stress or a plane-stress/plane strain transition region. It is usually impossible to use linear elastic fracture mechanics to calculate the energy release rate when large scale yielding occurs. Thus, the energy release rate due to Mode III fracture is estimated using the plastic tearing concept in the present model. Both the tearing energy and the strain energy due to shear in the tearing process are included. This differs from the earlier investigation

where large scale yielding effects were considered by justifying the size of the plastic zone together with some results from linear fracture mechanics.

Secondly, the previous model employed a stress intensity factor given by $K_C = K_{IC} [1 + (1.4/h_t^2)(K_{IC}/S_y)^4]$ to calculate the energy rate due to mode I fracture. This empirical equation applies only to a region in plane strain (Hertzberg, 1983) and not for the present case. It can be seen that the K_{IC} value above is inversely proportional to h_t^2 and, hence, the energy rate is inversely proportional to h_t . This is contradicted by the experimental results and general physical concepts. In the present formulation, large scale yield effects are considered and the J integral is introduced in the estimate of the energy release rate due to Mode I fracture.

Both the present resulting fracture energy rates per unit area due to Mode I and Mode III fracture are proportional to the plate thickness h_t . This type of linear relation agrees with experimental results (Knott, 1973).

(K) Results

A finite-difference method is used to solve the two-stage analytical model and the motion of the rigid striker. The program was designed so that the impact phenomena can be predicted for several cases: the evolution of the events and the final values of various parameters for a single shot, and the terminal values of various penetration parameters for several different impact velocities and plate thicknesses. Figs. C-15-C-22 exhibit the x- and z component history, the history of the trajectory and its angle, as well as the rotational angle of the projectiles and the grid line variations for three different aluminum plate thicknesses, a blunt projectile at a initial speed of 450 m/s and a target velocity of 133 m/s.

(L) Numerical Simulations

The program DYNA-3D (Whirley and Hallquist, 1991) was utilized in the

numerical simulation of the present problem to check the accuracy of the analytical computations and to complement the predictions of the model. It is an explicit 3D finite element code useful for solid mechanics; this program and its associated pre- and post-processors, developed at LLNL, have been used frequently in the investigation of impact processes; however, only lately has it been possible to utilize this program for cases involving perforation because of improvements in the handling of slide lines and the capability of separation of fragments from the main body. The computations were performed on a CRAY X-MP/48 Supercomputer located at several Centers, in particular those at San Diego and Pittsburgh. The programs were accessed remotely via Telnet from the Berkeley Campus. The application of the DYNA3D program involves a successive implementation of three independent codes: INGRID (Stillman and Hallquist, 1985), DYNA3D and TAURUS (Spelce and Hallquist, 1991). INGRID is a three-dimensional mesh generator for modeling nonlinear systems and has been developed as the preprocessor of DYNA3D, which provides a complete input file for this program. This program, which features 35 types of material models and 11 types of equation of states, and its execution has been described in great detail in many other publications and will not be detailed further here. The SAND slide surface program which permits material failure, was incorporated in the 3.2.3 version of DYNA3D and used in the present computations.

Two types of material model were applied to the projectile: the first is rigid and the second is kinematic/isotropic elastic-plastic. The rigid version is a DYNA3D defined material type 20 which provides an inexpensive method for modeling portions of a structure that are much stiffer than the regions of interest, or which experience negligible deformations. The material behavior of kinematic/isotropic elastic-plastic (material type 3 of

DYNA3D) is elasto-plastic and includes linear strain hardening. The hardening parameter β_h specifies an arbitrary combination of kinematic and isotropic hardening; $\beta_h = 0$ represents purely kinematic, while $\beta_h = 1$ denotes purely kinematic hardening. The numerical algorithms used in the model are adopted from Krieg and Key(1976); detailed mathematical descriptions can be found in Whirley and Hallquist (1991).

The material model used for the target is elastic-plastic with failure, DYNA3D defined material type 13. Before failure occurs, this model will give exactly the same behavior as material type 3 with $\beta_h = 1.0$. Two failure criteria have been implemented in this model: an effective plastic strain based criterion, and a hydrostatic tension based criterion. However, since the failed elements are stretched and largely deformed rather than removed from the main body, this model is not sufficient to describe the plugging and petaling processes before the SAND slide interface is developed.

SAND is a newly developed capability for modeling material failure along interfaces. A failure criterion is defined for a volume of material adjacent to a SAND contact surface. As material within an element on the contact surface fails, the failed element is removed from the calculation, and the slide surface definition adapts to the new exterior boundary of the unfailed material. This new type of slide surface allows improved modeling of the problems where penetration occurs.

Results of several runs are presented in Figs. C-15 to C-17. In the first example, the projectile is modeled as a rigid body with an initial velocity of 450 m/s. The target is a 1/8 in thick aluminum plate moving at a speed of 133 m/s. In the second example, an elastic/plastic model is used for the striker, all other conditions being the same. The validity of the rigid-body assumption for the striker in the analytical model can be gaged by the

results of this computation. The third example portrays the perforation of the plate by a conically-tipped striker, which is not covered by the present analytical model.

A comparison of the results from the analysis and the numerical computation clearly exhibits a two-stage velocity drop (plugging and petaling) in the numerical evaluation and a three-stage drop (plastic wave propagation, common motion and petaling) for the phenomenological model. The time of penetration obtained from the two types of analyses are very close. The decrease in the value of v_{CZ} from the numerical solution is a little larger than that from the analysis in both plugging and petaling stages.

The results for the striker velocity in the x-direction, v_{CX} are linear functions of the penetration time by both methods; however, the numerical result is somewhat smaller than the analytical counterpart.

It may be noted from Figs. C-15 and C-16 that there is only a small amount of projectile rotation produced in the perforation, as predicted by the analysis using DYNA3D. This was not found in the experiments. The phenomenological model provides a much better description of the orientation.

It may be concluded from this investigation that many of the parameters involved in plate perforation of a moving target by a blunt projectile moving normal to its plane of motion are satisfactorily predicted by either the phenomenological or the numerical model. However, some features are found to be in much better accord when the analytical model is used, while the detailed history of others is more closely described numerically. Clearly, additional tests covering a wider range of materials, thicknesses and initial velocities need to be performed to ascertain whether the present formulations are valid over wider ranges of impact parameters and geometries. However, even at this stage, it is clear that improvements in both should be considered to provide a

somewhat better predictive capability than presently available, although the current approach is substantially superior to that chosen initially.

(M) COMPARISON OF EXPERIMENTAL, ANALYTICAL AND NUMERICAL RESULTS

Figure 26 - 29 present the comparison of the measured information with the predictions of the phenomenological and numerical models for a 3.175 mm (1/8 in) thick 6061-T6 aluminum plate struck by a blunt-nosed bullet at various initial speeds for a fixed target speed of 93.1 m/s. As may be noted, the terminal velocity is in excellent agreement with predictions, the crater length discrepancy increases with increasing striker speed, but is still in fair accord, the numerical prediction of the trajectory angle is not satisfactory, especially at low striker speeds, and the penetration time is in good agreement, considering the uncertainties of the data within the limits of a single time frame.

D. CONCLUSION

The present undertaking was concerned with three disparate aspects of non-standard impact, penetration and perforation of thin plates by projectiles: (A) Impact on Stationary Plates for Blunt-nosed Projectiles with Yaw, (B) Impact of Tumbling Projectiles on Stationary Plates, and (C) Impact of both Blunt-nosed and Conical-nosed Projectiles on Targets moving orthogonal to the initial striker trajectory. All three facets of this work were attacked by both experimental and phenomenological/numerical methods, and correlations between data and analytical predictions were obtained. Considering the fact that these events represent some of the most complex phenomena in the field of impact mechanics, the correlations for all three phases were found to range from acceptable to excellent. Further improvements in the modeling process can and should be undertaken, but the current results constitute a workable

foundation that provides sufficient predictability for results of this type to permit their utilization without costly extensive additional testing.

BIBLIOGRAPHY

Beynet, P., and Plunkett, R., "Plate Impact and Plastic Deformation by Projectiles," Exp. Mech., v. 11, pp. 64-70, 1971.

Giovanola, J. H., and Finnie, I., "The Crack Opening Displacement (COD) of a Fracture Parameter and a Comparative Assessment of the COD and J-Integral Concepts," Solid Mechanics Archives, v. 9, pp. 227-257, 1984.

Hertzberg, R. W., Deformation and Fracture Mechanics of Engineering Materials. 2d ed. New York, J. Wiley, 1983

Jones, N., "Impulsive Loading of a Simply Supported Circular Rigid Plastic Plate," J. appl. Mech., v. 35, pp. 59-65, 1967.

Krieg, R. D., and Key, S. W., "Implementation of a Time Dependent Plasticity Theory into Structural Computer Programs," Constitutive Equations in Viscoplasticity: Computational and Engineering Aspects, v. 20. New York, ASME, pp. 125-137, 1976.

Radin, J., and Goldsmith, W., "Normal Penetration and Perforation of Layered Targets," Int. J. Impact Engng., v. 7, pp. 229-259, 1988.

Reismann, H. Elastic Plates -- Theory and Applications. New York, J. Wiley & Sons, 1988.

Spelce, T., and Hallquist, J. O., An Interactive Post-Processor for the Analysis Codes NIKE3D, DYNA3D, AND TOPAZ3D. Univ. of California, Lawrence Livermore National Laboratory, Report UCRL-MA-105401, 1991.

Stillman, D. W. and Hallquist, J. O., INGRID: A Three-dimensional Mesh Generator for Modeling Nonlinear Systems. Univ. of California, Lawrence Livermore National Laboratory, Report UCID-20506, July, 1985.

Taylor, G. I., "The Formation and Enlargement of a Circular Hole in a Thin Plastic Sheet," Quart. J. Mech. Appl. Math., v. 1, pp. 103-124, 1948.

Thomson, W. T., "An Approximate Theory of Armor Penetration," J. Appl. Phys., v. 26, pp. 80-82, 1955.

Whitney, J. M., Structural Analysis of Laminated Anisotropic Plates. Technomic Publishing Co., Inc., 1987.

Whirley, R. G., and Hallquist, J. O. DYNA3D: A Nonlinear, Explicit, Three-Dimensional Finite Element Code for Solid and Structural Mechanics -- User Manual. Univ. of California, Lawrence Livermore National Laboratory. Report UCRL-MA-107245, May, 1991.

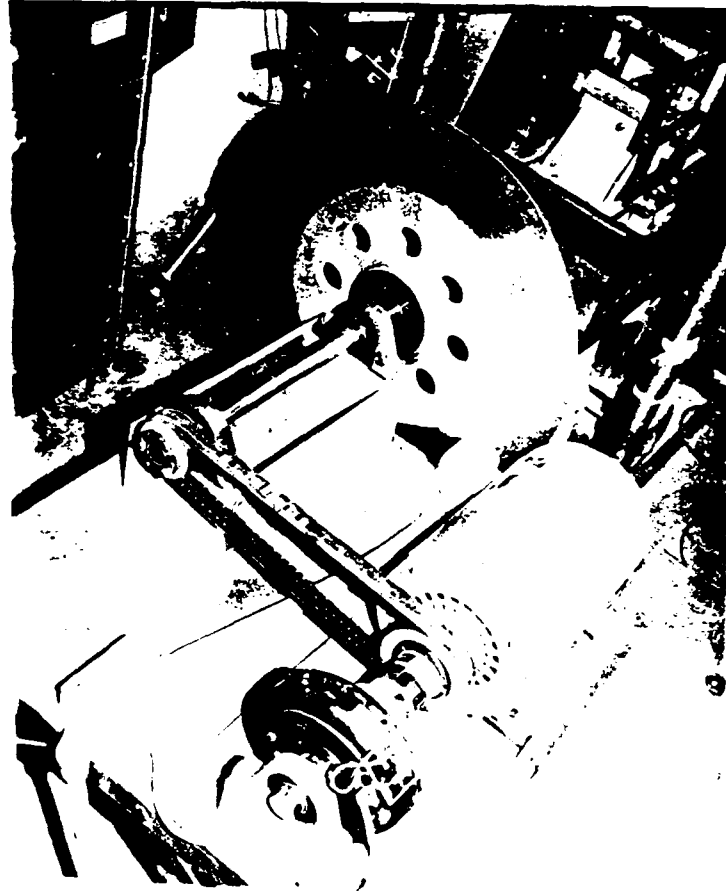
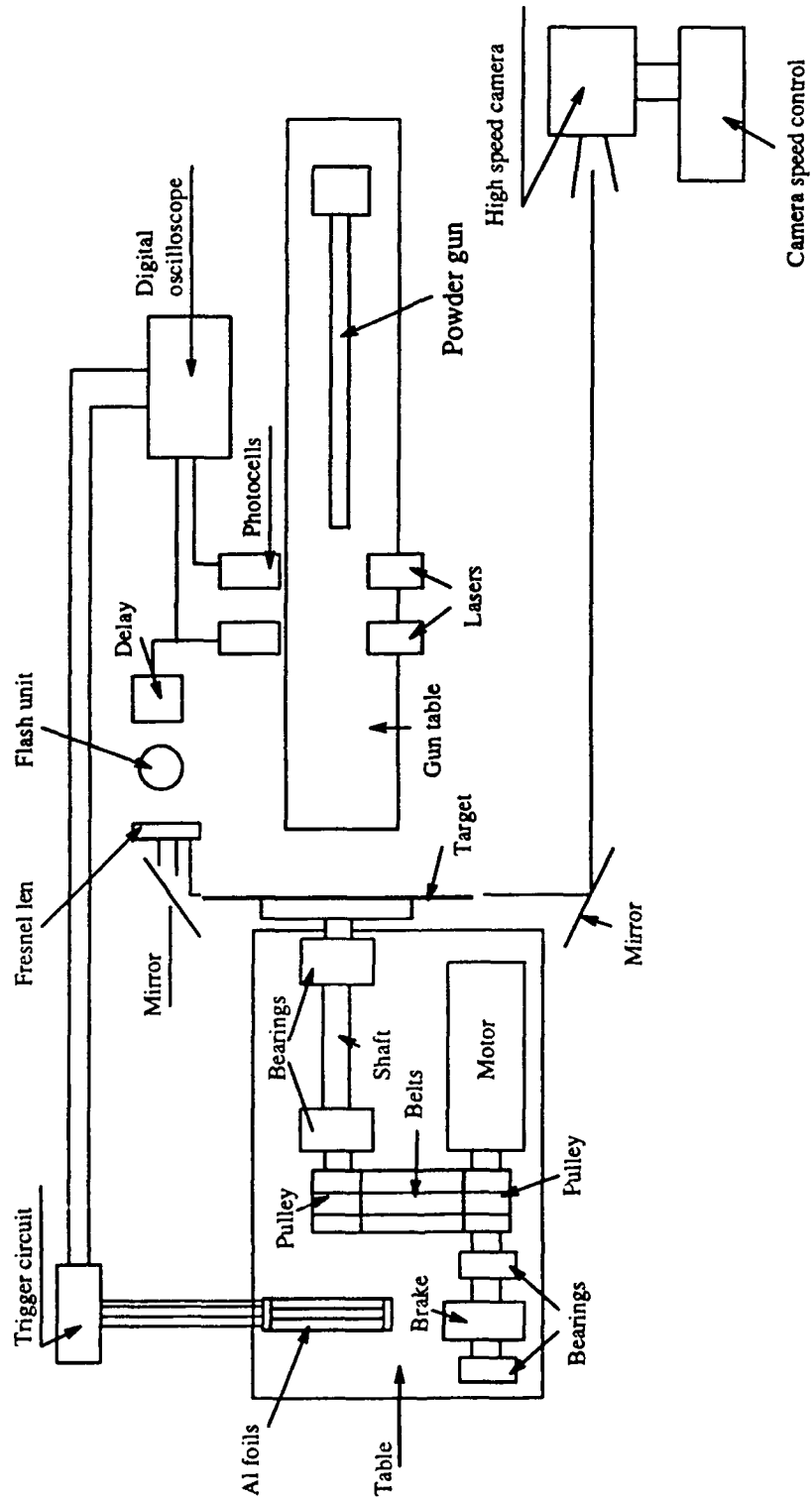


Fig. C-1 Photograph of the target system



Top View

Fig. C-2 Schematic of experimental setup for impact on moving targets

No	Target		Target speed (m/s)	Projectile		Initial velocity (m/s)	Final Velocity (m/s)	Trajectory		Crater Length (cm)
	Material	Plate thickness (in)		Projectile type	weight (gram)			X axis Angle (Degree)	Y axis Angle (Degree)	
1	Al	1/16 in	133 m/s	blunt	39.5 g	443	397	2.19	0.31	2.95
2	Al	1/16 in	133 m/s	conical	32.3 g	448	408	1.56	0	2.1
3	Al	1/8 in	133 m/s	conical	32.2 g	461	423	5.8	0	2.1
4	Al	1/8 in	133 m/s	blunt	39.7 g	426	365	8.39	-0.94	2.4
5	Al	1/8 in	133 m/s	conical	30.7 g	461	413	6.73	0	2.5
6	Poly	1/8 in	133 m/s	conical	30.7 g	405	400	1.88	0.56	2
7	Poly	1/8 in	133 m/s	blunt	39.5 g	434	430	2.19	0.18	2.2
8	Al	1/16 in	133 m/s	blunt	39.5 g	897	no data	0.63	0	2.1
9	Al	1/16 in	133 m/s	blunt	39.5 g	887	no data	0.63	0	2.15
10	Al	1/16 in	133 m/s	blunt	39.5 g	857	no data	0.625	0	2
11	Al	1/16 in	133 m/s	conical	30.7 g	880	875	0.63	0	2.1
12	Poly	1/16 in	133 m/s	conical	30.5 g	890	890	0.03	0	1.6
13	Poly	1/16 in	133 m/s	blunt	39.5 g	880	879	0.02	0	1.8
14	Poly	1/16 in	133 m/s	blunt	39.5 g	422	418	0.62	0.25	2

No	Target		Target speed (m/s)	Projectile		Initial velocity (m/s)	Final Velocity (m/s)	Trajectory		Crater Length (cm)
	Material	Plate thickness (in)		Projectile type	Projectile weight (gram)			X axis Angle (Degree)	Y axis Angle (Degree)	
15	Al	1/8 in	133 m/s	blunt	39.5 g	1025	1016	3.23	0.1	2.5
16	Al	1/8 in	133 m/s	conical	30.7 g	1031	1020	3.15	0	1.8
17	Al	1/4 in	133 m/s	blunt	39.5 g	1005	998	5.13	0.22	2.1
18	Al	1/4 in	133 m/s	conical	30.7 g	1011	1002	4.55	0.2	2.2
19	Poly	1/4 in	133 m/s	conical	30.7 g	454	452	1.9	0	2.3
20	Poly	1/4 in	133 m/s	blunt	39.5 g	456	452	2.3	0	2.35
21	Al	1/4 in	133 m/s	blunt	39.5 g	437	365	18.1	0.025	2.5
22	Al	1/4 in	133 m/s	conical	30.8 g	459	408	21.26	0	2.4
23	Poly	1/4 in	133 m/s	conical	30.7 g	467	466	0.035	0	2
24	Al	3/8 in	133 m/s	blunt	40.1 g	428	342	24.29	0	2.5
25	Al	3/8 in	133 m/s	conical	30.6 g	456	401	23.3	0.2	2.45
26	Steel	1/8 in	133 m/s	blunt	39.5 g	451	332	16.5	2.07	2.4
27	Steel	1/8 in	133 m/s	conical	30.7 g	495	391	9.66	-3.32	2.2
28	AL	1/4 in	133 m/s	blunt	39.5 g	896	881	2.67	0.83	2.1

No	Target		Target speed (m/s)	Projectile type	Projectile		Trajectory			Crater Length (cm)
	Material	Plate thickness (in)			weight (gram)	Initial velocity (m/s)	Final Velocity (m/s)	X axis Angle (Degree)	Y axis Angle (Degree)	
29	Steel	1/8 in	133 m/s	blunt	39.8 g	819	721	3.31	0	3
30	Steel	1/8 in	133 m/s	conical	30.7 g	1016	927	2.9	0	2
31	Al	3/8 in	133 m/s	blunt	39.5 g	866	848	3.56	0.44	2.3
32	Al	3/8 in	133 m/s	conical	30.7 g	870	854	3.1	0	2.5
33	Al	1/8 in	93.1 m/s	Blunt	38.5 g	431	382	8.82	1.32	2
34	Al	1/8 in	93.1 m/s	Conical	29.5 g	457	411	5.45	0.66	2.1
35	Al	1/8 in	93.1 m/s	Conical	29.46 g	894	871	0	-1.32	1.5
36	Al	1/16 in	93.1 m/s	Conical	29.5 g	457	411	1.32	0	2.2
37	Al	1/16 in	93.1 m/s	Conical	29.5 g	992	980	0	0	2.7
38	Al	1/4 in	93.1 m/s	Conical	29.5 g	430		14.81	0	2.5
39	Al	1/4 in	93.1 m/s	Conical	29.5 g	566		12.5	0	2.4
40	Al	1/16 in	93.1 m/s	Blunt	38 g	397	347	1.97	0	2.5
41	Al	1/16 in	93.1 m/s	Blunt	38 g	856.2	811	0.67	0	1.75
42	Al	1/16 in	93.1 m/s	Blunt	38 g	610	569	1.23	0	2.2

Table C-1c. Experimental Results

No	Target		Projectile			Trajectory		Crater Length (cm)		
	Material	Plate thickness (in)	Target speed (m/s)	Projectile type	Projectile weight (gram)	Initial velocity (m/s)	Final Velocity (m/s)		X axis Angle (Degree)	Y axis Angle (Degree)
43	Al	1/16 in	93.1 m/s	Blunt	38 g	254	198	2.76	0	3
44	Al	1/8 in	93.1 m/s	Blunt	38 g	254	189	13.9	0	2.7
45	Al	1/8 in	93.1 m/s	Blunt	38 g	521	478	4.8	-2.63	2
46	Al	1/8 in	93.1 m/s	Blunt	38 g	668	631	1.32	0	1.9
47	Al	1/8 in	93.1 m/s	Blunt	38 g	810	782	1.32	0	1.7
48	Al	1/8 in	93.1 m/s	Blunt	38 g	875.8	848	1	0	1.85
49	Al	1/8 in	93.1 m/s	Conical	29.5 g	599	542	6.56	0	2.2
50	Poly	1/16 in	93.1 m/s	Blunt	38 g	423	415	0.5	0	1.9
51	Poly	1/16 in	93.1 m/s	Conical	29.5 g	467	449	0.5	0	1.9
52	Poly	1/4 in	93.1 m/s	Blunt	38 g	386	372	3.95	1.97	2.5
53	Poly	1/4 in	93.1 m/s	Conical	30.5 g	399	383	5.12	0	2
54	Poly	1/4 in	93.1 m/s	Blunt	38 g	810	800	1.12	0	1.7
55	Poly	1/4 in	93.1 m/s	Blunt	38 g	802	790	5.45	0	1.7
56	Poly	1/4 in	93.1 m/s	Conical	29.5 g	962	951	1.97	0	1.7

No	Target		Projectile			Trajectory			Crater Length (cm)	
	Material	Plate thickness (in)	Target speed (m/s)	Projectile type	Projectile weight (gram)	Initial velocity (m/s)	Final Velocity (m/s)	X axis Angle (Degree)		Y axis Angle (Degree)
57	Steel	1/8 in	93.1 m/s	Blunt	38 g	284	153	23.3	7.85	3
58	Steel	1/8 in	93.1 m/s	Blunt	38 g	420	301	16.3	-4.93	2.1
59	Steel	1/8 in	93.1 m/s	Blunt	38 g	521	419	9.78	-4.93	2
60	Steel	1/8 in	93.1 m/s	Blunt	38 g	686	593	4.93	2.63	2
61	Steel	1/8 in	93.1 m/s	Blunt	38 g	793.8	700	1.98	0	1.9
62	Steel	1/8 in	93.1 m/s	Blunt	38 g	866	771	1.2	0	1.8
63	Steel	1/8 in	93.1 m/s	Conical	29.5 g	444	312	10.8	-3.95	2
64	Steel	1/8 in	93.1 m/s	Conical	29.5 g	1020	918	2.97	0	
65	Steel	1/8 in	93.1 m/s	Conical	29.5 g	948	827	3.19	0.66	1.8
66	Al	1/4 in	93.1 m/s	Blunt	39.5 g	388.8	342	24.3	2.24	2.4
67	Al	1/4 in	93.1 m/s	Blunt	39.5 g	846.7	820	2.92	0.5	1.85
68	Al	1/4 in	93.1 m/s	Conical	29.5 g	426.2	380	16.8	0	1.65
69	Al	1/4 in	93.1 m/s	Conical	29.5 g	774	739	4.1	0	1.7
70	Poly	1/8 in	93.1 m/s	Blunt	39.5 g	397	374	1.4	0	2

No	Target		Projectile			Trajectory		Crater Length (cm)		
	Material	Plate thickness (in)	Target speed (m/s)	Projectile type	Projectile weight (gram)	Initial velocity (m/s)	Final Velocity (m/s)		X axis Angle (Degree)	Y axis Angle (Degree)
71	Poly	1/8 in	93.1	Blunt	39.5 g	876	870	0.2	0	1.62
72	Poly	1/8 in	93.1	Conical	30.5 g	896	893	0.1	0	1.6
73	Poly	1/8 in	93.1	Conical	30.5 g	412	402	1.2	0	1.9
74	Al	3/8 in	93.1	Conical	30.5 g	917	893	3.5	0.3	2.5
75	Al	3/8 in	93.1	Blunt	39.5 g	897	844	3.2	0	2.3
76	Al	3/8 in	93.1	Blunt	39.5 g	588	503	8.9	1.5	2.5
77	Al	3/8 in	93.1	Conical	29.5 g	624	540	8	1.6	2.45
78	Al	1/16 in	51	Spherical	30.0 g	146	121	8.9	0	2.8
79	Al	1/16 in	51	Spherical	30.0 g	143	120	8.8	0	2.6
80	Al	1/32 in	51	Conical	30.5 g	141	122	7.4	0	2.4
81	Al	1/32 in	51	Spherical	29.6 g	135.7	126	8.9	0	2.8
82	Al	1/16 in	51	Spherical	30.0 g	150	128	7.2	0	2.7
83	Al	1/32 in	51	Conical	30.5 g	145.3	119	7.1	0	2.3
84	Al	1/32 in	51	Conical	30.5 g	137.3	113	7	0	2.2

No	Target		Target speed (m/s)	Projectile type	Projectile weight (gram)	Initial velocity (m/s)	Trajectory		Crater Length (cm)
	Material	Plate thickness (in)					X axis Angle (Degree)	Y axis Angle (Degree)	
85	Al	1/32 in	51	Spherical	30.0 g	136.1	7.4	0	2.4
86	Al	1/16 in	51	Spherical	30.0 g	148	7.9	0	2.4

Table C-1g. Experimental Results



Fig. C-3 Mode (a) failure -- A continuous pile-up with some small cracks at its edge
6061 T-6 Aluminum, 1/8 in. thick. $v_0 > 900$ m/s



Fig. C-4 Mode (b) Failure -- A pile-up consisting of three major petals



Fig. C-5 Mode (c) failure -- A major petal produced by bending and tearing



Fig. C-6 Failure phenomenon of a Al plate impacted by a conical striker

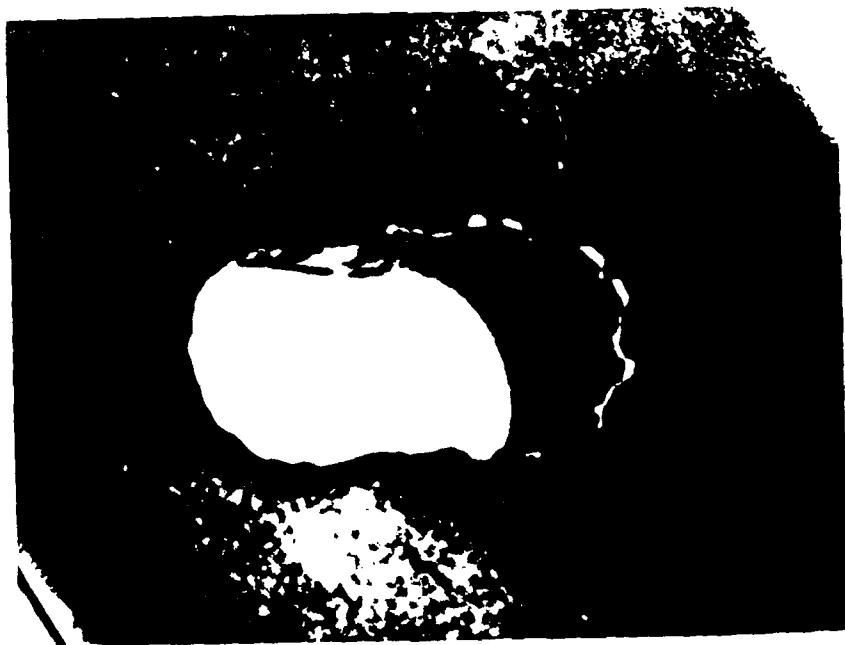


Fig. C-7 Failure phenomenon of steel plate impacted by a blunt striker



Fig. C-8 Failure phenomenon of steel plate impacted by a conical striker



(a)



(b)

Fig. C-9 Plugging and front petaling failure of polycarbonate plate. (Run 6: impact of a conical projectile at a velocity of 405 m/s on a 1/8 in thick polycarbonate plate)
(a). view from impact side ; (b). view from distal side



(a)



(b)

Fig. C-10 Plugging and front petaling failure of polycarbonate plate. (Run 7: impact of a blunt projectile at a velocity of 430 m/s on a 1/8 in thick polycarbonate plate) (a). view from impact side ; (b). view from distal side

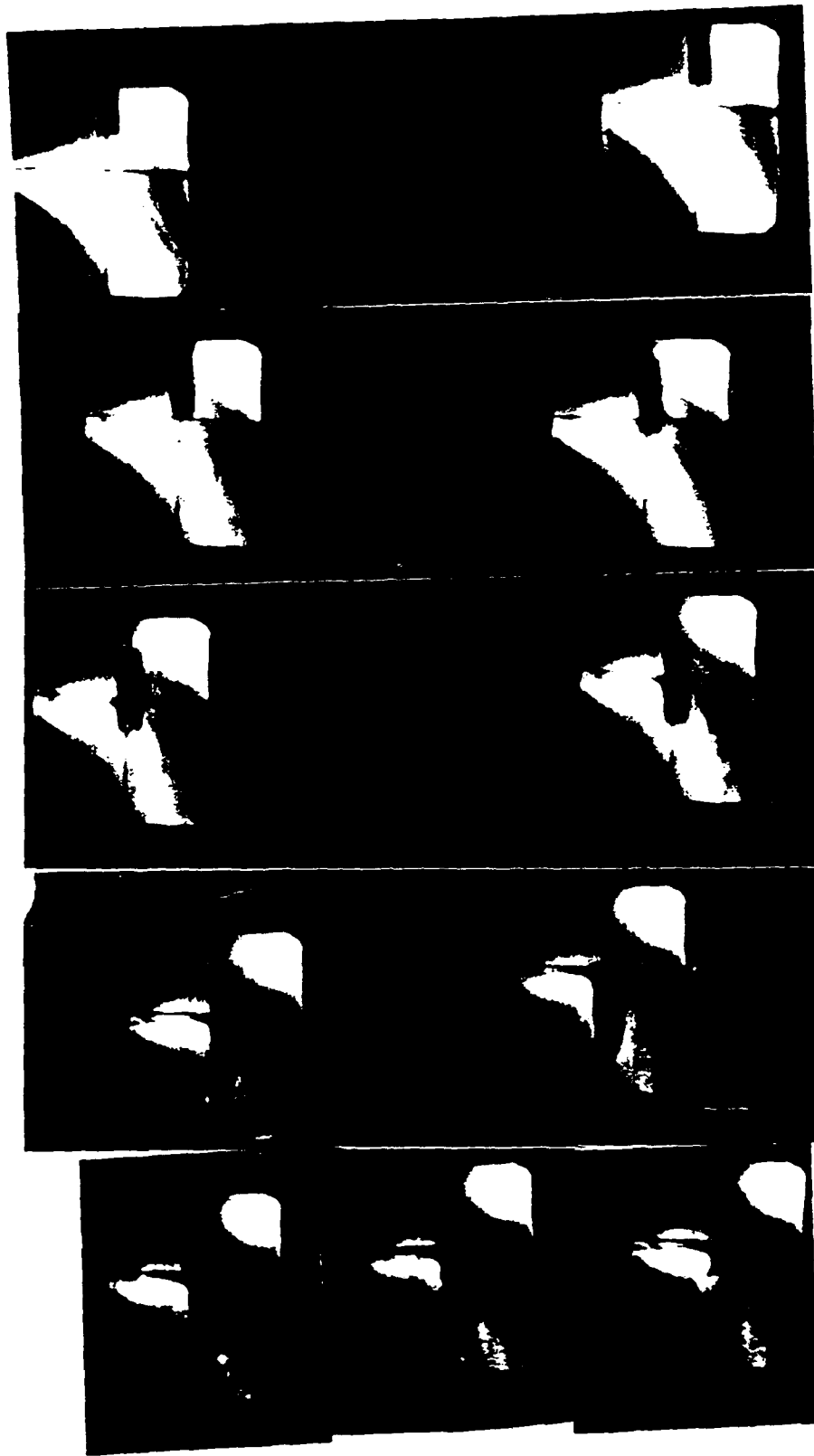


Fig. C-11

Penetration process recorded by high speed camera on run 1.
The framing rate is 54747 frame/sec.

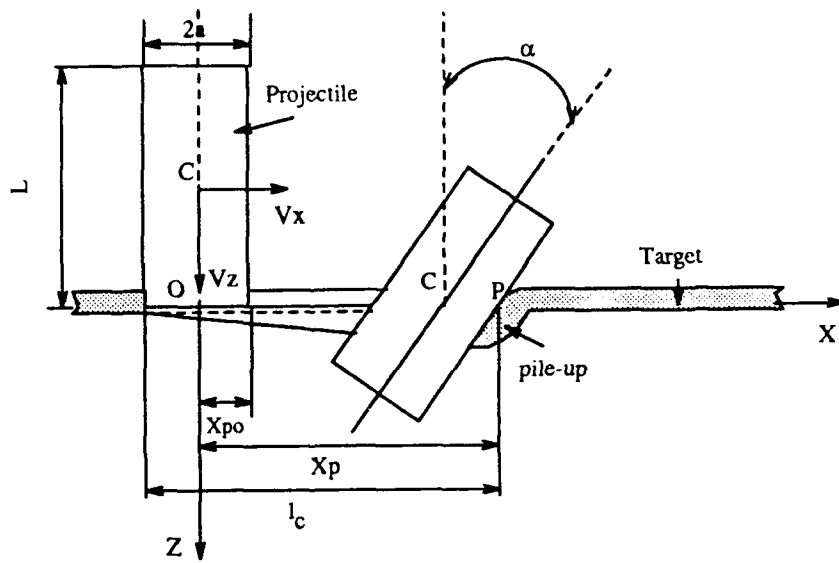


Fig. C-12 Coordinate system in the petaling stage

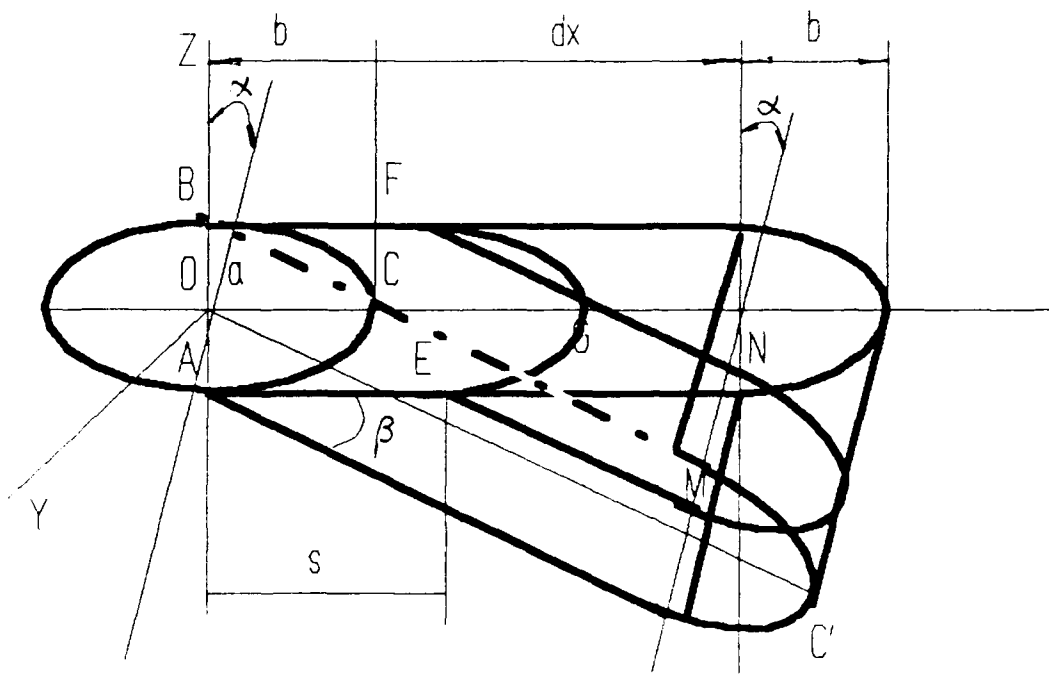


Fig. C-13 Assumed shape of plastic deformation due to compression

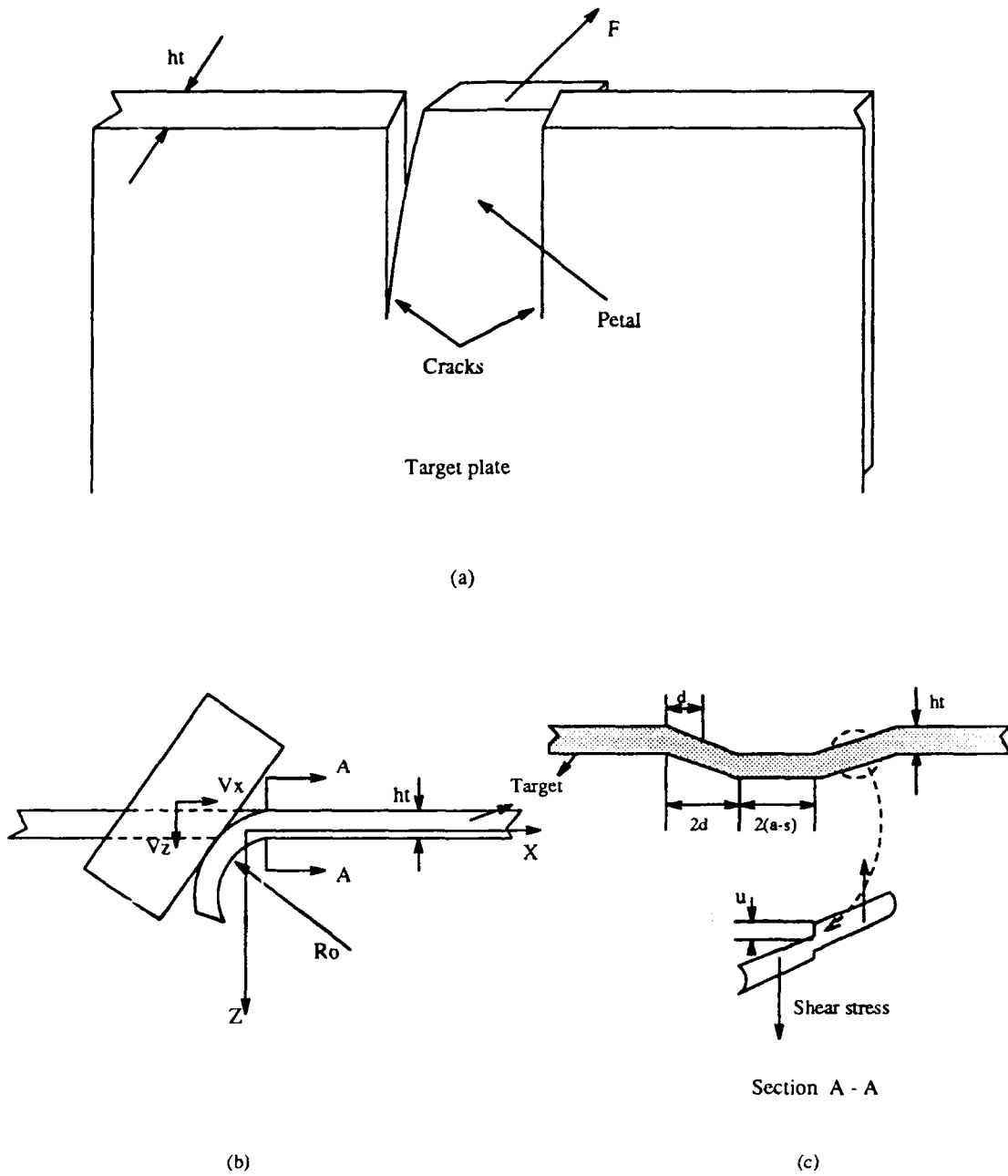
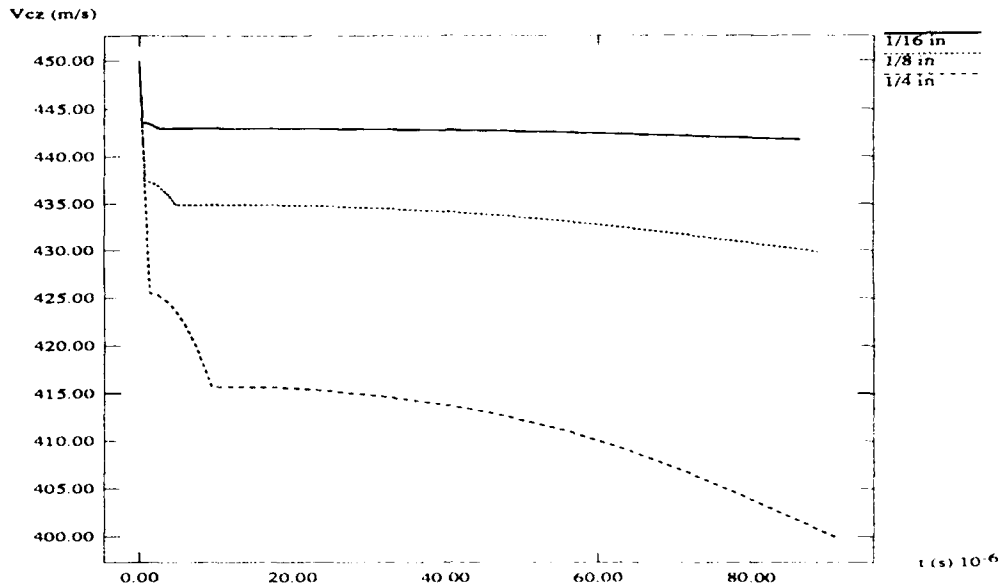
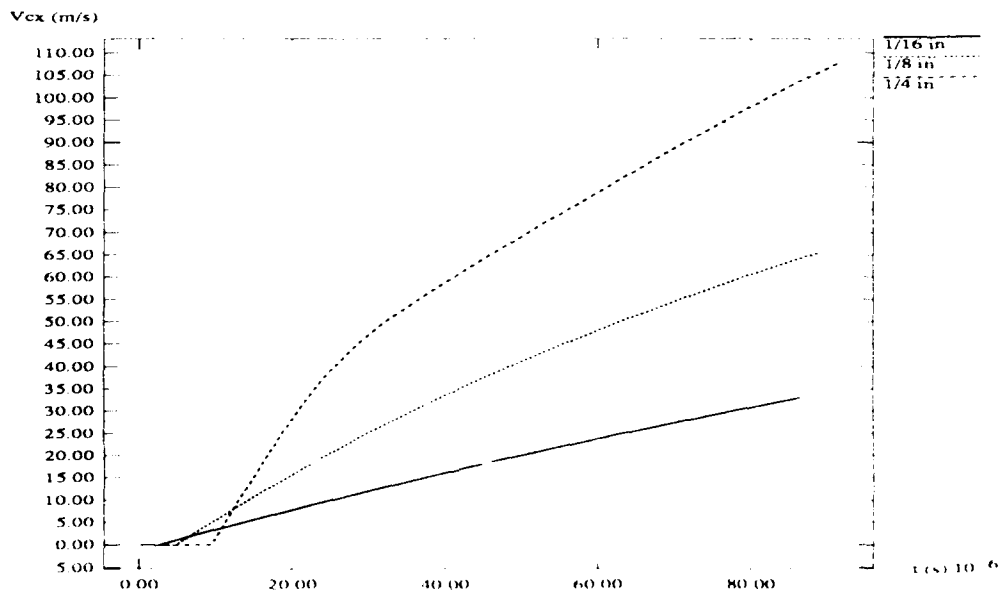


Fig. C-14 Crack propagation due to the tearing and bending of the petal
 (a) Tearing model, (b) bending of the petal
 (c) Shearing of the petal and shear zone structure



**Fig. C-15 Velocity history of the striker in z-direction
1/16, 1/8 and 1/4 in thick Al plates moving at speeds of 133.3 m/s
penetrated by a blunt projectile with an initial velocity of 450 m/s**



**Fig. C-16 Velocity history of the striker in x-direction
1/16, 1/8 and 1/4 in thick Al plates moving at speeds of 133.3 m/s
penetrated by a blunt projectile with an initial velocity of 450 m/s**

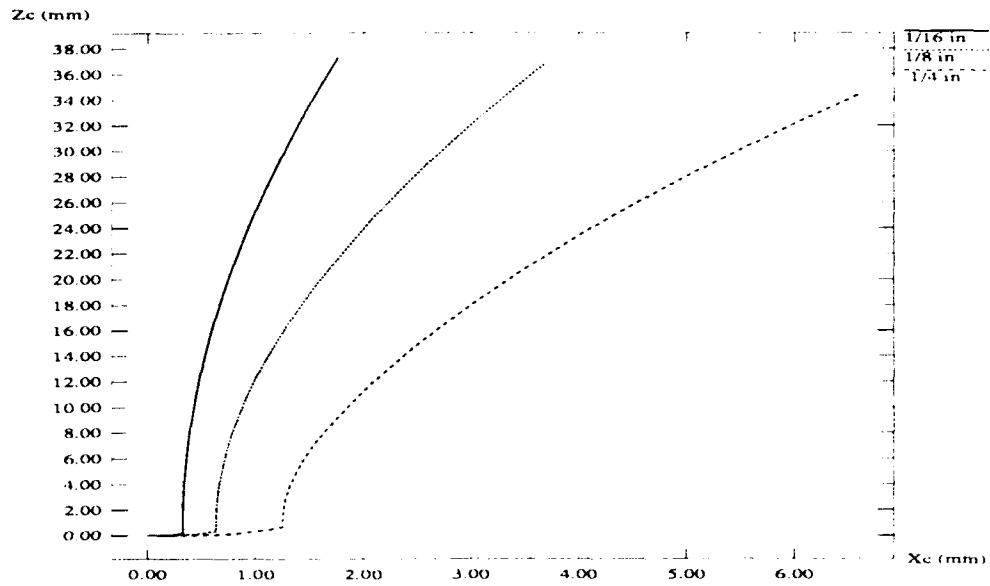


Fig. C-17 Trajectory of the mass center of the striker 1/16, 1/8 and 1/4 in thick Al plates moving at speeds of 133.3 m/s penetrated by a blunt projectile with an initial velocity of 450 m/s

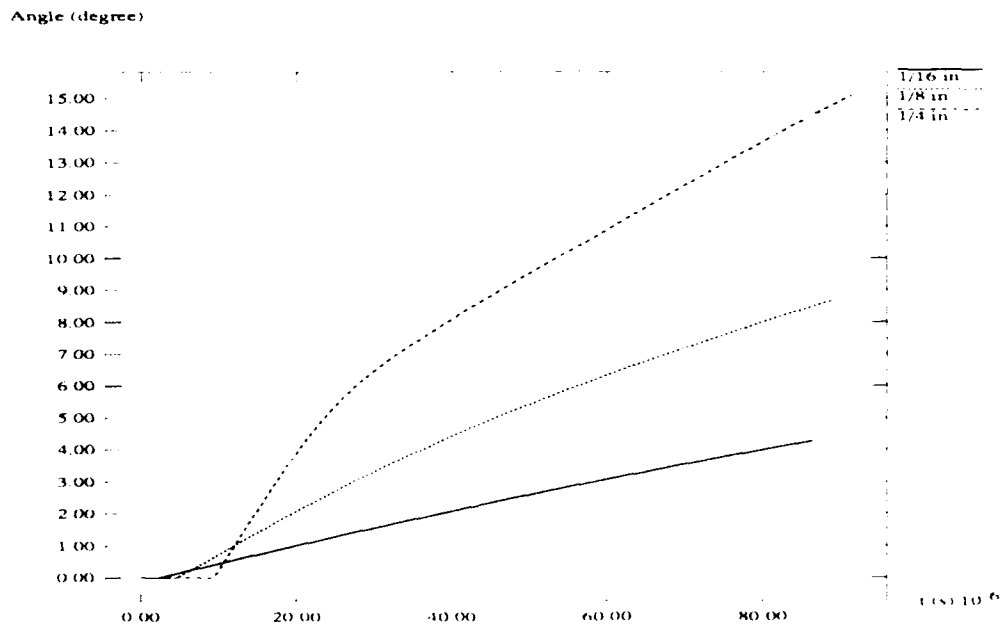


Fig. C-18 Trajectory angle of the projectile 1/16, 1/8 and 1/4 in thick Al plates moving at speeds of 133.3 m/s penetrated by a blunt projectile with an initial velocity of 450 m/s

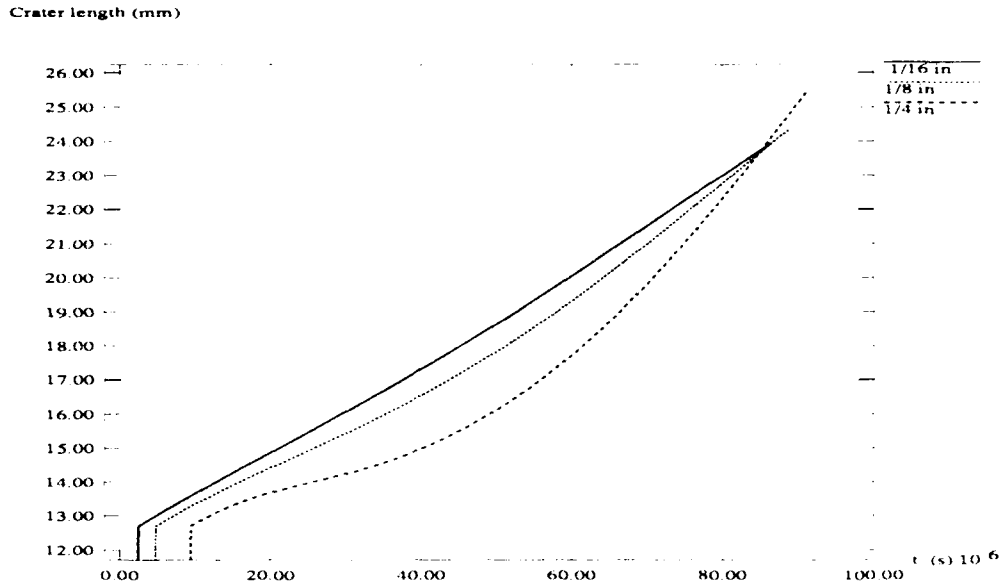


Fig. C-19 Crater lengths of the targets
1/16, 1/8 and 1/4 in thick Al plates moving at speeds of 133.3 m/s
penetrated by a blunt projectile with an initial velocity of 450 m/s

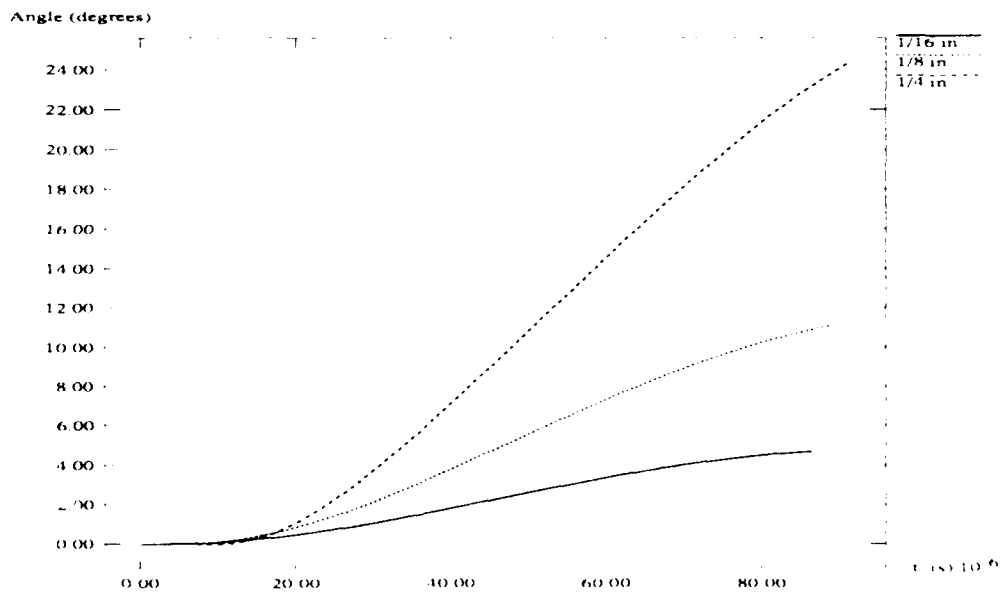


Fig. C-20 Rotational angle of the projectile
1/16, 1/8 and 1/4 in thick Al plates moving at speeds of 133.3 m/s
penetrated by a blunt projectile with an initial velocity of 450 m/s

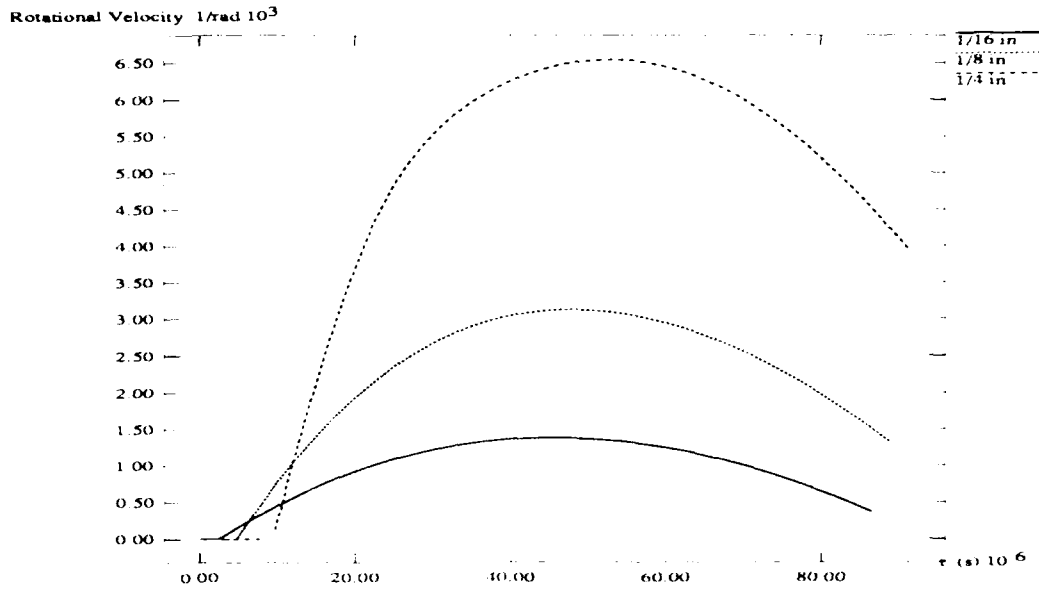


Fig. C-21 Rotational velocity of the projectile 1/16, 1/8 and 1/4 in thick Al plates moving at speeds of 133.3 m/s penetrated by a blunt projectile with an initial velocity of 450 m/s

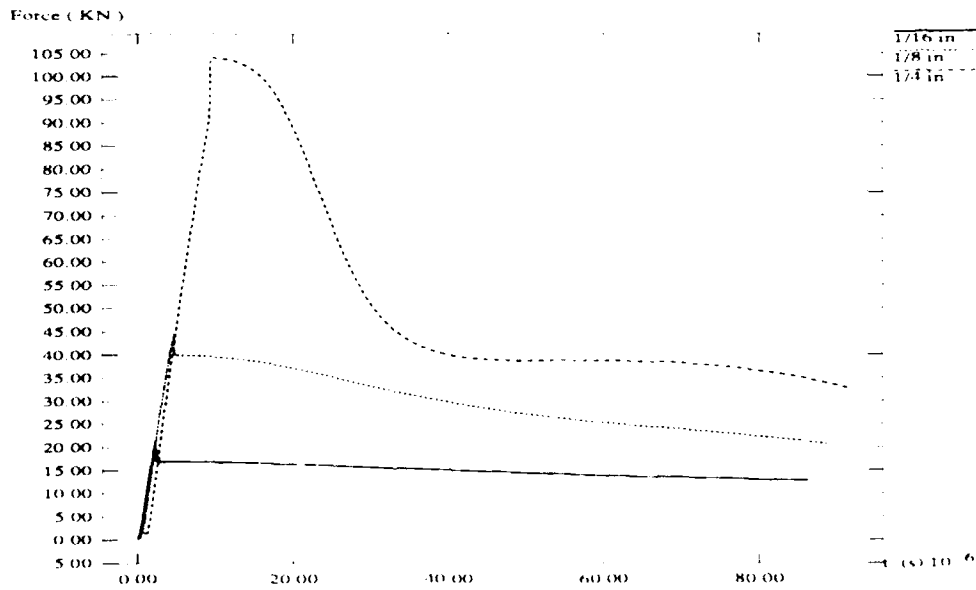


Fig. C-22 Total resistance force applied on the projectile 1/16, 1/8 and 1/4 in thick Al plates moving at speeds of 133.3 m/s penetrated by a blunt projectile with an initial velocity of 450 m/s

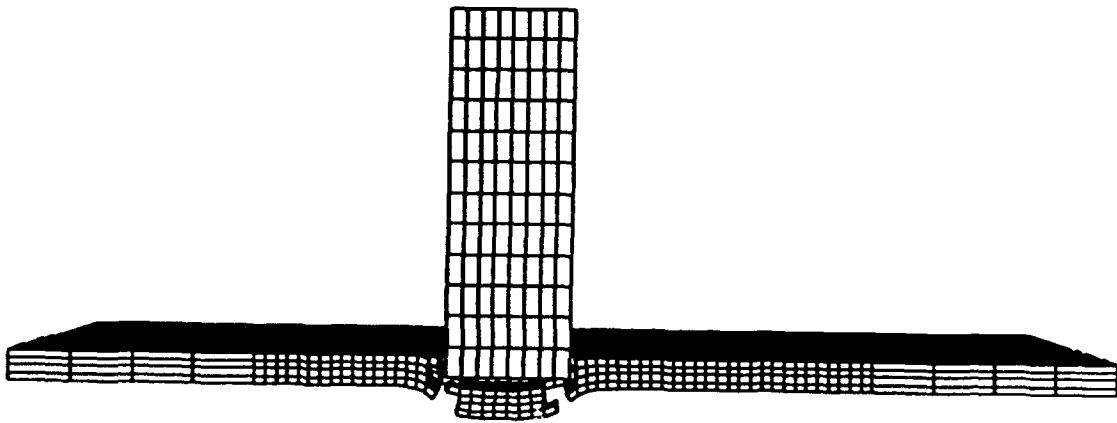
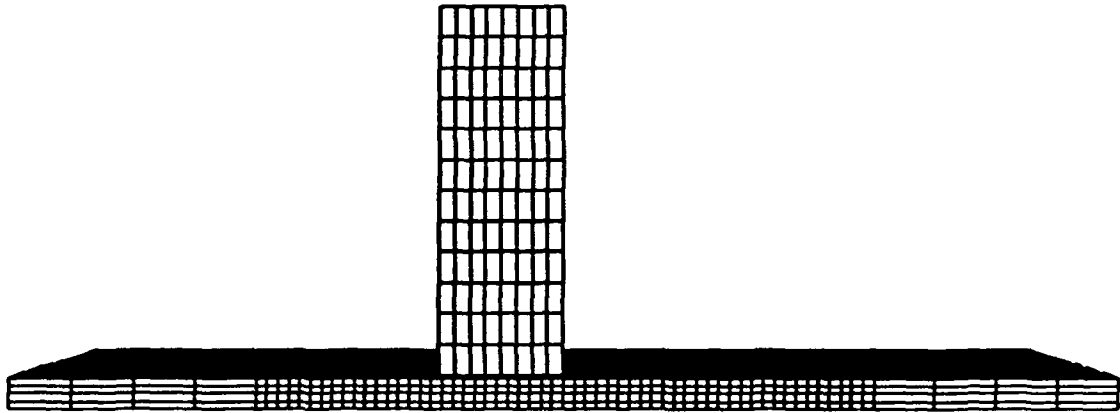


Plate target ($V_i = 450$ m/s, $V_t = 133.3$ m/s)
time = $0.59281E-05$

Fig. C-23a A rigid blunt striker impacts on a 1/8 in thick aluminum plate

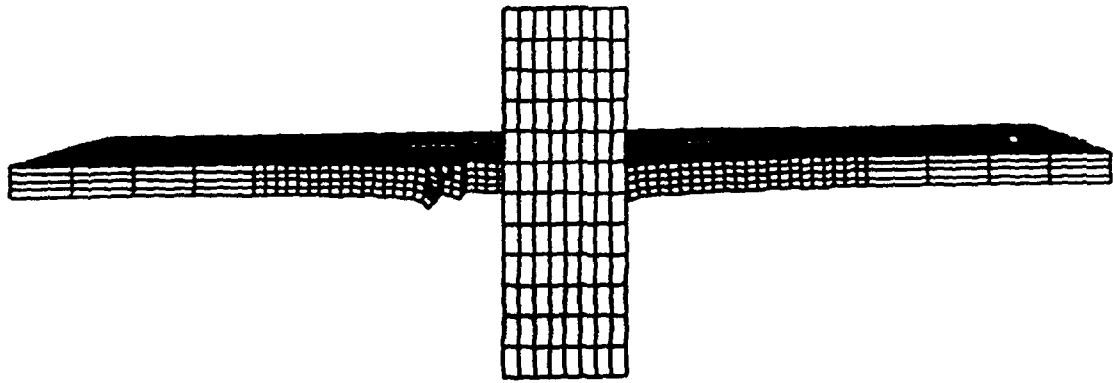


Plate target($V_i=450$ m/s, $V_t=133.3$ m/s)
time = $0.53950E-04$

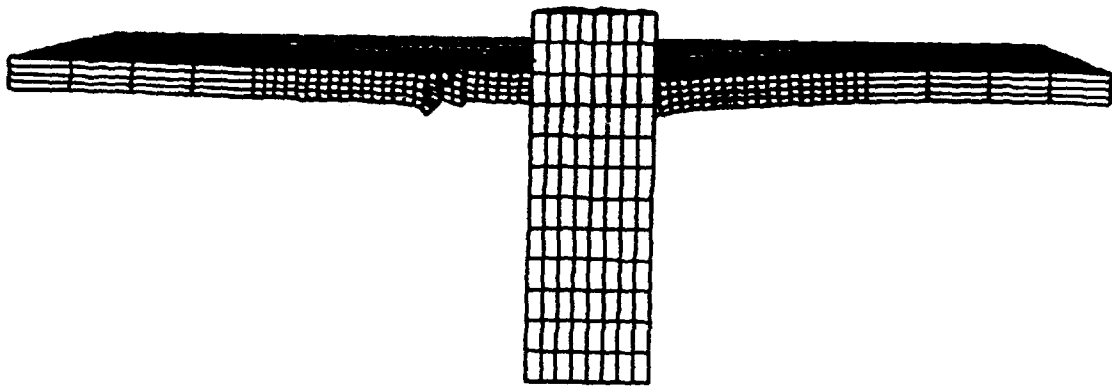


Plate target($V_i=450$ m/s, $V_t=133.3$ m/s)
time = $0.77987E-04$

Fig. C-23b A rigid blunt striker impacts on a 1/8 in thick aluminum plate

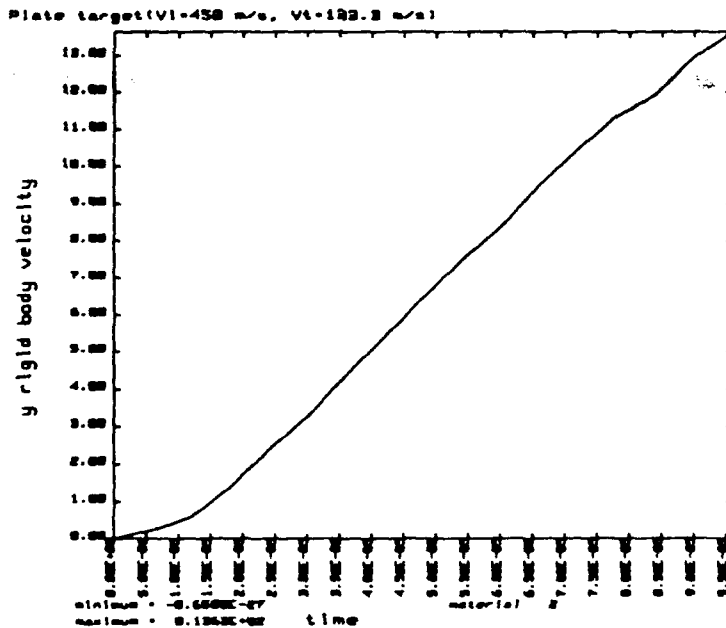
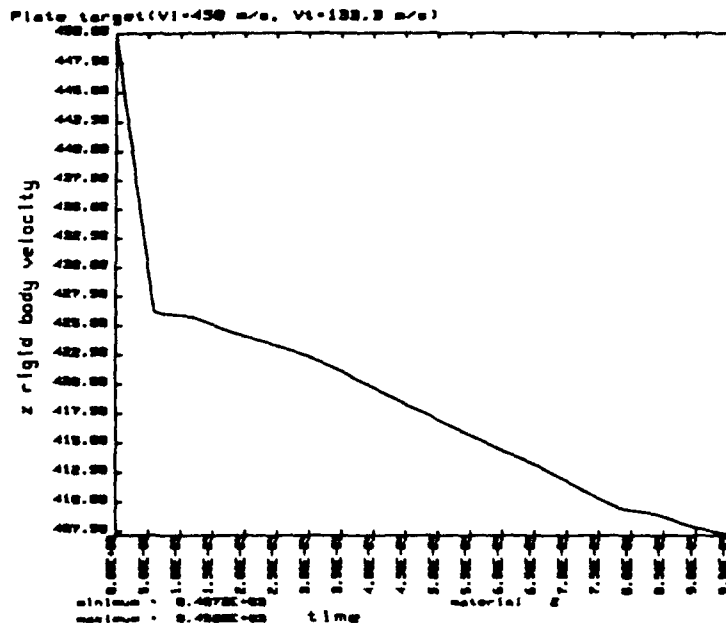
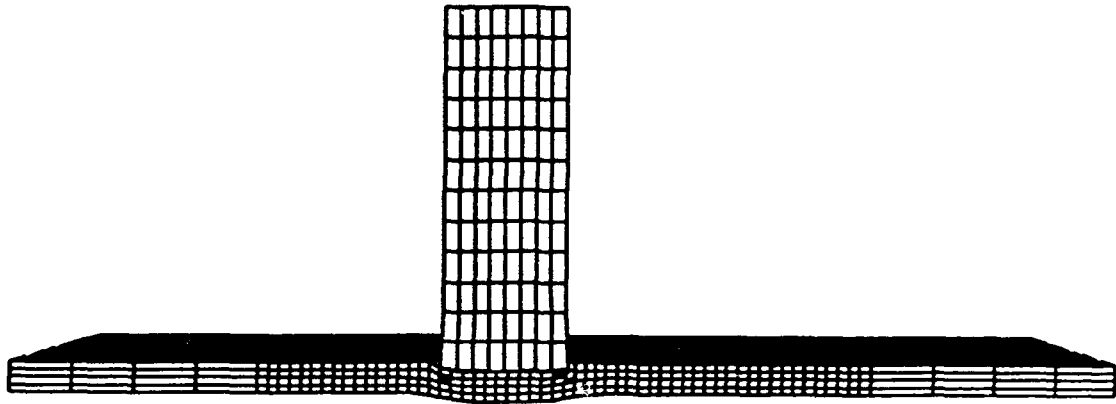
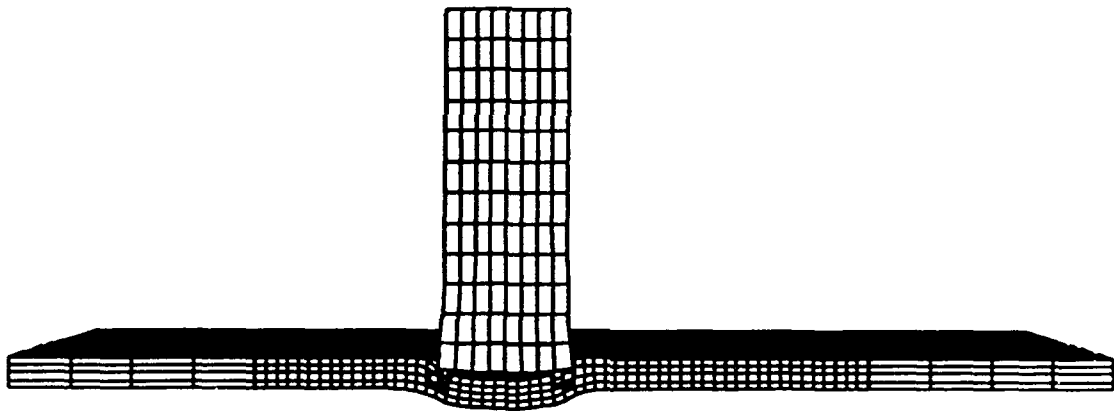


Fig. C-23c Rigid body velocity components for case shown in Fig. C-23a and 23b

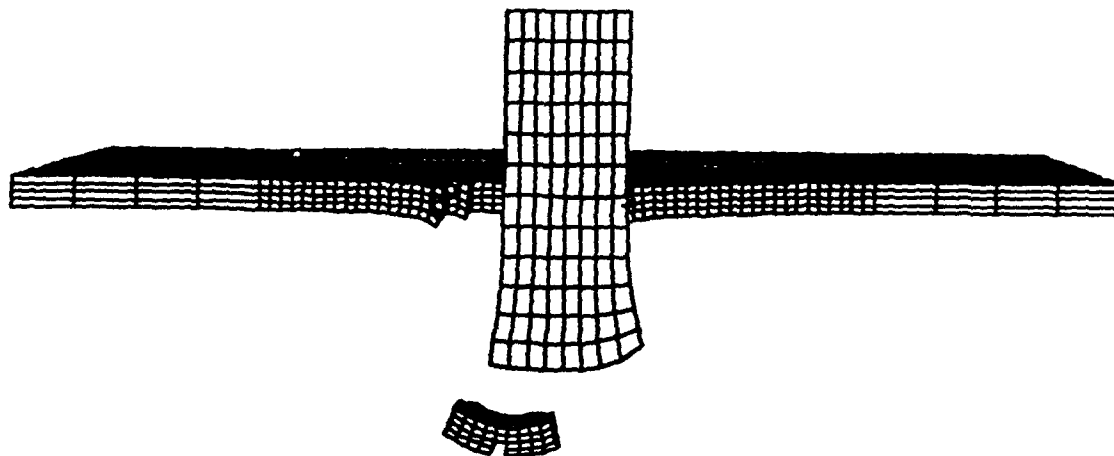


Al Plate ($V_i=450$ m/s, $V_t=133.3$ m/s)
time = $0.29561E-05$

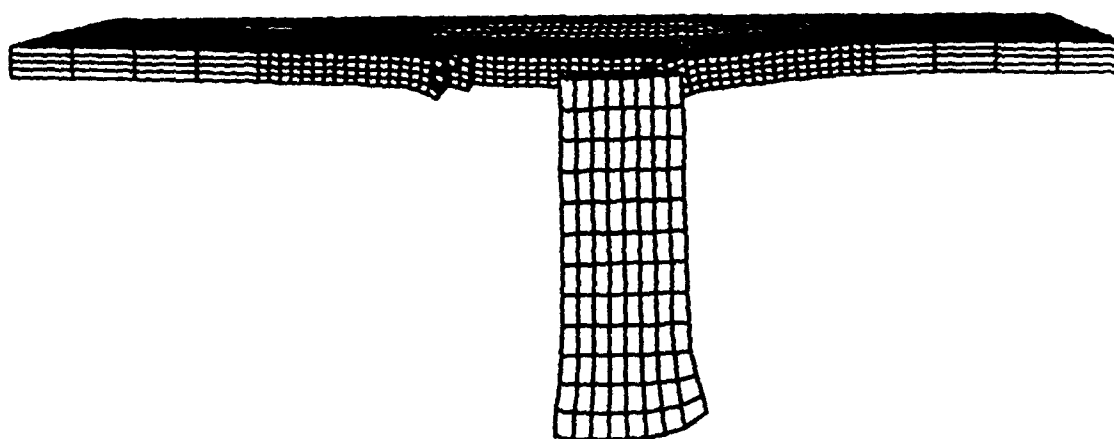


Al Plate ($V_i=450$ m/s, $V_t=133.3$ m/s)
time = $0.49102E-05$

Fig. C-24a A deformable blunt striker impacts on a 1/8 in thick aluminum plate



Al Plate ($V_i=450$ m/s, $V_t=133.3$ m/s)
time = $0.48984E-04$



Al Plate ($V_i=450$ m/s, $V_t=133.3$ m/s)
time = $0.98936E-04$

Fig. C-24b A deformable blunt striker impacts on a 1/8 in thick aluminum plate

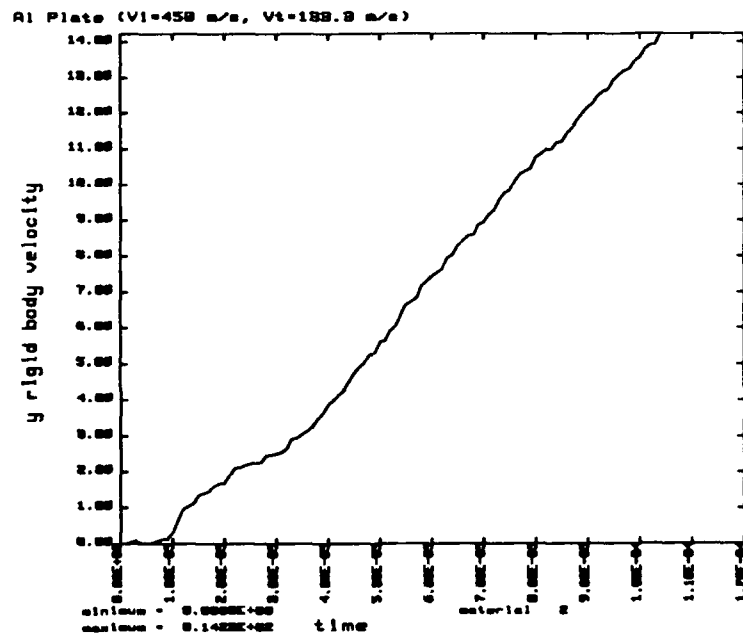
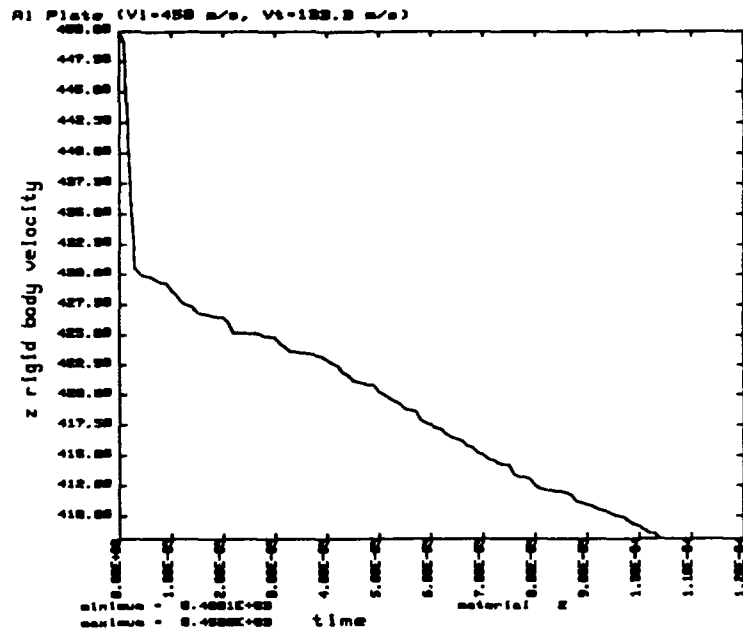
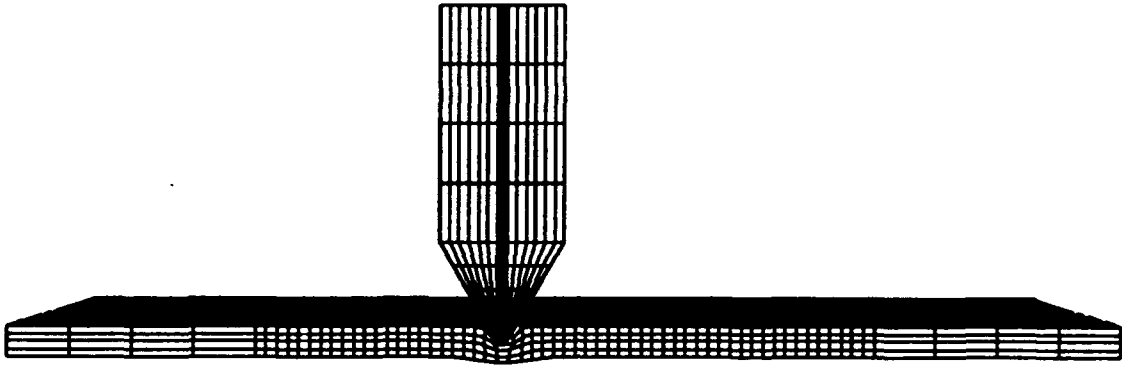
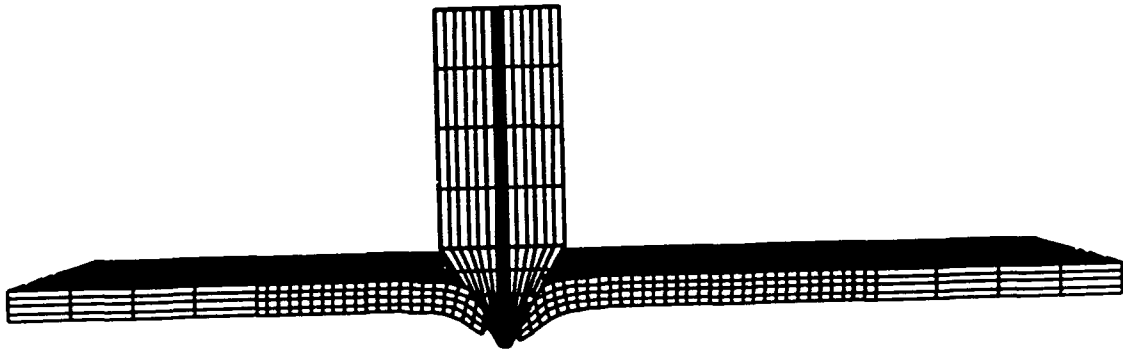


Fig. C-24c Rigid body velocity components for case shown in Fig. C-24a and 24b

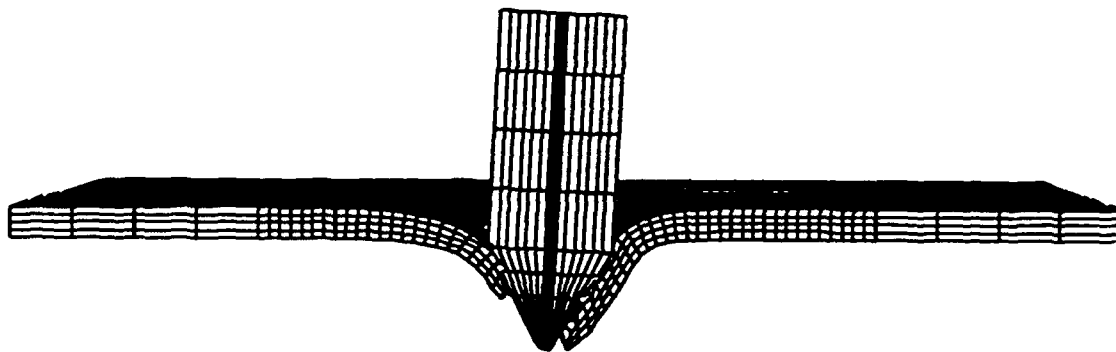


Al Plate ($V_i=450$ m/s, $V_t=133.3$ m/s)
time = $0.11932E-04$

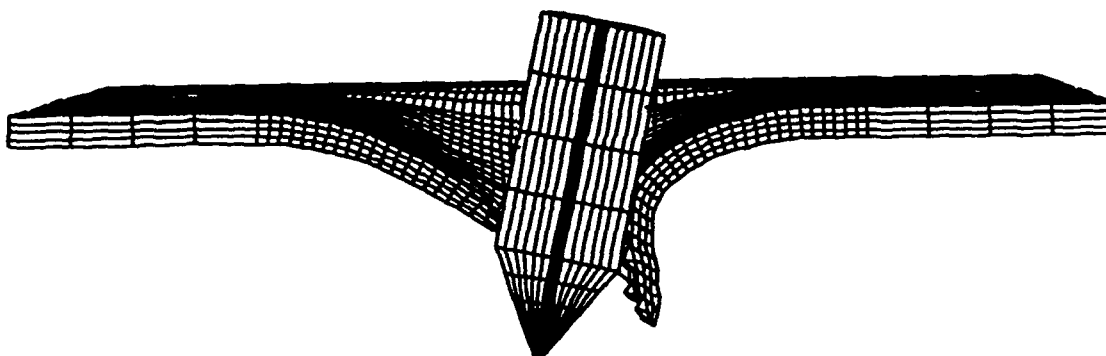


Al Plate ($V_i=450$ m/s, $V_t=133.3$ m/s)
time = $0.23941E-04$

Fig. C-25a A conical-tipped striker impacts on a 1/8 in thick aluminum plate



Al Plate ($V_i=450$ m/s, $V_t=133.3$ m/s)
time = $0.41992E-04$



Al Plate ($V_i=450$ m/s, $V_t=133.3$ m/s)
time = $0.71939E-04$

Fig. C-25b A conical-tipped striker impacts on a 1/8 in thick aluminum plate

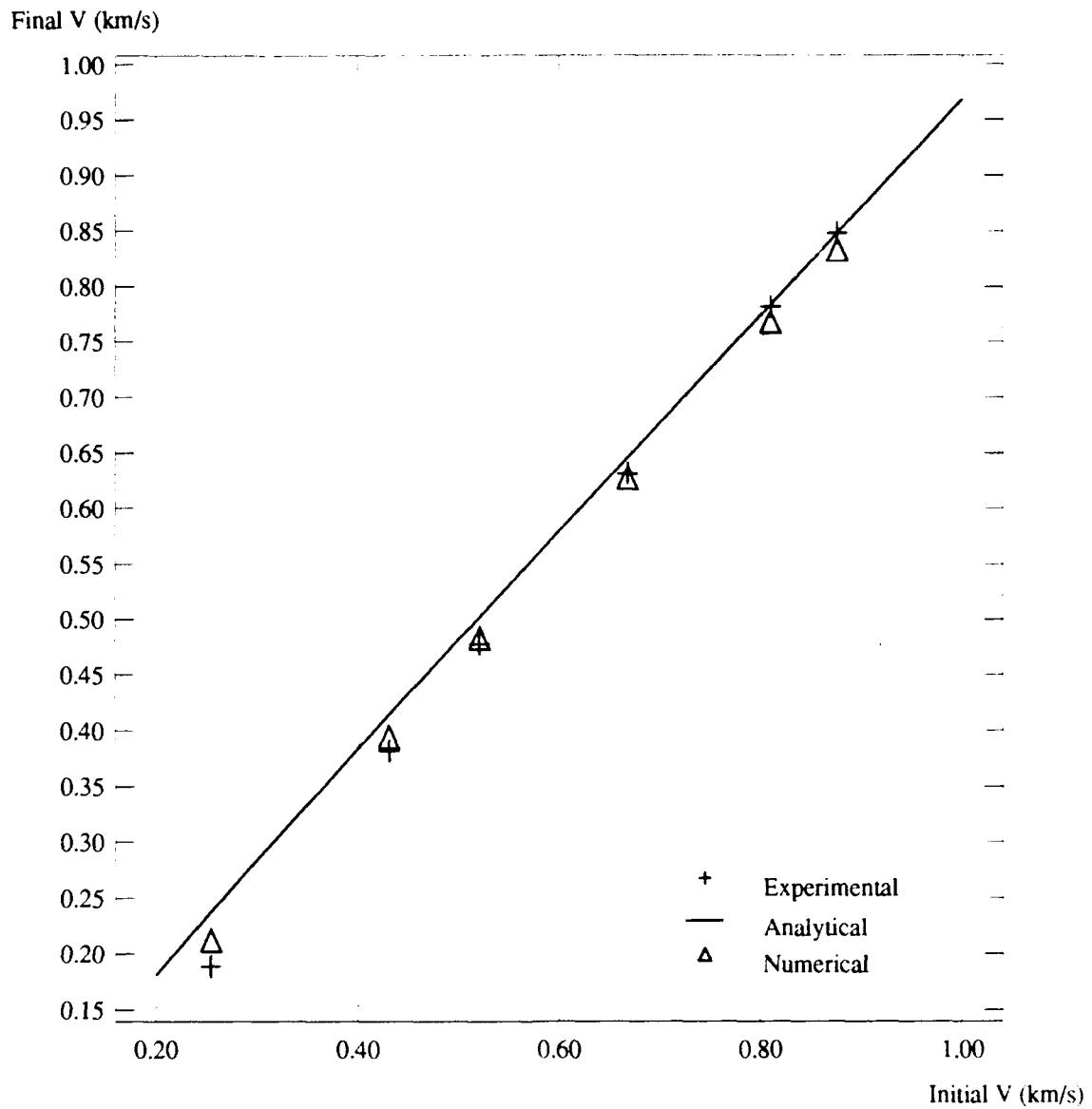


Fig. C-26 Final velocity of the striker
 (Blunt strikers impact on 1/8 in thick Al plates moving at a speed of 93.1 m/s)

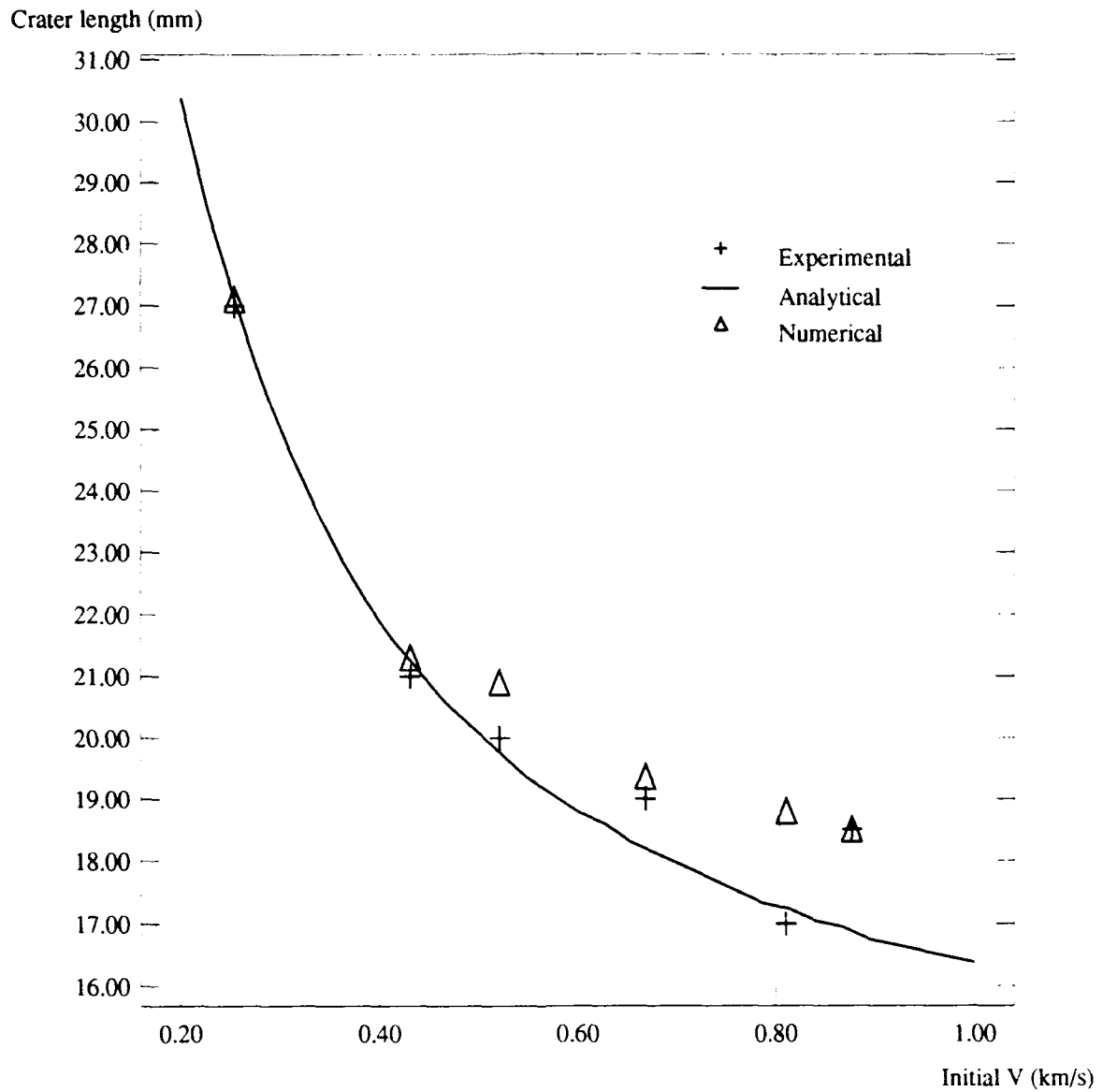


Fig. C-27 Crater length of the target
 (Blunt strikers impact on 1/8 in thick Al plates moving at a speed of 93.1 m/s)

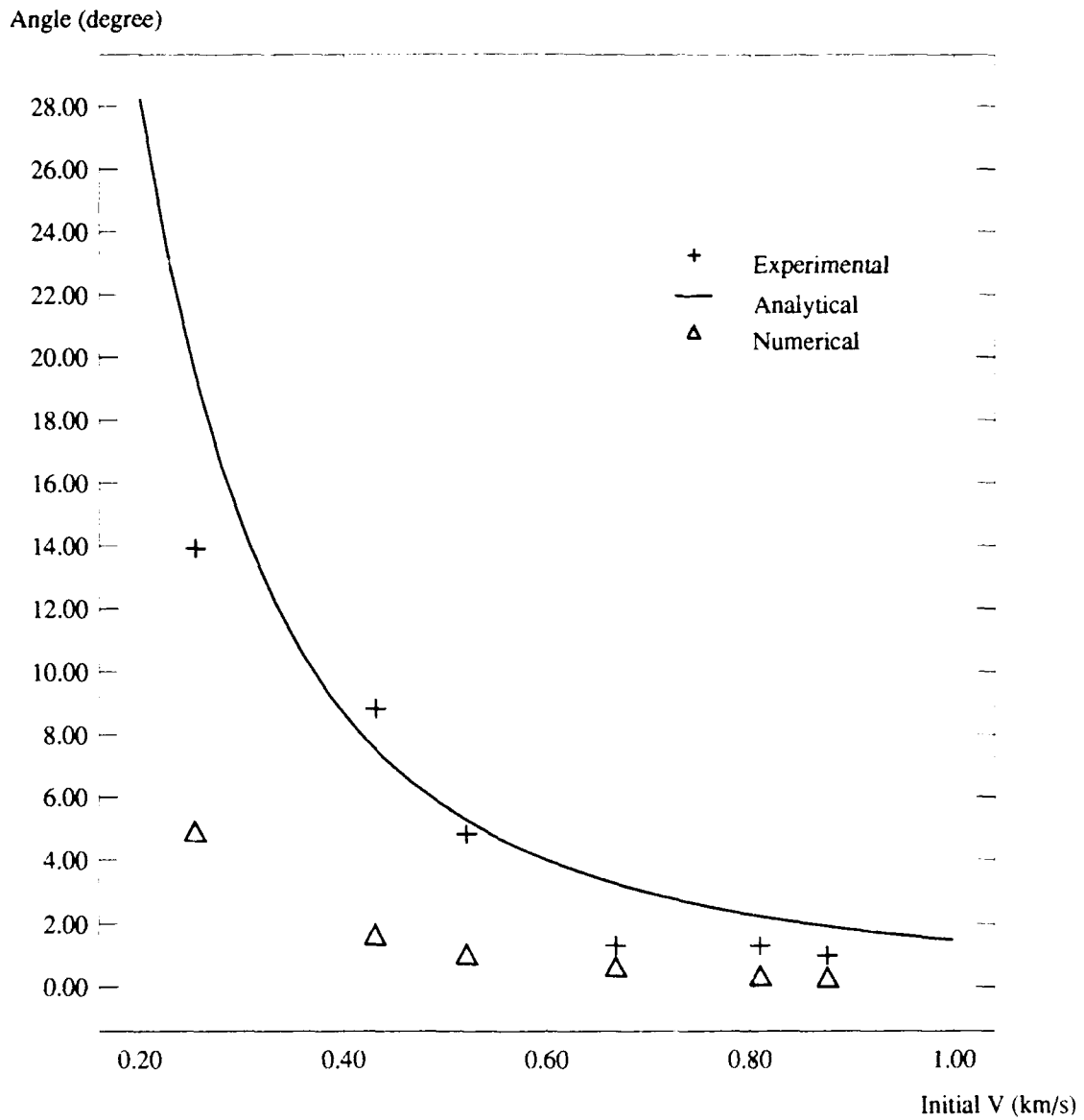


Fig. C-28 Trajectory angle of the striker
 (Blunt strikers impact on 1/8 in thick Al plates moving at a speed of 93.1 m/s)

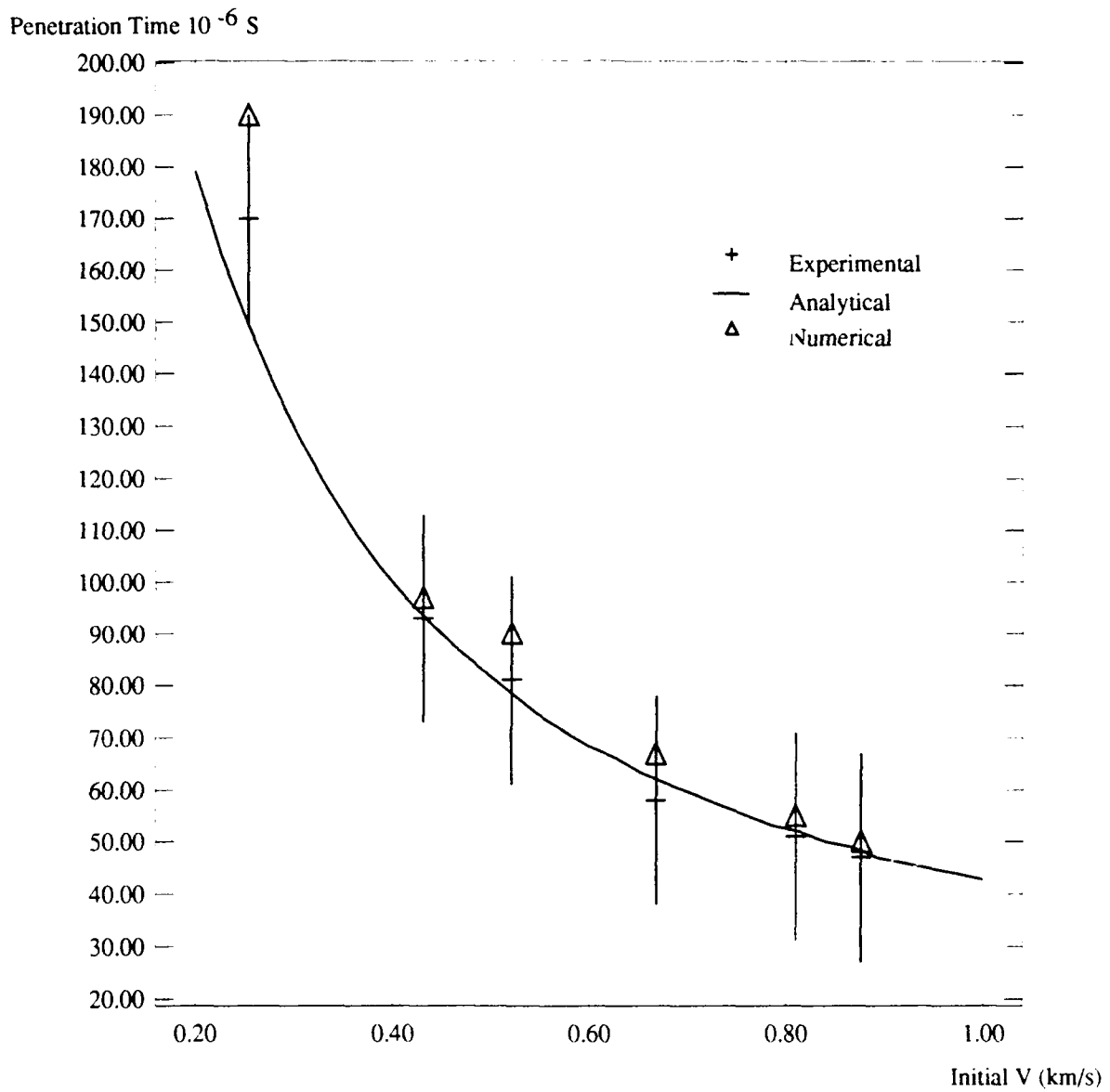


Fig. C-29 Penetration time
 (Blunt strikers impact on 1/8 in thick Al plates moving at a speed of 93.1 m/s)

APPENDIX

YAWING IMPACT ON THIN PLATES BY BLUNT PROJECTILES

by

Werner Goldsmith, Eric Tam* and David Tomer**
Department of Mechanical Engineering
University of California, Berkeley, CA 94720

* Current address:

**Current address: RAFAEL, P. O. Box 2250, Haifa, Israel

ABSTRACT

Two series of experimental investigations and an analytical study correlated with one of these were conducted to examine the phenomena attendant to the normal impact of blunt-nosed, hard-steel strikers but moderate angles of yaw (ranging from normal up to 190°) against stationary thin plates of aluminum and steel. The projectiles for the two sequences were 6.35 mm and 6.2 mm in diameter with corresponding lengths of 20 and 19 mm, respectively. The first set of runs involved 2024-0 aluminum and 4130 steel targets with a thickness of 3.175 mm, while the second utilized this thickness for the 2024-0 aluminum, but a thickness of 1.588 mm for the corresponding steel plate. The samples were circular with a 140 mm diameter and were clamped in a holder attached to a massive base. Initial velocities ranged from 115 to 285 m/s.

The experiments were designed to ascertain the ballistic limit at the various yaw angles. The ballistic limit is the initial velocity of a particular striker required to just perforate a specified target, usually at normal incidence, in 50 percent of a large number of identical tests. At higher initial speeds, where the projectile was ejected with a final velocity, this value and the final oblique angle were also determined. Post-mortem examination of the plates indicated that damage and failure occurred by bulging, lateral indentation, and side and front petaling.

A theoretical model was developed that analyzed the impact by dividing the process into five stages, utilizing simplifying phenomenological assumptions. These phases consisted of (1) initial striker penetration; (2) normal impact and tensile plate failure; (3) initial rotation of the projectile; (4) shearing and ejection of a plug; and (5) target petaling. A major assumption was the use of a membrane representation for stage (2). Consecutive phases prevailed except for the simultaneity of domains (2) and (3). Two of these steps were identical to those employed in a model of impact on moving targets.

The present analytical model underpredicted the ballistic limit by up to 14.4%, but better correlation was found at higher yaw angles. Excellent agreement was observed between the experimental and analytical final velocities when the data points were corrected to reflect the difference between the experimental values of the ballistic limit and that predicted by the model. Fair agreement was found between the experimental and the analytical values of the oblique angle in spite of the paucity of the data obtained due to the limitations imposed by the equipment.

INTRODUCTION

The simulation of the impact and perforation of plates has been studied extensively, but virtually exclusively under the hypothesized conditions of a stationary target and the normal impact of a non-yawed, non-rotating projectile [c.f. 1-4]. Furthermore, a smaller subset of these investigations has been restricted to thin targets, i.e. those where stress and deformation gradients throughout the thickness are neglected. In the field, those ideal situations are never encountered; however, their examination facilitates the evaluation of the effects of striker rotation, obliquity, yaw and that of a moving target. A further limitation on the relevant literature is the fact that a substantial number of the previous studies have been concerned with long rods or with hypervelocity impact conditions which are not relevant to the present investigation.

A number of researchers have attacked the problem of oblique impact on thick or thin targets that encompassed either analytical or experimental investigations or a combination of these [5-15]. Several of the theoretical approaches required a priori knowledge of certain mechanical parameters such as the ballistic limit at normal incidence or the size of plugs generated in a perforation process, or the fit of data to a stipulated empirical equation.

The only work to date involving impact on moving targets has been described by Wu and Goldsmith [16, 17] using a series of continuum representations whose evaluation was found to be in reasonable agreement with experimental results. A technique for the repeatable production of tumbling motion and a preliminary set of target responses has been described by Ruiz and Goldsmith [18, 19].

The present study consists of the experimental determination of the effect of striker yaw, up to 19° , on the penetration and perforation of thin metallic plates by relatively short projectiles at speeds of the order of 100-300 m/s and development of an analytical model for this process, partially adapted from [17]. It is not otherwise related to the rare previous publications involving yawing motion. One of the first comments on this subject is due to Grabarek [20] who estimated that the minimum velocity required for a projectile to perforate a plate at yaw angles up to 3° would need to be increased by no more than 1%. A study by Bless et al. [21] used reversed ballistics for long rods where the target plates were moved towards a stationary striker; the penetration depth was found to depend on the rod diameter and the yaw angle.

EXPERIMENTAL ARRANGEMENT

The general arrangement for the tests have been previously described in substantial detail [16, 21]; a schematic of the system is presented in Fig. 1. The propulsion mechanism for the principal tests consisted of a gun using compressed nitrogen as the driving agent whose 1.37 m long barrel was supported by means of three brackets with the breech movable along a set of rails; the entire unit was mounted on a massive table. Two steel barrels, each 1.37 m long, were used for the shots with a 12.7 mm I.D. unit employed for all yawed tests, where a sabot was required, while a few shots at normal incidence utilized a 6.35 mm diameter tube. Two horizontal slots near the

muzzle end permitted the passage of two parallel laser beams, focused on a set of photodiodes, whose interruption by projectile traverse generated signals recorded on an oscilloscope that permitted the determination of the striker velocity; these slots also prevented further bullet acceleration. The gun can launch a 6.7 g projectile/sabot combination at a peak speed of about 250 m/s. In one series of tests projectiles were fired by means of a powder gun with the initial velocity measurement occurring in front of the muzzle. The ballistic test stand was located in an isolation chamber; firing was initiated remotely and the chamber was evacuated for the powder gun tests.

Two series of blunt-nosed cylindrical projectiles were fabricated from heat-treated oil-hardened drill rod. The first series involved strikers of 6.2 mm diameter, 19 mm length, and masses of 4.5 g with a hardness R_C 50; for a second sequence, these values were 6.35 mm, 20 mm, 5 g and R_C 60. No deformation of these strikers was observed in any of the tests, justifying the assumption of a rigid body in the corresponding analytical development.

In order to generate impact at the desired angle of yaw, the projectiles were embedded prior to launching in a sabot with length, diameter and mass of 19 mm, 12 mm and 2.2 g for the first series and 12.7 mm length and diameter with a mass of 2.9 g for the second. The lighter sabot was composed of polycarbonate, slotted so as to fly apart upon impact, while the second involved an integral Teflon cylinder. Holes with diameters corresponding to those of the projectiles, with a slight interference fit that ensured their union during flight were drilled into the sabots at obliquities of 0, 5, 10, 15 (and, for the second series, 19) degrees. Small yaw angles correspond to those found in practice and are, furthermore, required for trajectory stability. Hole depths ranged from 9.5 to 10.2 mm. Attempts failed to remove the sabots from the projectile by their impingement on the edge of a hole with a diameter slightly larger than the presented projectile area, drilled in a

metallic plate placed just outside the muzzle; while separation was effected, the strikers were subjected to an undesired tumbling motion. In consequence, the striker/sabot combination struck the target; post-mortem examination of the targets revealed only a superficial annular mark on the entry side, attributable to the impact of the sabot, with no observable indentation.

Targets consisted of 140 mm diameter circular plates of 2024-0 aluminum with a thickness of 3.175 mm or SAE 4130 steel with thicknesses of either 1.59 mm or 3.175 mm. The yield and ultimate tensile strength and and tensile strain of the 2024-0 aluminum series were selected as 200 MPa, 240 MPa and 0.22 (taken from [16]).* For the SAE 4130 steel, the corresponding values for the first series were selected as 560 MPa, 780 MPa, and 0.28, while the yield and failure stresses for the second series were found to be 690 and 930 MPa*, respectively. The targets were clamped by means of three screws each inside two circular brackets and a corresponding steel holder bolted to the table, as shown in Fig. 2. Side constraints were removed to permit high-speed photographic examination of the perforation process. On the average, the distance of the target from the muzzle of the gun was 190 mm.

In a number of tests, the exit velocity of the striker after perforation was determined from the signals generated by the closure of a battery-energized circuit for each of two sets of closely-spaced parallel aluminum foils held by wooden frames; this eventuated when the metallic projectile ruptured the sheets and produced contact between them. In other experiments, this velocity as well as the perforation event was obtained from the photographic records of a Beckman-Whitley W-2 framing camera recording a series of 79 individual frames by means of a rotating prism at framing rates of the order of 44,000-50,000 pictures per second. Illumination by a Singer Graflex

*Strength magnitudes vary depending on heat treatment. Even treatments listed as identical have resulted in different quoted values in the literature.

triggered the flash via a delay box and a differential amplifier during the continuous operation of the camera.

PROCEDURE

The ASA 400 panchromatic 35 mm film is taped to the spool of a cassette so that it can be wound at the end of each shot. An approximate value of the initial projectile velocity was determined, ranging from 130-200 m/s for the pneumatic gun and previously ascertained for the chamber pressure, and up to 240 m/s for the powder gun for predetermined powder weights used in a particular test. This value controls the delay setting for the flash unit so that illumination commences when the striker enters the field of vision of the camera. The camera speed is adjusted by a rheostat, the room is darkened, the shutter is opened manually and the gun is fired whenever the camera motor has achieved the desired, stable rotational speed. Immediately after the shot, the camera shutter is closed, and the target and projectile are examined with respect to their terminal state.

The film removed from the cassette is processed and examined in an optical comparator with a magnification of 10 which provides the final velocity as well as the phenomenological aspects of the perforation. Comparison of the initial velocity from these photographs with the measured value from laser beam interruption indicates a discrepancy of 4%, which, together with an estimated experimental inaccuracy of 1% amounts to a potential data error of 5%. The oblique angle determined from the film is only the component in the plane normal to the camera view; the deviation from the actual angle is estimated to be about 10%. The permanent deflection of the target was measured by means of a mechanical comparator. Further details concerning the equipment and operation may be found in [23].

means of a mechanical comparator. Further details concerning the equipment and operation may be found in [23].

PERFORATION MODEL

A simple perforation model has been developed to describe the present yawing impact of a blunt cylinder of mass m_p , length L and diameter d on a thin, metallic plate, in the vertical plane based on a post-mortem examination of the experimental results. The sequential aspects of the phenomenon and the definition of the yaw, oblique and trajectory angles α , β , and β' are depicted in Fig. 3. These angles are defined, respectively, as the angle between the velocity vector of the striker and the horizontal x -axis normal to the target, (y is the downward direction in the target plate), that between the axis of symmetry and the horizontal, and the trajectory angle is the angle from the horizontal axis to the velocity vector, $\beta' = \alpha - \beta$. Projectile perforation with yaw, whose sequential phenomenology is indicated in Fig. 4, is regarded to consist of 5 separate stages: (1) initial penetration of the striker into the target without angular deviation under essentially quasi-static conditions, (2) plate failure as if yaw were absent, (3) an initial striker rotation produced by the non-symmetric stress distribution due to oblique entry, (4) additional angular changes while a plug is sheared from the target, and (5) petaling of the target caused by side contact with the striker. Stages 2 and 3 are contemporaneous, while all others are successive; phases 2 and 5 have been adapted from [23].

The striker motion during phase (1) is assumed to consist of a pure translation until the entire face has made contact with the target, Fig. 4b. Plate motion during this interval is neglected; the work done by the stresses acting on the striker faces, assumed to be uniform, are given by

$$U = \int_0^t \int_{\text{surface}} \bar{\sigma} \cdot \bar{v} \, dt = S e_y V_p = S e_y (\pi/8) d^3 \tan \alpha \quad (1)$$

where S_y^e is the effective yield stress, and V_p is the embedded projectile volume in this stage. It is assumed, further, that the stresses act on the projectile only on its front face and are at the yield limit, while the effect of those acting on the periphery is considered to be negligible. For the present experimental conditions, the striker indentation is less than the target thickness so that phase (1) does not result in plate failure. In view of the high loading rate, the yield stress S_y is taken at its dynamic value S_{dyn} and, further, is multiplied by the factor 1.75 quantifying the constraint to side flow in plates [24] so that $S_y^e = 1.75S_{dyn}$. The work-energy equation then provides the velocity v_1 at the end of this state as

$$v_1 = [v_0^2 - (2U/m_p)]^{1/2} \quad (2)$$

After phase (1), the interaction will be modeled as normal impact on a stationary target in view of the small oblique angles encountered in the experiments and the velocity vector is normal to the plate. A membrane model for very thin plates with ratios of thickness to projectile radius $(h/a) < 1$ is an excellent portrayal of this process [17], but it will also be assumed for the present situation where $(h/a) = 1$. The validity of such a model was supported by the observed tensile failures in the targets. Other assumptions include rigid-perfectly plastic behavior of the plate, a rigid striker and a constant dynamic yield strength. The analysis employed here is detailed in [17].

For normal impact, the target fails when the radial strain in its mid-plane at the periphery of the striker attains the ultimate tensile strain of the material. Because of axial symmetry, this failure is complete and results in ejection of a plug. The projectile subsequently encounters no further resistance. However, for yaw impact, it was experimentally found that only the upper portion of the plate failed by tensile (membrane) forces due to the inclination of the striker. Thus, tensile failure is a necessary, but not

a sufficient condition for target perforation. The second condition for perforation is developed in stage (4). Concurrent projectile rotation, phase (3), defined by angle β , will now be examined.

At the end of indentation, three stress components σ_{zz} , σ_{rr} and $\sigma_{r\theta}$ act on the striker surface in contact with the target in the axial, radial and circumferential direction, respectively; these are postulated to have attained the dynamic yield value S_{dyn} , based on the results from [25]. Only the first two stress components produce a moment about the mass center G of the striker; the third does not due to bilateral symmetry. The moment due to σ_{rr} is [23]

$$M_{rr} = S_y d b' (L - b') \quad \text{where } b' = d \tan \alpha \quad (3)$$

is the greatest contact distance along the surface of the projectile. The moment due to M_{zz} is

$$M_{zz} = S_y d^2 b' / \pi \quad (4)$$

These moments act in opposite directions. The net moment, $M_G = M_{rr} - M_{zz}$ produces an angular acceleration $\ddot{\beta}$ which, for a small time interval Δt , can be approximated by

$$M_G = I_0 (\Delta \dot{\beta} / \Delta t) \quad \text{with } I_0 = \left(\frac{1}{16}\right) m_p D^2 + (1/12) m_p L^2 \quad (5)$$

where I_0 is the moment of inertia about the mass center.

For the short plugging times encountered, about $30 \mu s$, it is reasonable to assume a constant acceleration so that

$$\dot{\beta} = M_G t_2 / I_0 \quad \text{or the change in the oblique angle } \Delta \beta = \dot{\beta} t_2 \quad (6)$$

The value of t_2 , measured as starting at the end of stage 1, is either the time required for the generation of tensile failure or that needed for the plate to stop the projectile.

After initial tensile failure of the plate, the striker does not encounter further resistance from the upper plug/plate interface. Experiments indicate that, at the onset of failure, this region constitutes an arc of about

90°. Thus, the force that opposes further projectile translation as well as the torque that rotates the projectile subsequently arise from the shear stress at the periphery of the plug subtended by the remaining 270°. This shear force F_{sh} is then quasi-empirically given by

$$F_{sh} = (3/4) d h^{\prime < t >} S_y \quad (7)$$

where $h^{\prime < t >}$ represents the continually diminishing thickness of the plug still attached to the plate. Its moment arm, in terms of the arc radius r subtended by an angle of 2θ , is $r (\sin \theta / \theta)$.

Application of the linear and angular impulse-momentum principle to the projectile during a time step Δt provides the change in linear and angular velocity during this interval as

$$\Delta v = (F_{sh} \Delta t) / m_p \quad \text{and} \quad \Delta \dot{\beta} = (F_{sh} r_2 \Delta t) / I_0 \quad (8)$$

where r_2 , the moment arm of F_{sh} , is taken as constant. The values of the updated translational and rotational velocity and the new oblique angle are given by

$$v = v_0 - \Delta v; \quad \dot{\beta} = \dot{\beta}_0 + \Delta \dot{\beta}; \quad \beta = \beta_0 + \dot{\beta} \Delta t \quad (9)$$

where the new value of F_{sh} is obtained from Eq. (7).

The value of v_0 at the initiation of plug shear is normal component of the velocity obtained using the membrane equations of motion for plate and projectile and the associated boundary conditions [17][26], i.e.

$$v_0 = \left[\frac{\partial w}{\partial t} \cos \beta \right]_{t=t_3} \quad (10)$$

where t_3 is the time at the end of stage 3 and equals t_2 . For Eqs. (a) and (10), it is assumed that the projectile velocity vector is parallel to its axis during this phase.

With the further assumption that the plug and projectile move as a unit, the decrease in contact area thickness between plug and target is

$$\Delta h^{\prime < t >} = v \Delta t \quad \text{so that} \quad h^{\prime < t >} = h^{\prime < t_0 >} - \Delta h^{\prime < t >} \quad (11)$$

where $h^{\prime} < t_0 >$ is the value at the end of the previous time step. The value of $h^{\prime} < t >$ at the start of stage 4 is assumed to be $h^{\prime} < t > |_{t=t_2} = h / [\cos \beta] |_{t=t_2}$; this stage ends when $h^{\prime} < t >$ reaches zero where the plug separates and no longer moves together with the striker.

After the plug has sheared, the contact of the upper striker periphery with the target produces a force P which, in conjunction with the projectile velocity, creates further deformation and hole enlargement and changes in the rigid-body striker motion; friction is ignored. As detailed in [17], the change in the angular velocity is

$$\Delta \dot{\beta} = (P r_1 \Delta t) / I_0 \quad (12)$$

where r_1 is the distance from the line of action of P to the mass center of the striker. The drag and lift force, P_d and P_ℓ are the components of P along and perpendicular to v (resolved into v_x and v_y) and are given by

$$P_d = P \sin (\beta - \beta') \quad P_\ell = P \cos (\beta - \beta') \quad (13)$$

where $\beta' = \tan^{-1}(v_y/v_x)$. The drag force changes the striker speed by $\Delta v = (P_d \Delta t) / m_p$. The change in trajectory angle is $\Delta \beta' = (v \Delta t) / r_c$ where r_c , the distance to the instant center, is given by $r_c = (m_p v^2) / P_\ell$. The updated values of linear and rotational velocity, oblique and yaw angles can be determined by means of Eqs. (9). During time interval Δt , the projectile position is given by

$$x = x_0 + (v \cos \beta') \Delta t \quad y = y_0 + (v \sin \beta') \Delta t \quad (14)$$

The impact ends when either the penetrator loses contact with the target, ricochets or is embedded (or, equivalently, exits the plate with negligible velocity). The first case occurs when $r_1 > L/2$, while the latter ensues when the striker velocity is reduced to zero. Numerical results from this analysis were obtained by means of FORTRAN and a DEC VAX VS 3600 computer using the Ultrix operating system.

RESULTS AND DISCUSSION

a) Target Damage

A sequence of selected photographs portraying the perforation of a 3.175 mm thick 2024-0 aluminum plate by a projectile/sabot combination striking at an initial velocity of 193 m/s with a 15° angle of yaw is presented in Fig. 5 and shows the splitting of the sabot; the series was taken at a camera speed of 44,320 frames per second. A simulation of the impact process below the ballistic limit is shown in Fig. 6; it consists sequentially of (a) penetration at the initial yaw angle, (b) further penetration due to rotation of the striker around point A that shears the target along the path of B without further penetration at A, and (c-e) subsequent further rotation around point C at the edge of the crater without an increase in the depth of penetration.

Selected results from the first series of tests, including the values of the peak plate deflection and of the ballistic limit v_{50} are summarized in Table 1 for the aluminum and steel targets. All plates experience bulging, especially in the vicinity of the contact area, as illustrated in Figure 7 for the subballistic-limit Run 16. This feature also occurred in the case of embedment, as shown in Fig. 8 for Run 36, and is almost entirely due to the membrane response of the target. For normal impact, bulging and plug ejection are the only damage mode due to axial symmetry.

Under conditions of yaw, the obliquity of the striker generates lateral indentation, as shown in the impact side in Fig. 9, Run 27; it results in an elliptic crater that is more pronounced for higher yaw angles. The photograph also indicates the absence of any noticeable effect due to the presence of the sabot. This feature is absent for normal impact where the final diameter of the hole is slightly smaller than that of the striker due to elastic recovery.

Further plate damage occurs upon projectile perforation and subsequent dissociation from the plate with the generation of a larger hole on the exit

side and cracks emanating from this discontinuity. When only one major crack is present, this phenomenon is termed side petaling [16, 17], as shown in Fig. 10 for Run 19, while front petaling obtains when two (or more) major cracks appear, as depicted in Fig. 11 for Run 33. Side petaling was noted only at yaw angles of 10 and 15 degrees, while front petaling was found only at the highest yaw angle of this series. These features are very similar to the damage patterns observed in impact on moving targets [16]; however, the perforation imprint for the moving target consists of a triangular shank below a more or less circular apex, while that for yaw impact exhibits a more irregular pattern for the head and a shorter shank.

While normal penetration of the striker generates a symmetric plug by shearing, the oblique entry due to yaw, illustrated in Fig. 12 for Run 24 shows that plug removal begins with target failure along the upper edge of the contact area, the region of furthest penetration, while the plug is still in contact with the lower edge. Cross sections of perforated targets at increasing angles of yaw, but similar impact speeds, are shown in Figs. 13a-13c for Runs 6, 19 and 29, respectively. These photographs show that resistance to plug ejection results from the cohesion at the lower interface edge, since the lower part of the target bends with greater curvature than the upper portion. Cross sections of both the aluminum and steel targets, 3.125 mm thick, from the second series of tests are exhibited in Fig. 14a and 14b. These samples were struck at the ballistic limit velocity for normal impact, 133 m/s for aluminum and 152 m/s for steel, respectively and increasing angles of yaw. The evolution of the plug and other phenomena described above are also manifested in these photographs.

b) Ballistic Limit

The experimentally-determined ballistic limit velocities v_{50} for the

3.175 mm thick 2024-0 aluminum targets for series 1 and 2 are listed in the first portion of Table 2. Since this parameter should represent the minimum average of a very large number of shots which just result in complete perforation, minor adjustments in the present data were required to obtain this designated limit. This is due to slight variations in yaw angles and specimen material properties, and in view of the conduct of only a few tests for each impact condition. The data for series 2 were scaled to that of series 1 by the mass ratio of the strikers used in these tests, based on the hypothesis that initial momentum is the principal determinant for perforation. With this adjustment, the ballistic limit data correspond very well. It should also be noted that the sabots for series 2 consisted of hollow cylinders of polycarbonate that, unlike those for series 1, do not break into two pieces.

The theoretical value of the ballistic limit is critically affected by the choice of the dynamic yield strength which depends on the strain rate extant and the test arrangement. A comparison of the data from the series 1 aluminum tests with the predictions of the analysis is provided in the second section of Table 2; the computations have been performed both on the basis of a previously-employed yield strength S_y of 200 MPa [16] and for a higher value of 250 MPa. For the latter, the discrepancy is less than 5%.

It is noteworthy that the results obtained here are consistent with similar comparisons involving moving targets [16-17] where agreement between data and predictions were better for moving than for stationary targets. This is somewhat analogous to the present situation where this correspondence improves as the yaw angle increases [23]. Such a trend is partly due to the use of a membrane theory that does not account for plug shear at normal incidence, but that is indirectly accounted for in the application of the membrane equation which uses a striker velocity reduced from its initial value by the indentation process. The second reason for the superior agreement,

when yaw is present, is that the tensile plate failure criterion must be supplemented by the requirement that the plug must be sheared, necessitating a higher striker velocity.

Table 2 also lists the percentage in the increase of the ballistic limit, Z , for the current experimental results of series 1 and 2 on aluminum, the theoretical value, and the data of [20]. In general, the predicted value of Z is larger than the experimental result, as was also found in the analogous case of moving targets [16-17]. Finally, this table contains the data for the two series on 4130 steel; here, the wide divergence between the two test sequences can only be attributed to a totally different heat treatment of the targets, as evidenced by their different yield and ultimate strengths. The effect of any similar difference in the strength and hardness properties of the two series of aluminum targets would be substantially less in view of their significantly lower magnitudes and annealed condition.

c) Other Features

The theoretical model will predict the final velocity of the projectile in cases of perforation only if the actual impact velocity is scaled to the value of the ballistic limit for the particular yaw angle employed. A typical example for a yaw of 15° is shown in Fig. 15; while, in spite of some scatter due to experimental errors and the difficulty in precisely defining the ballistic limit, agreement with the analysis is good near this value; the divergence increases with initial impact velocity. The largest ratio of terminal to initial velocity was found both analytically and experimentally to occur at 5° yaw.

The final oblique angle could not be measured when the projectile axis was not located in the plane perpendicular to the field of vision. As shown in Fig. 16, the prediction indicate a rapid rise of this parameter with impact

speed near the ballistic limit, followed by an exponential decay. The difficulty of experimentally substantiating this spike is severe; hence the correspondence evident in this figure is considered to be satisfactory.

The present investigation represents the only analysis of yaw impact known to the authors. However, a number of models for oblique impact, which has many similar features, have been proposed. The relations of [6] for the final velocity of the striker have been compared with present experimental results. It was found that the predicted values are, with but one exception, uniformly lower than the present measured exit speeds by 12 - 30 percent. It can only be hypothesized that there are some, as yet unexplained, fundamental mechanistic differences between the two types of impact compared here.

CONCLUSIONS

An experimental investigation of the impact of 3.175 mm blunt, hard-steel strikers with an L/D ratio of 3 against 3.175 mm thick soft aluminum and hard steel target plates in the velocity range from somewhat below to well above the ballistic limit at yaw angles up to 19° revealed target damage involving plug formation, bulging, and lateral indentation. Side petaling was found only for yaw angles of 10° or higher, while front petaling occurred only for 15° and 19°.

An analysis using some features from a moving target impact model involved the consecutive stages of (a) initial indentation, considered to occur at normal incidence, (b) plate motion and failure as though occurring for normal impact concurrent with initial projectile rotation, (c) further projectile rotation during plug ejection, and (d) petaling damage produced by contact with the lateral projectile surface. This model underpredicted the experimental ballistic limit within $12 \pm 2.4\%$; this discrepancy was eliminated from other comparisons by multiplication of the measured initial velocity by

the ratio of the experimental to theoretical ballistic limit. For perforation runs, this yielded good correlation between data and predictions for the final velocity and fair agreement for the oblique angle. The ballistic limit increased with increasing yaw angle, much more so for the stronger than for the weaker metallic target.

ACKNOWLEDGMENT

A portion of this work was sponsored by the Air Force Office of Scientific Research under Contract No. AFOSR F49620-89-C-8127 and another portion by the U.S. Army Research Office under Contract DAAG29-80-K-0052 and by a gift from the FMC Corporation. A part of the work reported constituted a segment of a thesis by the second author submitted in partial fulfillment of the requirements of the M.S. degree at the University of California, Berkeley.

REFERENCES

1. Backman, M. E., and Goldsmith, W., "The Mechanics of Penetration of Projectiles into Plates," Int. J. Engng. Sci., v. 16, pp. 1-99, 1978.
2. Wright, T. W., and Frank, K. "Approaches to Penetration Problems." SMIRT Symposium, No. 14, Impact. Lausanne, Switzerland, 1987.
3. Anderson, C. E., and Bodner, S. R., "The Status of Ballistic Impact Modelling," Int. J. Impact Engng., v. 7, pp. 9-35, 1988.
4. Recht, R. F., "High Velocity Impact Dynamics: Analytical Modeling and Plate Penetration Dynamics." In: High Velocity Impact Dynamics, ed. by J. A. Zukas, et al., New York, J. Wiley, pp.443-513.
5. Zaid, M., and Paul, B., "Oblique Perforation of a Thin Plate by a Truncated Conical Projectile," J. Franklin Inst., v. 268, pp. 25-45, 1959.
6. Recht, R., and Ipson, T. W., "Ballistic Perforation Dynamics," J. Appl. Mech., v.60, pp. 384-390, 1963.
7. Awerbuch, J., and Bodner, S. R., "An Investigation of Oblique Perforation of Metallic Plates by Projectiles," Exp. Mech., v. 17, pp. 147-153, 1977.
9. Backman, M. E., Finnegan, S. A., and Whitman, K. G., "Dynamics of the Oblique Impact and Ricochet of Nondeforming Projectiles against Thin Plates." In" Recent Advances in Engineering Science, ed. by G. C. Sih. Soc. Engng. Sci., Lehigh Univ., pp. 9-20, 1977.
10. Woodward, R. L., and Baldwin, N. J., "Oblique Perforation of Targets by Small Armor-Piercing Projectiles," Int. J. Mech. Sci., v. 21, pp. 85-91, 1979
11. Goldsmith, W., and Finnegan, S. A., "Normal and Oblique Impact of Cylindro-conical and Cylindrical Projectiles on Metallic Plates," Int. J. Impact Engng., v. 4, pp. 83-105, 1986.
12. Sundarajan, G., and Shewmon, P. G., "The Oblique Impact of a Hard Ball against Ductile, Semi-Infinite Target Materials -- Experiments and Analysis," Int. J. Impact Engng., v. 6. [1/ 3-22. 1987.
13. Virostek, S. P. Dual, J., and Goldsmith, W., "Direct Force Measurement in Normal and Oblique Impact of Plates by Projectiles," Int. J. Impact Engng., v. 6, pp. 247-269, 1987.
14. Mayseless, M. et al., "A Computer Model for Oblique Impact of a Rigid Projectile at Ductile Layered Targets," Proc. 11th Int. Symp. on Ballistics, TB9, Brussels, Belgium, 1991.
15. Johnson, G. R., Stryk, R. A., Holmquist, T. J., and Souka, O. A.. "Recent Epic Code Developments for High Velocity Impact: 3D Element Arrangements

- and 2D Fragment Distribution," Int. J. Impact Engng., v. 10, pp. 281-294, 1990.
16. Wu, E., and Goldsmith, W., "Normal Impact of Blunt Projectiles on Moving Targets: Experimental Study," Int. J. Impact Engng., v. 9, pp. 389-404, 1990.
 17. Wu, E., and Goldsmith, W., "Normal Impact of Blunt Projectiles on Moving Targets: Analytical Considerations," Int. J. Impact Engng., v. 9, pp. 405-432, 1990.
 18. Ruiz, O., and Goldsmith, W., "Controlled Tumbling of Projectiles -- I. Theoretical Model," Int. J. Impact Engng., v. 7, pp. 101-115, 1988.
 19. Ruiz, O., and Goldsmith, W., "Controlled Tumbling of Projectiles--II. Experimental Results," Int. J. Impact Engng., v. 7, pp. 285-305, 1988.
 20. Grabarek, C., JTCG/MER Working Party for KE Penetrators, Information Exchange Meeting, Proceedings, Aberdeen Proving Ground, MD, 1973.
 21. Bless, S. J., Barber, J. P., Bertke, R. S., and Swift, H. F., "Penetration Mechanics of Yawed Rods," Int. J. Engng. Sci., v. 16, pp. 829-834, 1978.
 22. Liss, J., and Goldsmith, W., "Plate Perforation Phenomenon due to Normal Impact by Blunt Cylinders," Int. J. Impact Engng., v. 2, pp. 37-64, 1984.
 23. Tam, Eric, Yaw Impact on Plates by Blunt-nosed Projectiles. Thesis (M.S.) Univ. of California, Berkeley, 1991.
 24. Liss, J., Goldsmith, W., and Hauser, F. E., "Constraint to Side Flow in Plates," J. appl. Mech., v. 50, pp. 694-698, 1983.
 25. Liss, J., Goldsmith, W., and Kelly, J. M., "A Phenomenological Penetration Plates," Int. J. Impact Engng., v. 1, pp. 321-341, 1983.
 26. Beynet, P. and Plunkett, R., "Plate Impact and Plastic Deformation by Projectiles," Exp. Mech., v. 11, pp. 64-70, 1971.

TABLE I RESULTS FOR ALUMINUM AND STEEL TARGETS, First Series

Run No.	Yaw Angle, deg.	Initial Velocity, v_0 , m/s	Perforation Status	Final Velocity, v_f , m/s	Maximum Deflection, mm	Final Yaw Angle, °	Comments
<u>2024 Aluminum</u>							
1	0	116	No				Embedment
2	0	134	No		13.2		
3	0	147	No				Embedment
4	0	152	No		10.7		No sabot used
5	0	156	Yes		11.8		V50
6	0	169	Yes	27	10.6		No sabot used
7	0	193	Yes		11.1		
8	5	131	No		13.1		
9	5	146	No		14.5		
10	5	151	No				Embedment
11	5	151	Yes		10.6		V50
12	5	156	Yes	27	12.7		
13	5	166	Yes	67	11.4	13	
14	5	183	Yes	127	11.8	16	
15	5	197	Yes	152	11.5	9	
16	10	155	No		14.8		
17	10	159	Yes		14.7		V50
18	10	168	Yes	40	14.1	15	
19	10	176	Yes	78	13.5	31	
20	10	182	Yes	94	13.7	29	
21	10	193	Yes	120	13.3	19	
22	15	99	No		9.8		
23	15	132	No		12.6		
24	15	148	No		15.3		
25	15	161	No		17.2		
28	15	165	Yes		12.0		V50
27	15	170	Yes	37	14.1		
28	15	171	Yes	61	13.1		
29	15	183	Yes	81	13.5	35	
30	15	193	Yes	105	13.2	26	
31	15	197	Yes	118	14.1	30	
32	15	208	Yes	144	15.1	24	
33	15	234	Yes	187	15.1	21	
<u>4130 Steel</u>							
34	0	151	No		9.9		
35	0	170	Yes		7.1		V50
36	0	175	No				Embedment
37	0	178	No		10.0		
38	0	181	Yes		7.5		
39	10	158	No		7.4		
40	10	163	No		7.6		
41	10	175	Yes		8.0		V50
42	10	189	Yes		7.9		
43	10	195	Yes	39	8.1	11	

TABLE 2. BALLISTIC LIMITS OF TARGETS

Comparison of Data from Series 1 and Series 2, 2024-0 A1

Yaw Angle, deg.	Experimental Ballistic Limit, Ser. 1 v50, m/s	Experimental Ballistic Limit, Ser. 2 v50i, m/s	Adjusted Ballistic Limit, Ser. 2 v50a, m/s*	% Difference, (v50 - v50a)/v50
0	153	133	148	3.3
5	156	139	154	1.3
10	159	143	159	0
15	165	146	162	1.8
19		185		

*v50a is the ballistic limit for the second series adjusted for the mass difference in projectile/sabot mass between the two series, $v50a = v50i(5.0/4.5)$

Comparison of Theoretical and Experimental Values, 2024-0 A1

Yaw Angle, deg.	Experimental Ballistic Limit, Ser. 1 v50, m/s	Theoretical Ballistic Limit, v50t, m/s		% Difference (v50 - v50t)/v50	
		(a)	(b)	(a)	(b)
		S _y = 200 MPa	S _y = 250 MPa		
0	153	131	146	14.4	4.6
5	156	138	154	11.5	1.3
10	159	144	160	9.4	-0.6
15	165	150	166	9.1	-0.6

Percent Increase in Ballistic Limit with Yaw

$$Z = 100 \times (v50^{<a^0>} - v50^{<0^0>}) / v50^{<0^0>}$$

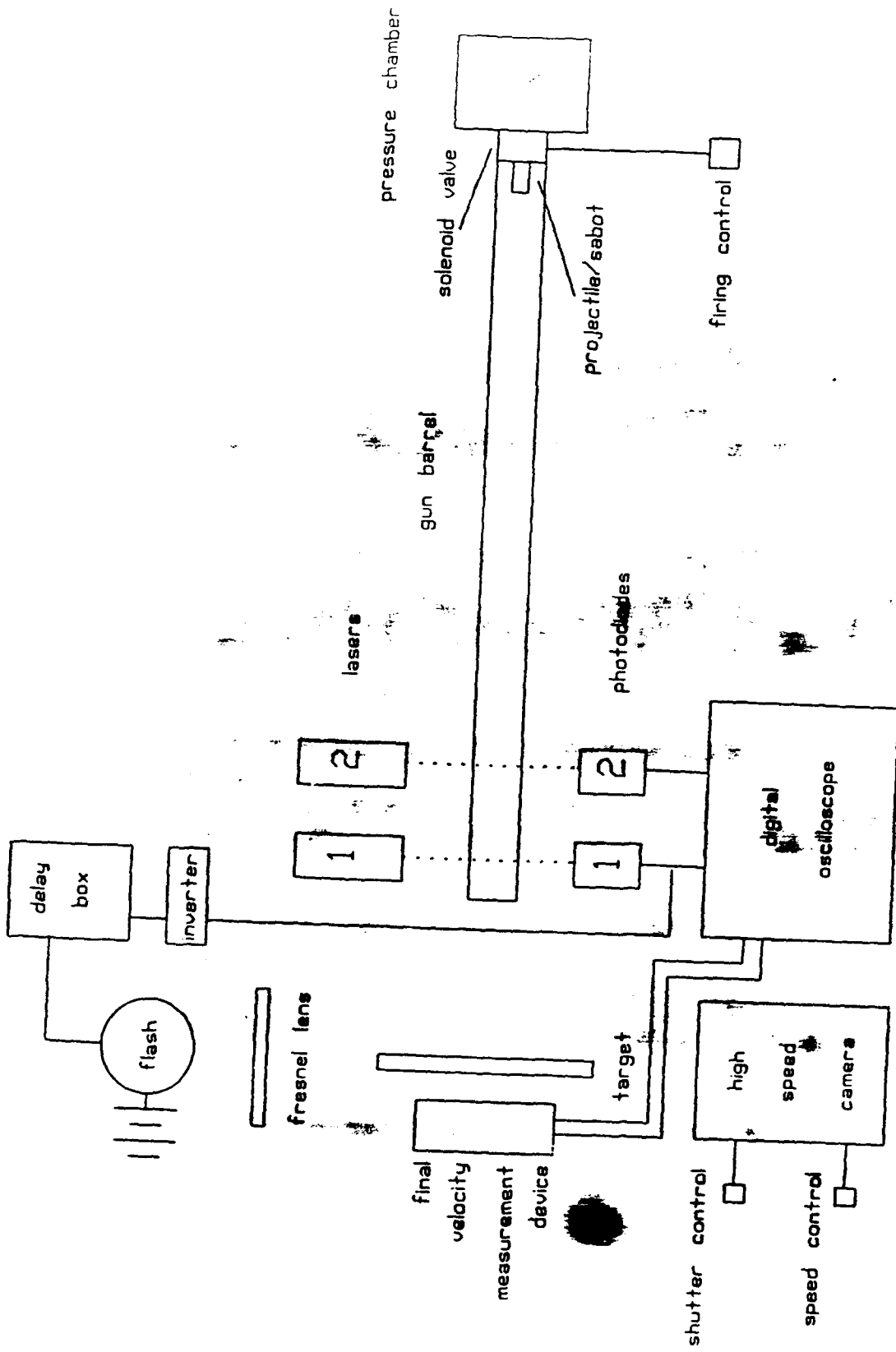
Yaw Angle, deg.	Series		Theory	Ref. [20]
	1	2		
5	2.0	4.5	5.3	3
10	3.9	7.5	9.2	12
15	7.8	9.8	13.7	--
19		12.6		

Experimental Value of the Ballistic Limit for 4130 Steel, m/s

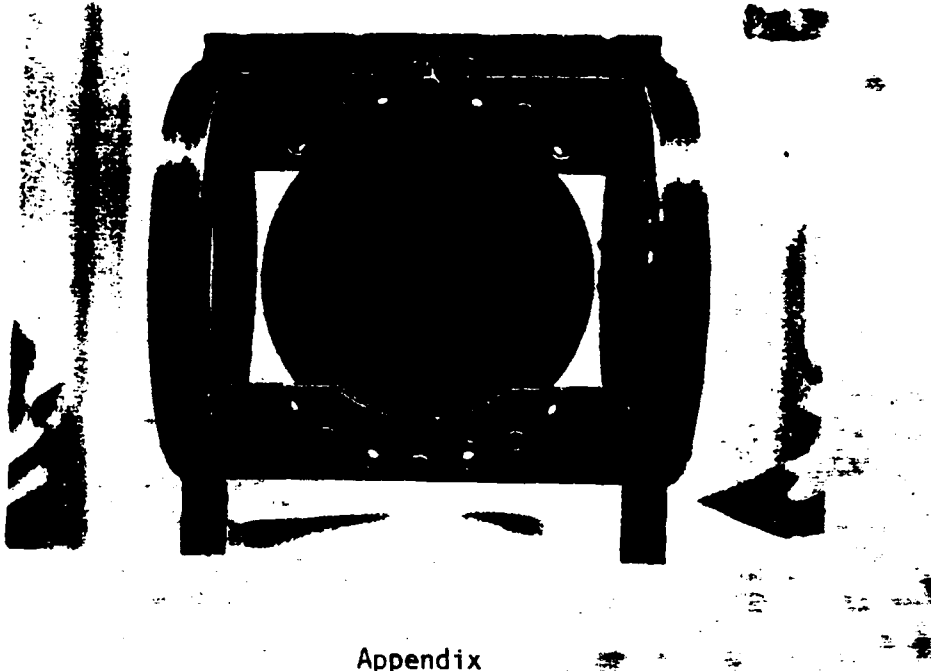
Yaw Angle, deg.	Series 1	Series 2 v50i	Adjusted Series 2 v50a
0	170	148	164
5		200	222
10	175	230	256
15		259	288
19		288	365

CAPTIONS FOR FIGURES

- Fig. 1 Schematic of Experimental Arrangement
- Fig. 2 Exit Side View of Target in Holder
- Fig. 3 Definition of the Yaw Angle, α , oblique angle, β , and Trajectory Angle, β' .
- Fig. 4 Penetration and Perforation Model of Impact with Yaw of a Cylindrical Projectile on a Thin Plate
- Fig. 5 Perforation Sequence for Run 30, 2024-0 Aluminum Target struck at 193 m/s at a 15° Yaw Angle with a Camera Speed of 44320 frames/s.
The sabot is seen to break into two pieces
- Fig. 6 Simulation of the Penetration Process
- Fig. 7 Bulging of the Aluminum Plate for Non-perforation Run 16 ($v_0 = 155$ m/s; $\alpha = 10^\circ$)
- Fig. 8 Bulging of the Steel Plate at the Ballistic Limit, Run 36 ($v_0 = 175$ m/s, $\alpha = 0^\circ$)
- Fig. 9 Lateral Deformation of the Aluminum Plate, Run 27 ($v_0 = 170$ m/s, $\alpha = 15^\circ$)
- Fig. 10 Side Petaling of the Aluminum Plate, Run 19 ($v_0 = 176$ m/s, $\alpha = 10^\circ$)
- Fig. 11 Front Petaling of the Aluminum Plate, Run 33 ($v_0 = 234$ m/s, $\alpha = 15^\circ$)
- Fig. 12 Cross Section of a Nonperforated Aluminum Plate, Run 24 ($v_0 = 148$ m/s, $\alpha = 15^\circ$)
- Fig. 13a to 13c Cross Section of Aluminum Plates for Perforation Run 6 ($v_0 = 169$ m/s, $\alpha = 0^\circ$); Run 19 ($v_0 = 176$ m/s, $\alpha = 10^\circ$), and Run 29 ($v_0 = 183$ m/s, $\alpha = 15^\circ$)
- Fig. 14 Perforation into Targets at the Ballistic Limit Speed with Yaw, Series 2: (a), Aluminum, $v_0 = 133$ m/s, $\alpha = 0^\circ, 5^\circ, 10^\circ, 15^\circ, 19^\circ$
(b) Steel, $v_0 = 148$ m/s, $\alpha = 0^\circ, 5^\circ, 10^\circ, 15^\circ$
- Fig. 15 Final vs. Initial Velocity for Aluminum, Series 1, at $\alpha = 15^\circ$
- Fig. 16 Final vs. Initial Oblique Angle, β , for $\alpha = 5^\circ$



Appendix Fig. 1 Schematic of Experimental Arrangement



Appendix

Fig. 2 Exit Side View of Target in Holder

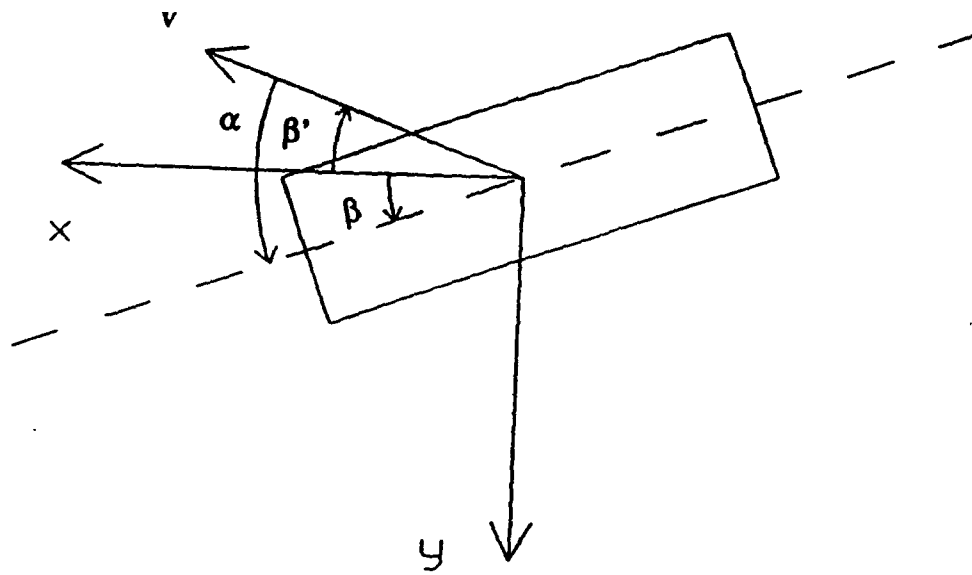


Fig. 3

Appendix

Definition of the yaw angle (α), oblique angle (β), and trajectory angle (β').

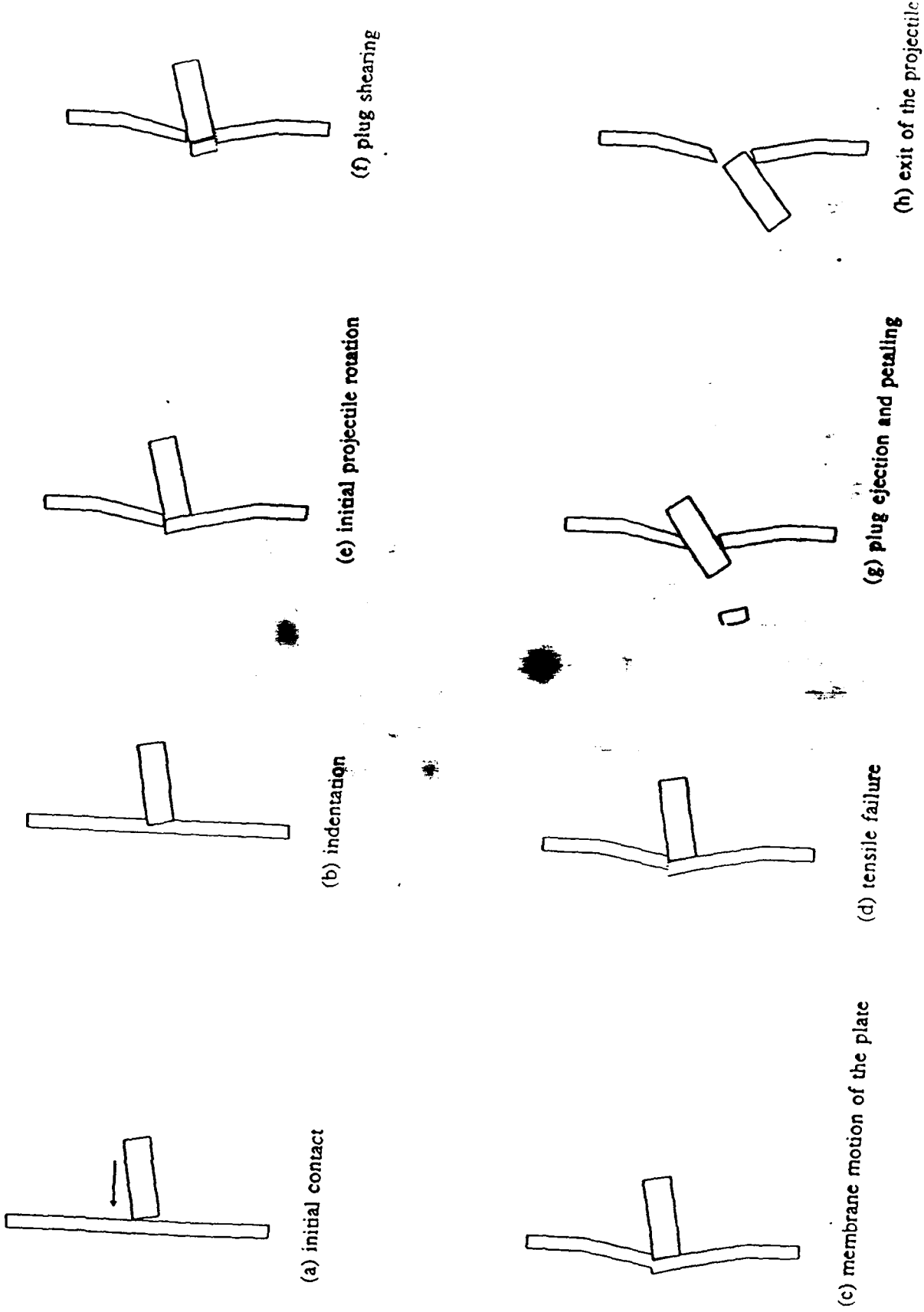
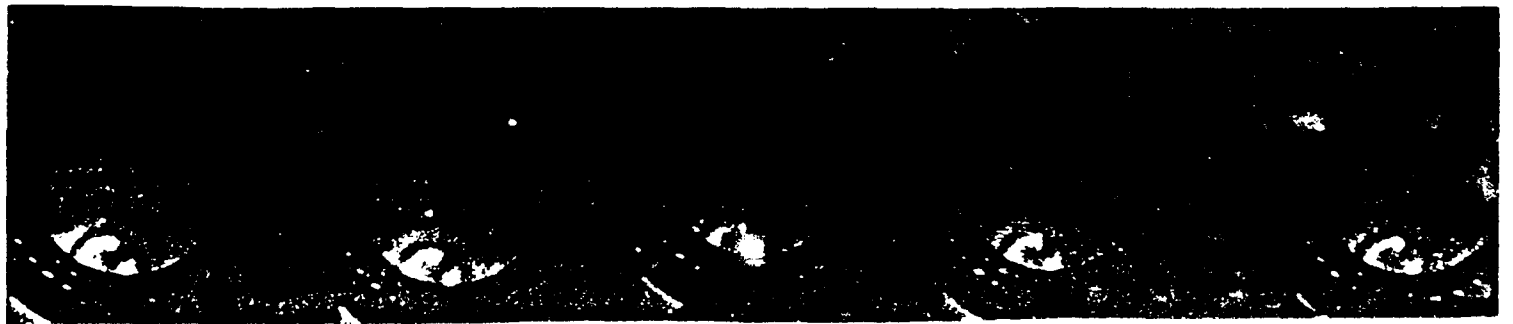
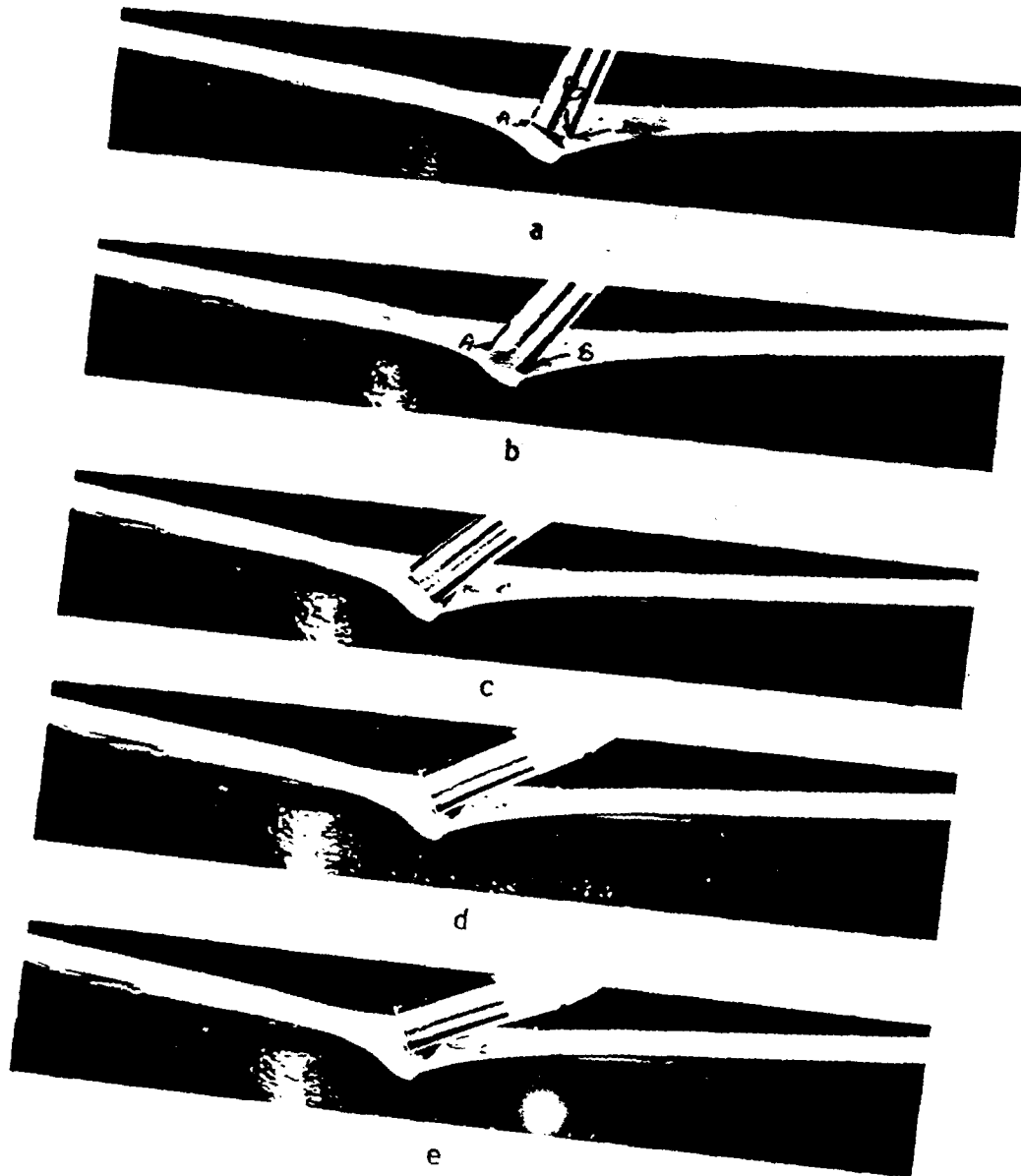


Fig. 4 Penetration and perforation model--impact with yaw.

Appendix





Appendix
Fig. 6 Simulation of the Penetration Process

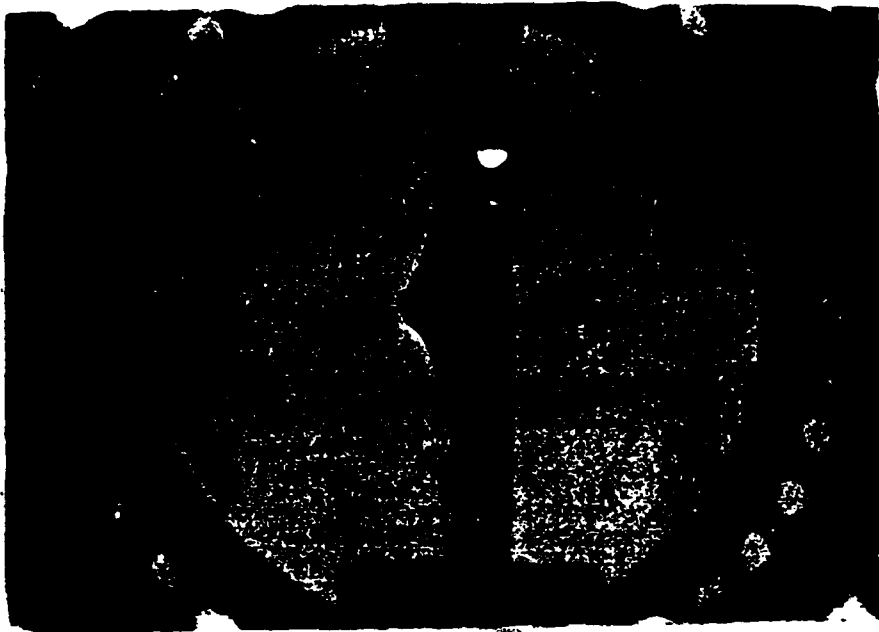


Fig. 7 Bulging of the Aluminum Plate for Non-perforation Run 16
($v_0 = 155$ m/s; $\alpha = 10^\circ$)

Appendix

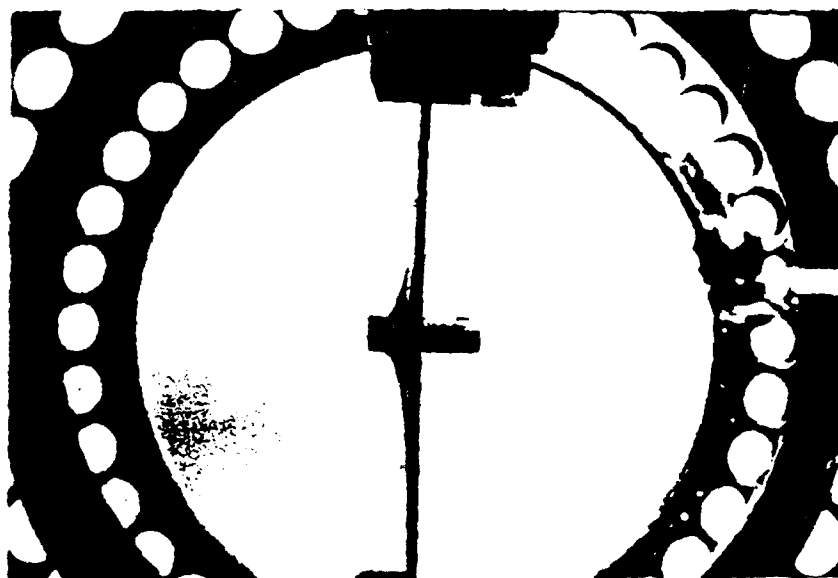
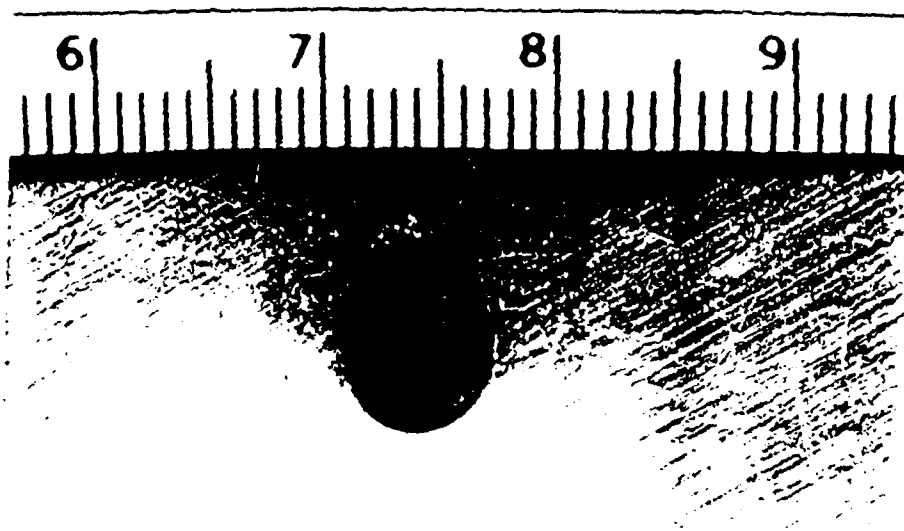


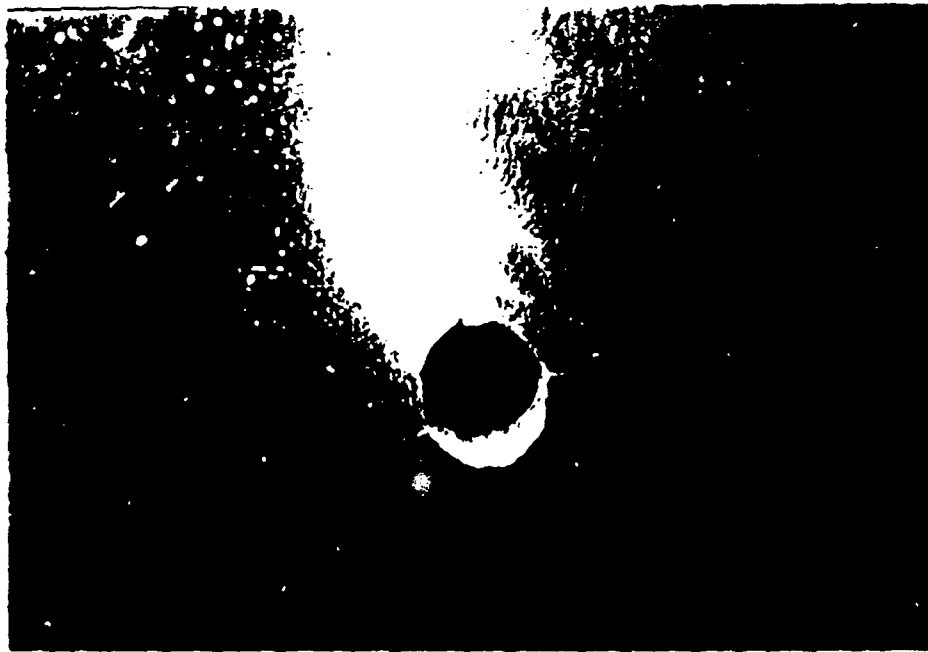
Fig. 8 Bulging of the Steel Plate, Run 30 ($v_0 = 175$ m/s, $\alpha = 0^\circ$)

Appendix



Appendix

Fig. 9 Lateral Deformation of the Aluminum Plate, Run 27
($v_0 = 170$ m/s, $\alpha = 15^\circ$)



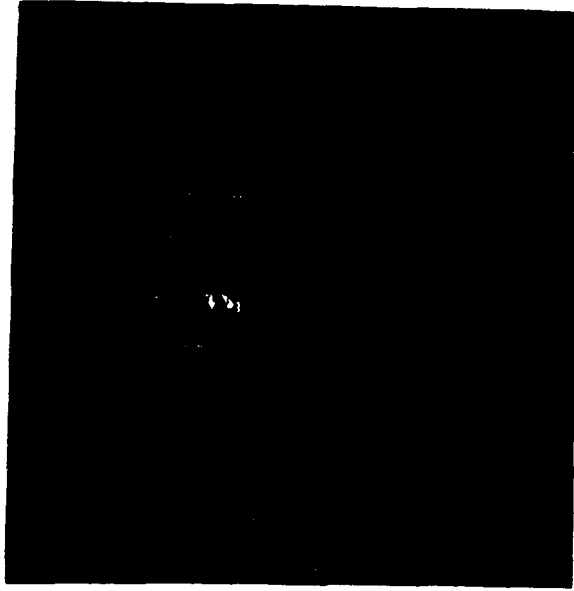
Appendix

Fig. 10 Side Petalling of the Aluminum Plate, Run 19 ($v_0 = 176$ m/s, $\alpha = 10^\circ$)



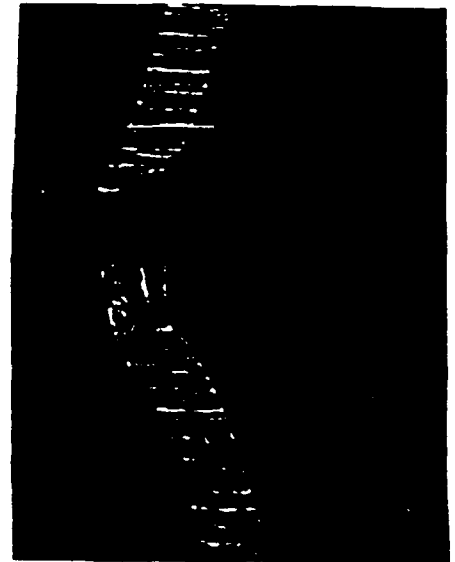
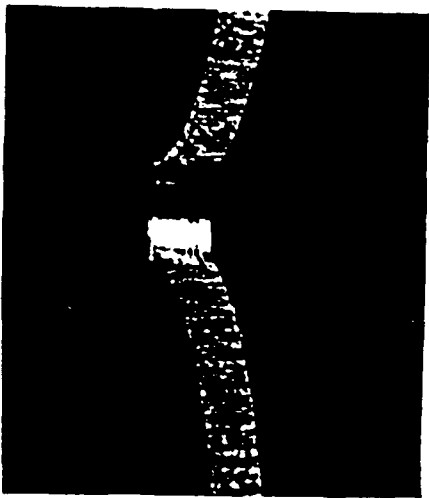
Appendix

Fig. 11 Front Petalling of the Aluminum Plate, Run 33 ($v_0 = 234$ m/s, $\alpha = 15^\circ$)



Appendix

Fig. 12 Cross Section of a Nonperforated Aluminum Plate, Run 24
($v_0 = 148$ m/s, $\alpha = 15^\circ$)



(a)

(b)

(c)

Run 6 ($v_0 = 169$ m/s,
 $\alpha = 00^\circ$)

Run 19 ($v_0 = 176$ m/s,
 $\alpha = 10^\circ$)

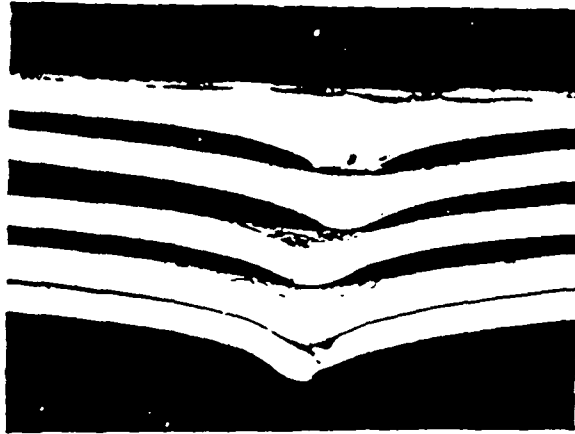
Run 29 ($v_0 = 183$ m/s,
 $\alpha = 15^\circ$)

Appendix

Fig. 13 Cross Section of Aluminum Plates for Perforation Runs

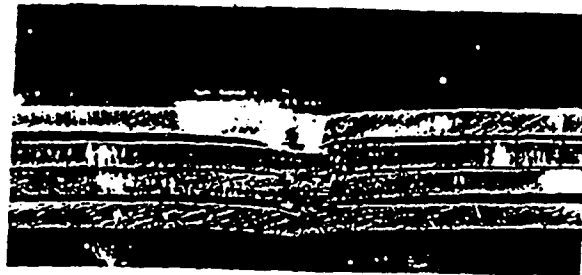
Yaw Angle

0°
5°
10°
15°
19°



(a)

0°
5°
10°
15°

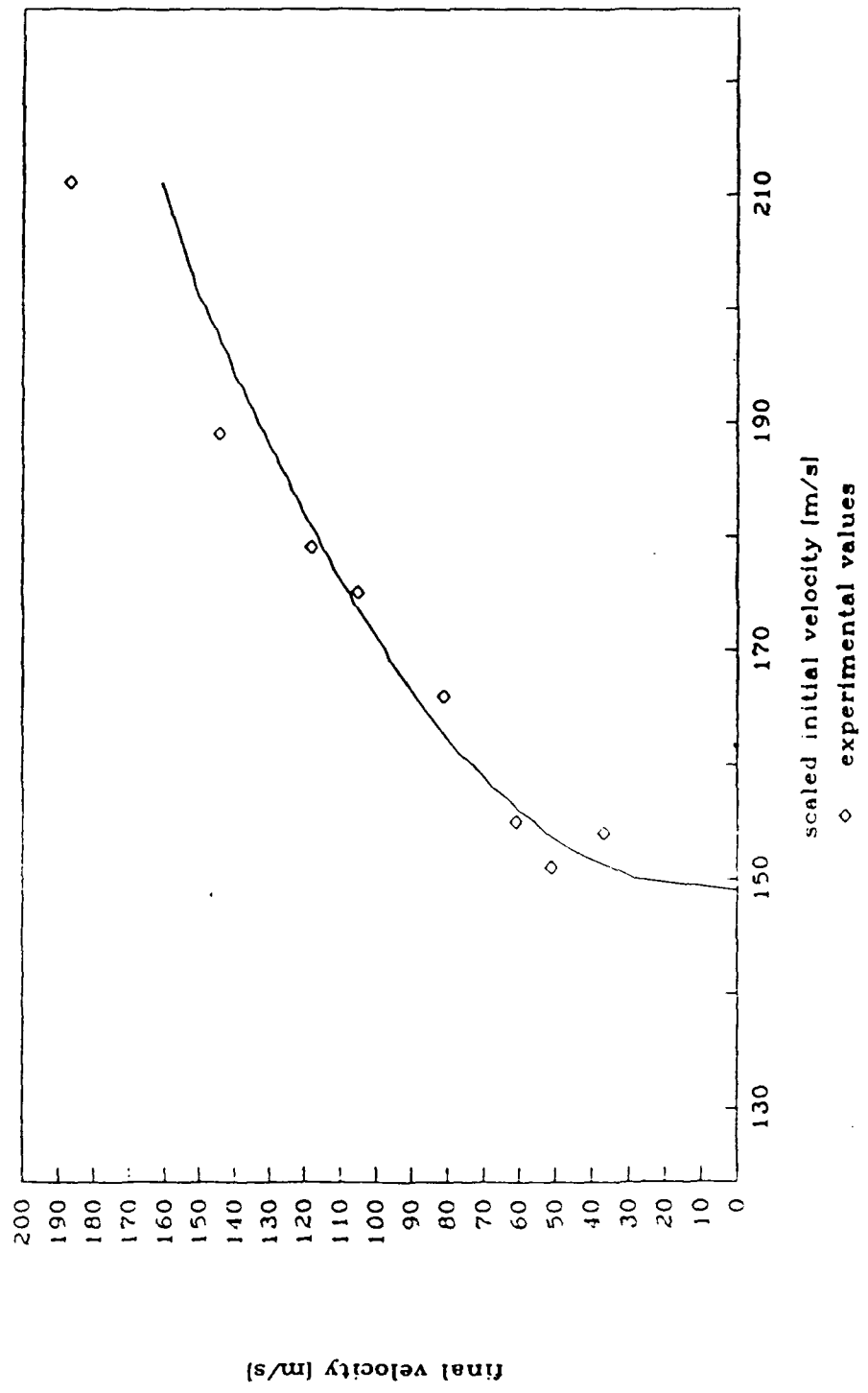


(b)

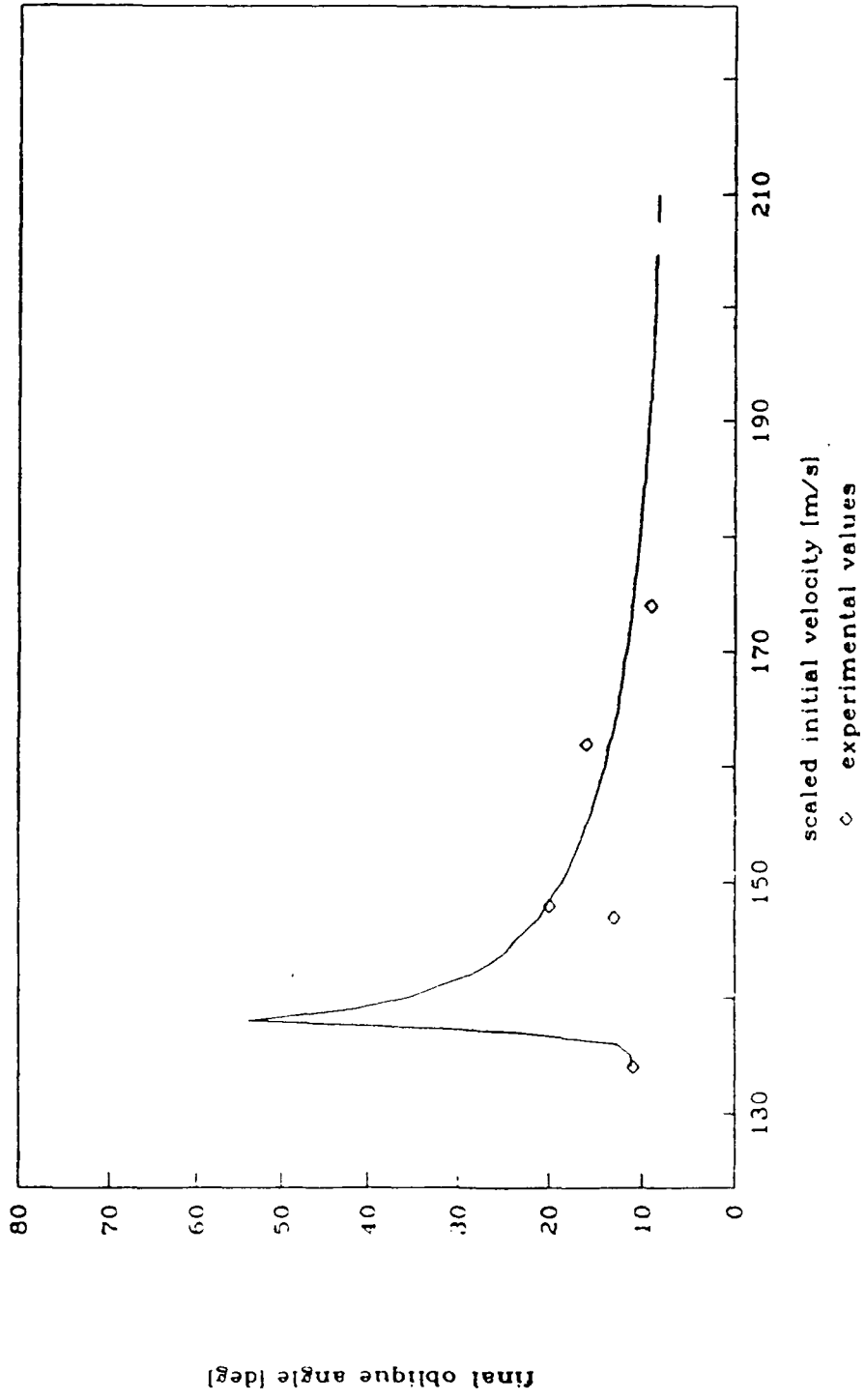
Appendix
Fig. 14 Perforation Into Targets at the Ballistic Limit Speed
with Yaw, Series 2

(a) Aluminum, $v_0 = 133$ m/s, $\alpha = 0^\circ, 5^\circ, 10^\circ, 15^\circ, 19^\circ$

(b) Steel, $v_0 = 148$ m/s, $\alpha = 0^\circ, 5^\circ, 10^\circ, 15^\circ$



Appendix
 Fig. 15 Graph of final velocity vs. initial velocity, $\alpha_1 = 15^\circ$.



Appendix
 Graph of final oblique angle vs. initial velocity, $\alpha_1 = 5^\circ$.

Fig. 16

TABLE 2. BALLISTIC LIMITS OF TARGETS

Comparison of Data from Series 1 and Series 2, 2024-0 A1

Yaw Angle, deg.	Experimental Ballistic Limit, Ser. 1	Experimental Ballistic Limit, Ser. 2	Adjusted Ballistic Limit, Ser. 2	% Difference, (v50 - v50a)/v50
	v50, m/s	v50i, m/s	v50a, m/s*	
0	153	133	148	3.3
5	156	139	154	1.3
10	159	143	159	0
15	165	146	162	1.8
19		185		

*v50a is the ballistic limit for the second series adjusted for the mass difference in projectile/sabot mass between the two series, $v50a = v50i(5.0/4.5)$

Comparison of Theoretical and Experimental Values, 2024-0 A1

Yaw Angle, deg.	Experimental Ballistic Limit, Ser. 1 v50, m/s	Theoretical Ballistic Limit, v50t, m/s		% Difference (v50 - v50t)/v50	
		(a)	(b)	(a)	(b)
		S _y = 200 MPa	S _y = 250 MPa		
0	153	131	146	14.4	4.6
5	156	138	154	11.5	1.3
10	159	144	160	9.4	-0.6
15	165	150	166	9.1	-0.6

Percent Increase in Ballistic Limit with Yaw
 $Z = 100 \times (v50^{<a^0>} - v50^{<0^0>})/v50^{<0^0>}$

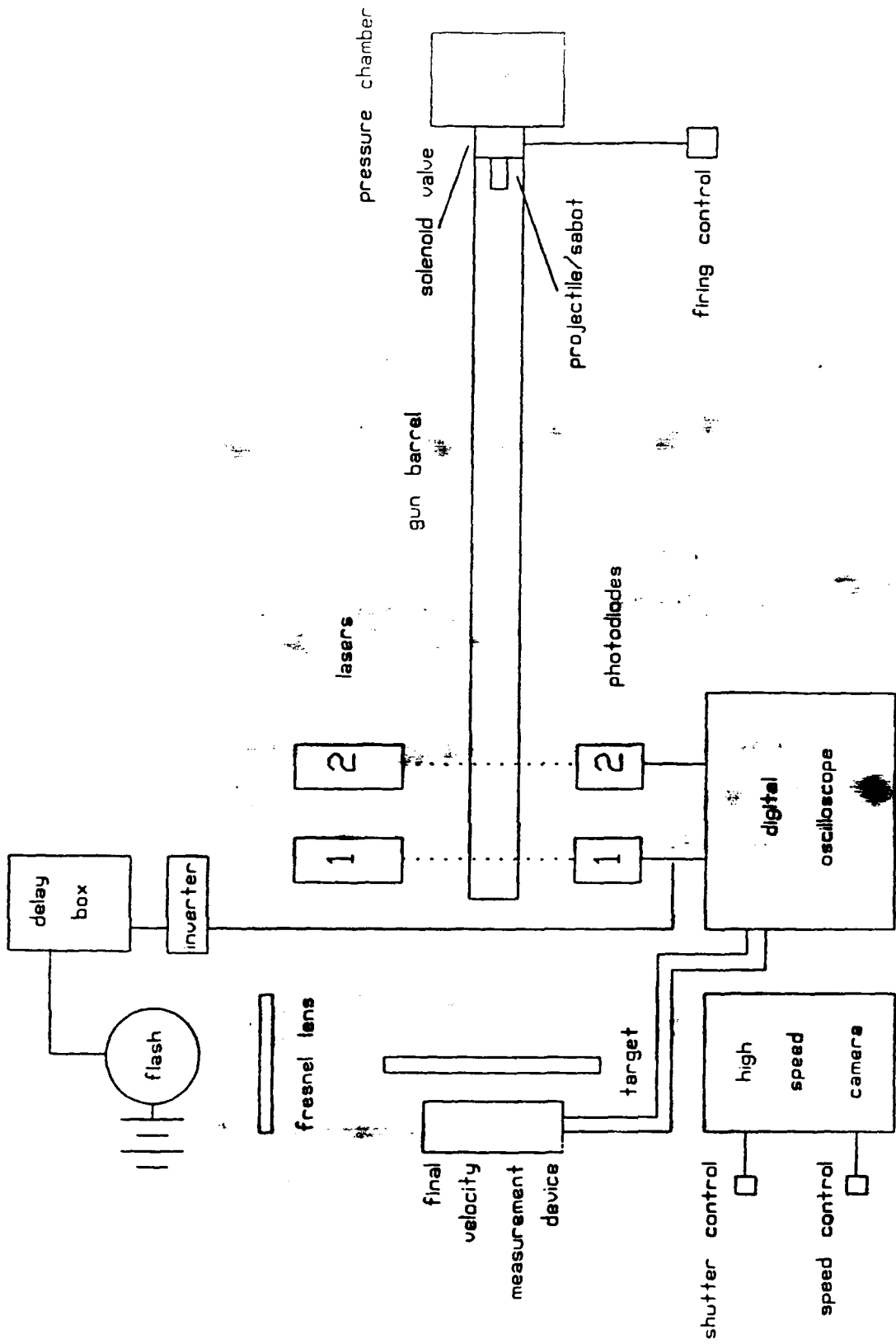
Yaw Angle, deg.	Series		Theory	Ref. [20]
	1	2		
5	2.0	4.5	5.3	3
10	3.9	7.5	9.2	12
15	7.8	9.8	13.7	--
19		12.6		

Experimental Value of the Ballistic Limit for 4130 Steel, m/s

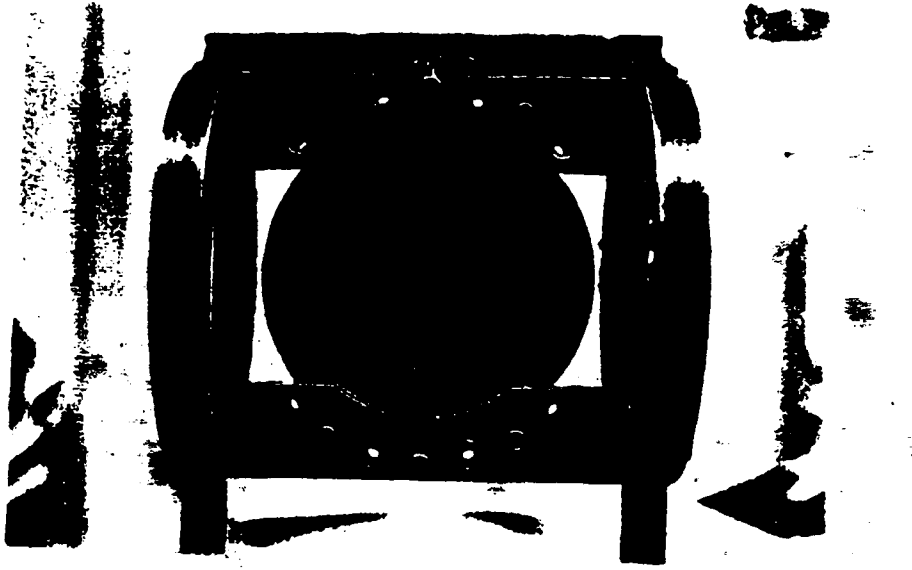
Yaw Angle, deg.	Series 1	Series 2 v50i	Adjusted Series 2 v50a
0	170	148	164
5		200	222
10	175	230	256
15		259	288
19		288	365

CAPTIONS FOR FIGURES

- Fig. 1 Schematic of Experimental Arrangement
- Fig. 2 Exit Side View of Target in Holder
- Fig. 3 Definition of the Yaw Angle, α , oblique angle, β , and Trajectory Angle, β' .
- Fig. 4 Penetration and Perforation Model of Impact with Yaw of a Cylindrical Projectile on a Thin Plate
- Fig. 5 Perforation Sequence for Run 30, 2024-0 Aluminum Target struck at 193 m/s at a 15° Yaw Angle with a Camera Speed of 44320 frames/s. The sabot is seen to break into two pieces
- Fig. 6 Simulation of the Penetration Process
- Fig. 7 Bulging of the Aluminum Plate for Non-perforation Run 16 ($v_0 = 155$ m/s; $\alpha = 10^\circ$)
- Fig. 8 Bulging of the Steel Plate at the Ballistic Limit, Run 36 ($v_0 = 175$ m/s, $\alpha = 0^\circ$)
- Fig. 9 Lateral Deformation of the Aluminum Plate, Run 27 ($v_0 = 170$ m/s, $\alpha = 15^\circ$)
- Fig. 10 Side Petaling of the Aluminum Plate, Run 19 ($v_0 = 176$ m/s, $\alpha = 10^\circ$)
- Fig. 11 Front Petaling of the Aluminum Plate, Run 33 ($v_0 = 234$ m/s, $\alpha = 15^\circ$)
- Fig. 12 Cross Section of a Nonperforated Aluminum Plate, Run 24 ($v_0 = 148$ m/s, $\alpha = 15^\circ$)
- Fig. 13a to 13c Cross Section of Aluminum Plates for Perforation Run 6 ($v_0 = 169$ m/s, $\alpha = 0^\circ$); Run 19 ($v_0 = 176$ m/s, $\alpha = 10^\circ$), and Run 29 ($v_0 = 183$ m/s, $\alpha = 15^\circ$)
- Fig. 14 Perforation into Targets at the Ballistic Limit Speed with Yaw, Series 2: (a), Aluminum, $v_0 = 133$ m/s, $\alpha = 0^\circ, 5^\circ, 10^\circ, 15^\circ, 19^\circ$ (b) Steel, $v_0 = 148$ m/s, $\alpha = 0^\circ, 5^\circ, 10^\circ, 15^\circ$
- Fig. 15 Final vs. Initial Velocity for Aluminum, Series 1, at $\alpha = 15^\circ$
- Fig. 16 Final vs. Initial Oblique Angle, β , for $\alpha = 5^\circ$



Appendix Fig. 1 Schematic of Experimental Arrangement



Appendix

Fig. 2 Exit Side View of Target in Holder

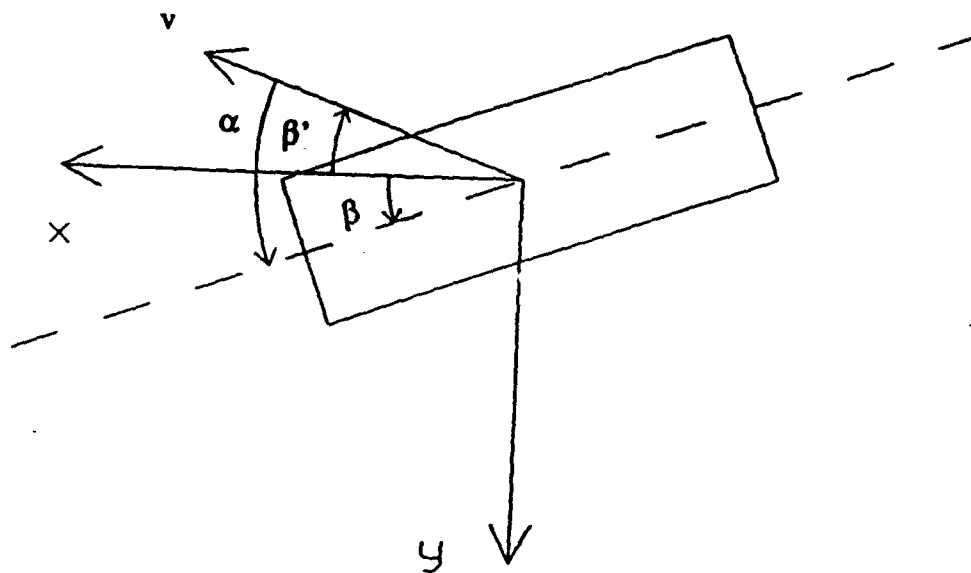
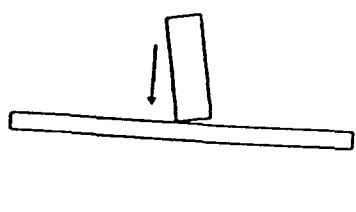
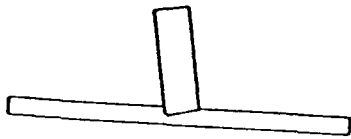


Fig. . 3

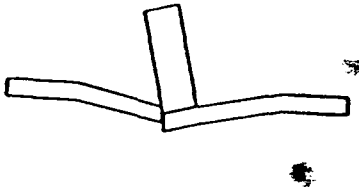
Appendix
Definition of the yaw angle (α), oblique angle (β), and trajectory angle (β').



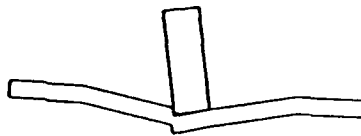
(a) initial contact



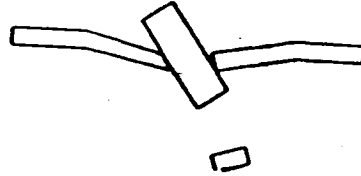
(b) indentation



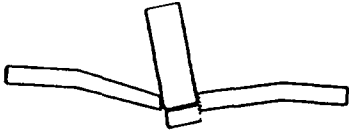
(c) membrane motion of the plate



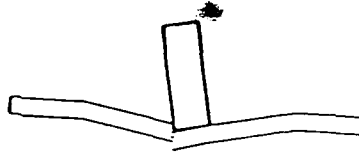
(d) tensile failure



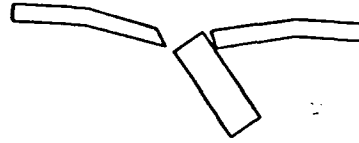
(e) initial projectile rotation



(f) plug shearing



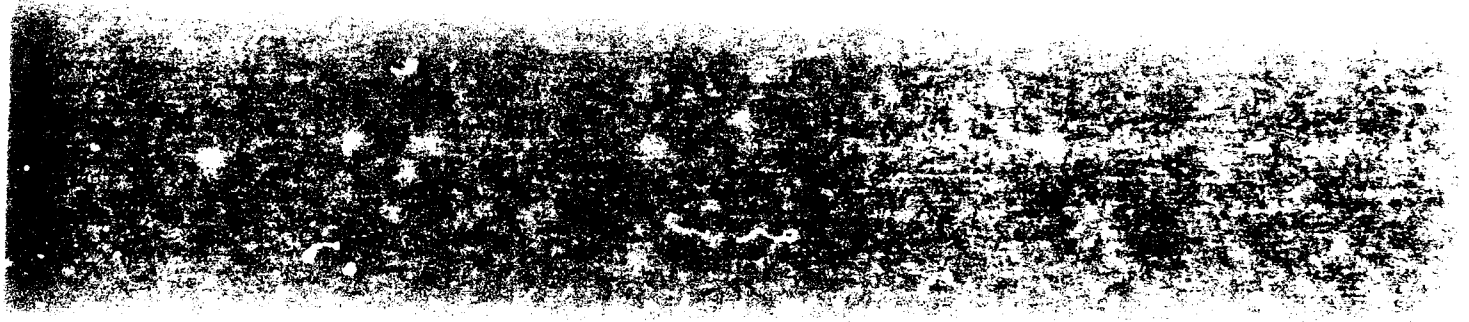
(g) plug ejection and petaling

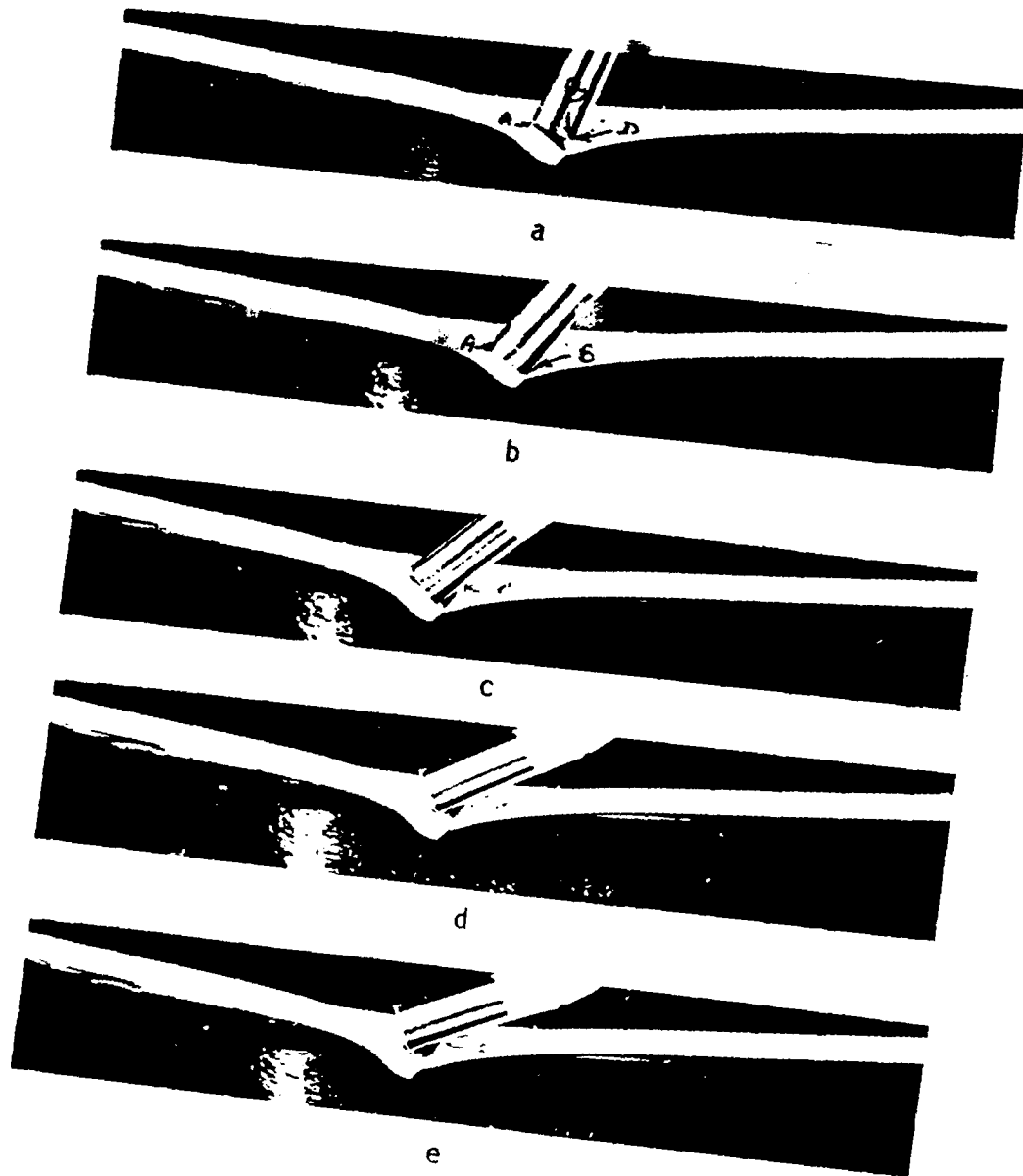


(h) exit of the projectile

Fig. 4 Penetration and perforation model--impact with yaw.

Appendix





Appendix
Fig. 6 Simulation of the Penetration Process

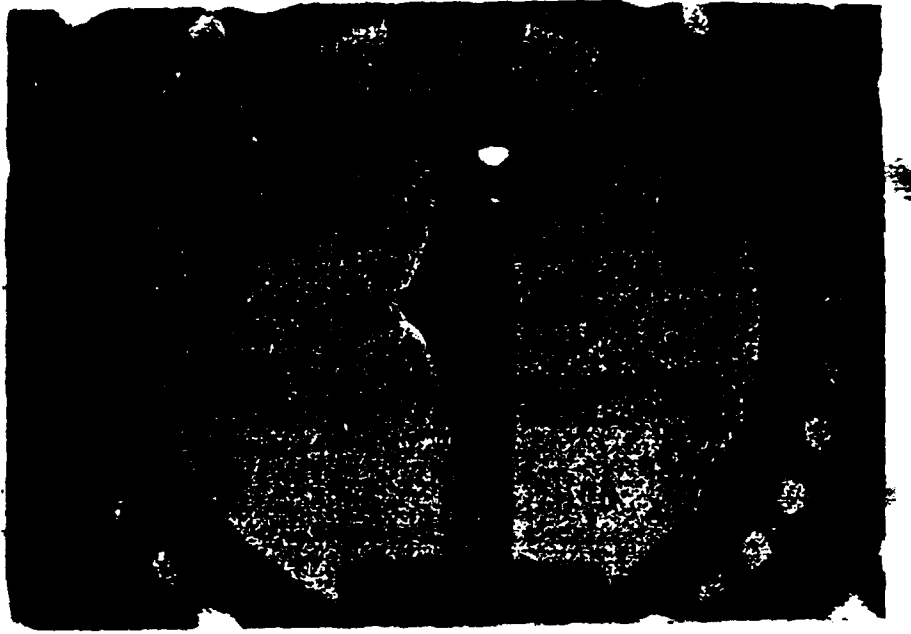


Fig. 7 Bulging of the Aluminum Plate for Non-perforation Run 16
($v_0 = 155$ m/s; $\alpha = 10^\circ$)

Appendix

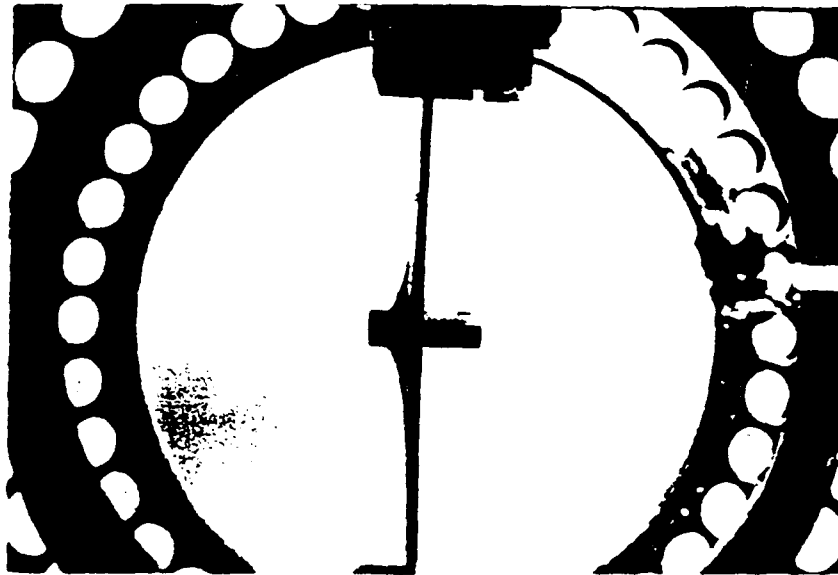
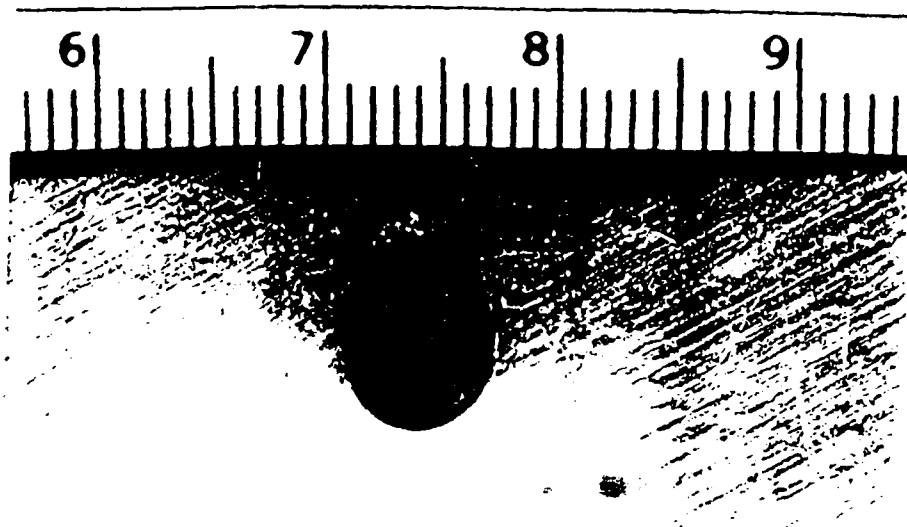


Fig. 8 Bulging of the Steel Plate, Run 36 ($v_0 = 175$ m/s, $\alpha = 0^\circ$)

Appendix



Appendix

Fig. 9 Lateral Deformation of the Aluminum Plate, Run 27
($v_0 = 170$ m/s, $\alpha = 15^\circ$)



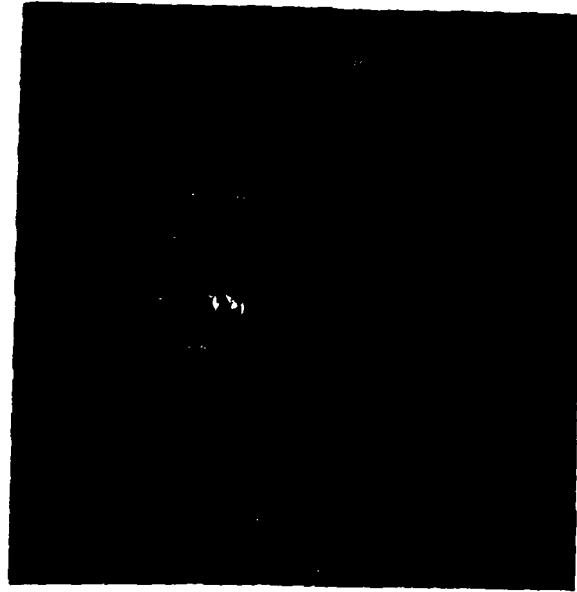
Appendix

Fig. 10 Side Petalling of the Aluminum Plate, Run 19 ($v_0 = 176$ m/s, $\alpha = 10^\circ$)

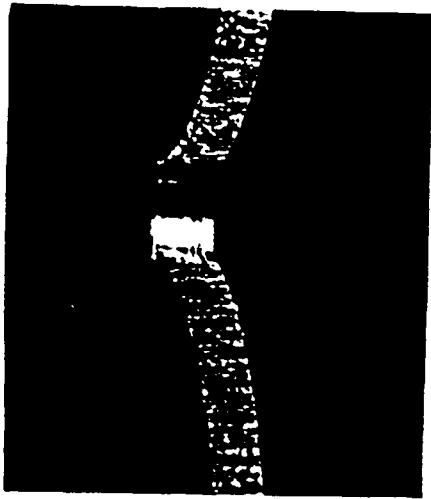


Appendix

Fig. 11 Front Petalling of the Aluminum Plate, Run 33 ($v_0 = 234$ r/s, $\alpha = 15^\circ$)



Appendix
Fig. 12 Cross Section of a Nonperforated Aluminum Plate, Run 24
($v_0 = 148$ m/s, $\alpha = 15^\circ$)



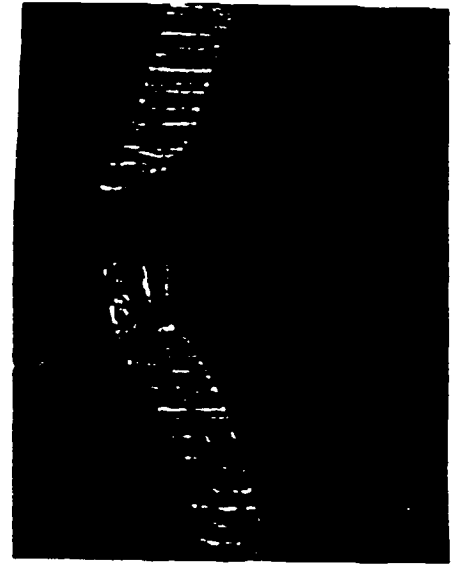
(a)

Run 6 ($v_0 = 169$ m/s,
 $\alpha = 0^\circ$)



(b)

Run 19 ($v_0 = 176$ m/s,
 $\alpha = 10^\circ$)



(c)

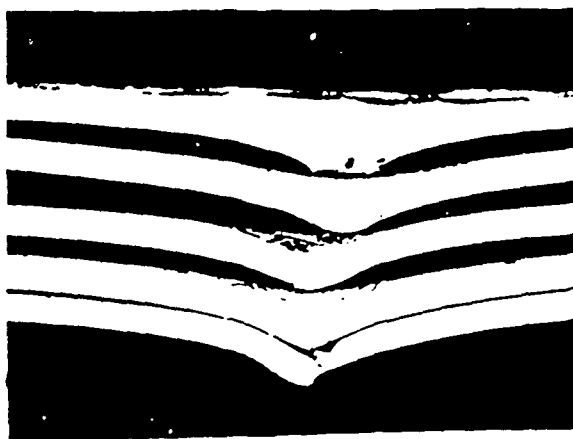
Run 29 ($v_0 = 183$ m/s,
 $\alpha = 15^\circ$)

Appendix

Fig. 13 Cross Section of Aluminum Plates for Perforation Runs

Yaw Angle

0°
5°
10°
15°
19°



(a)

0°
5°
10°
15°

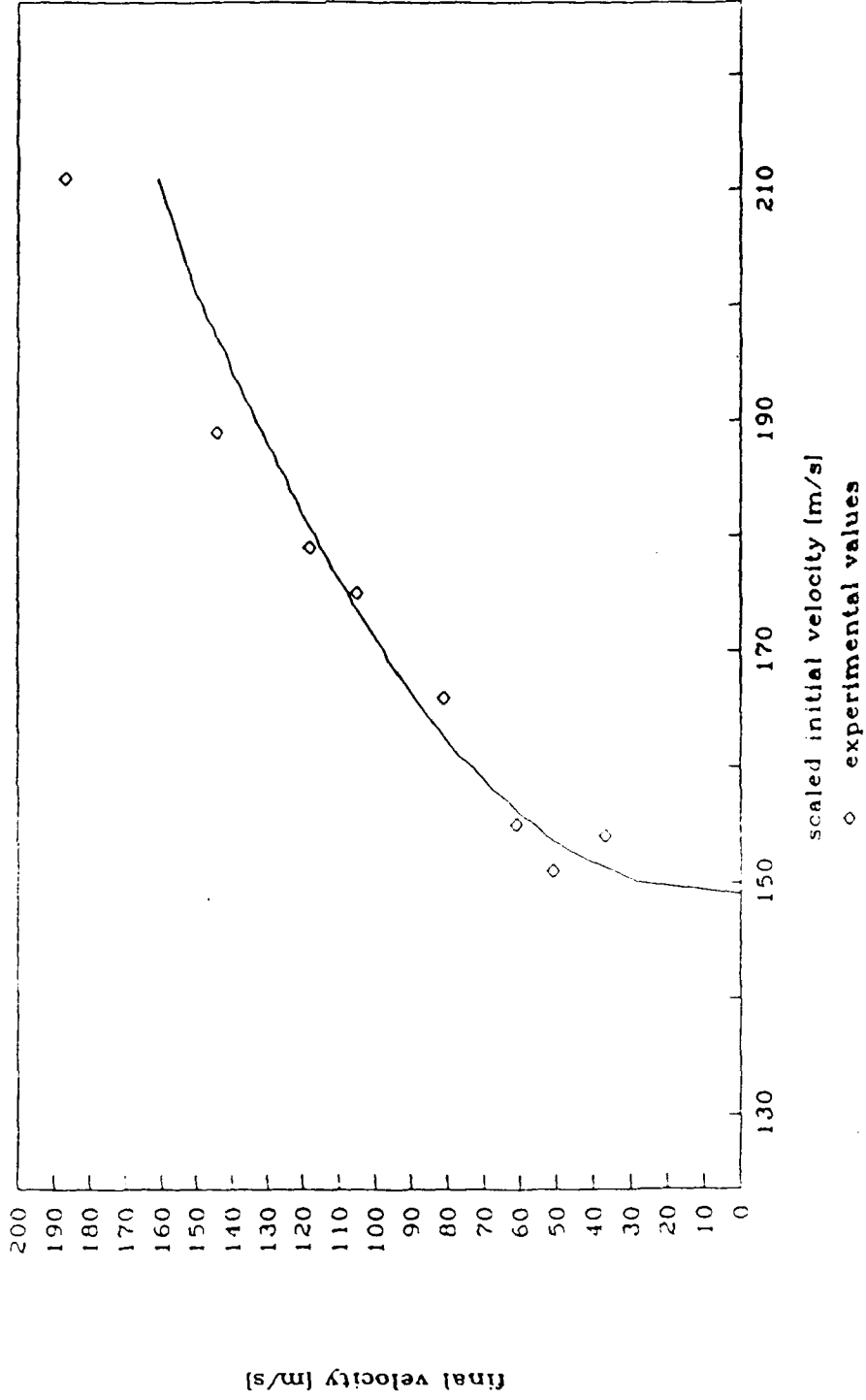


(b)

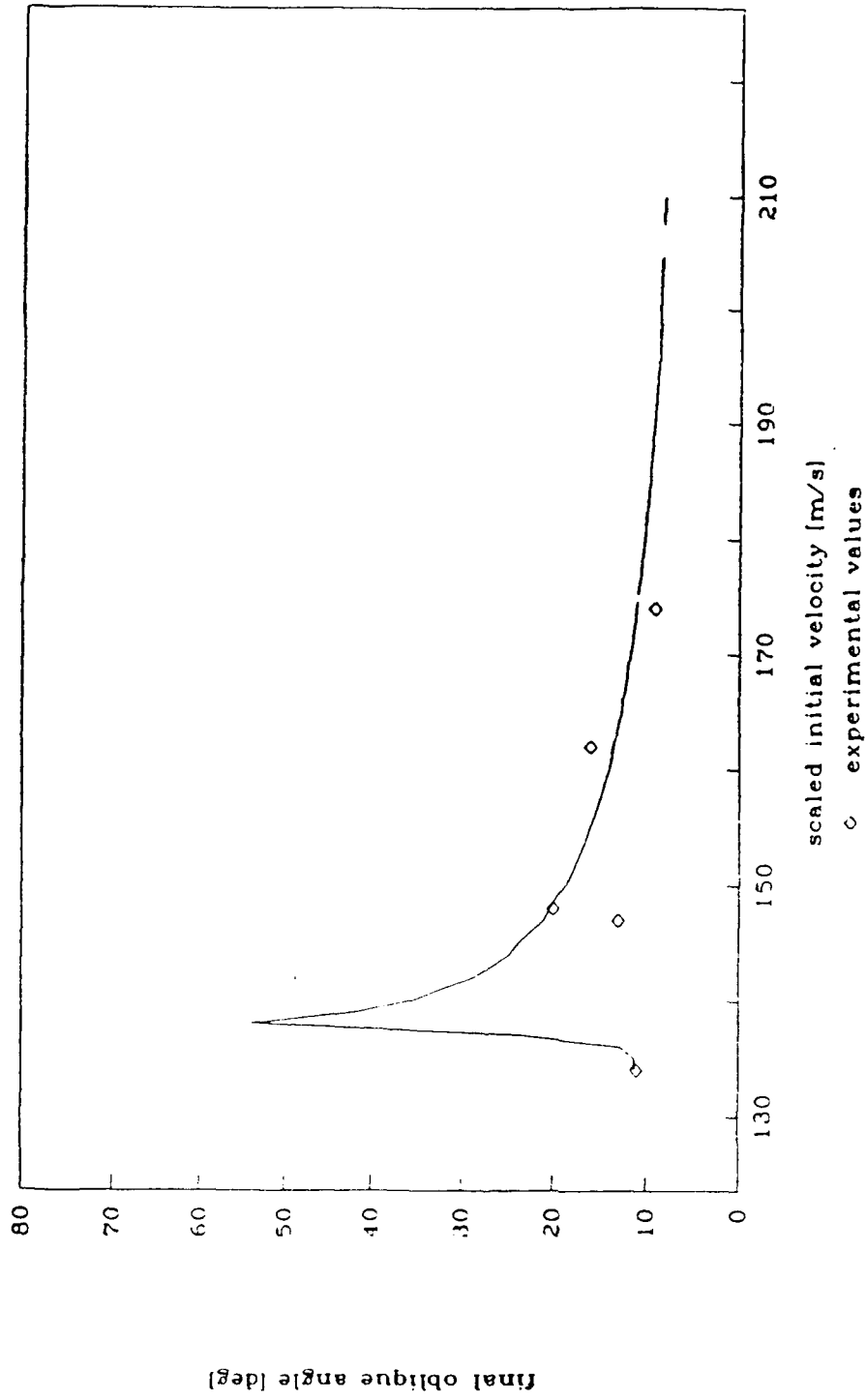
Appendix
Fig. 14 Perforation Into Targets at the Ballistic Limit Speed
with Yaw, Series 2

(a) Aluminum, $v_0 = 133$ m/s, $\alpha = 0^\circ, 5^\circ, 10^\circ, 15^\circ, 19^\circ$

(b) Steel, $v_0 = 148$ m/s, $\alpha = 0^\circ, 5^\circ, 10^\circ, 15^\circ$



Appendix
 Fig. 15 Graph of final velocity vs. initial velocity, $\alpha_1 = 15^\circ$.



Appendix
 Graph of final oblique angle vs. initial velocity, $\alpha_1 = 5^\circ$.

Fig. 16